

AD-A086 221

LOCKHEED MISSILES AND SPACE CO INC PALO ALTO CALIF

F/6 18/3

ASSESSMENT OF MAGNETOSPHERIC PROCESSES OF IMPORTANCE IN HANE.(U)

MAR 79 J B CLADIS, G T DAVIDSON, W E FRANCIS DNA001-78-C-0081

UNCLASSIFIED

LMSC/D634976

DNA-4822F

NL

[1 of 1]
AD-A
AD-A086 221

END
DATE
FILMED
8-80
DTIC

(12)
me

LEVEL II

AD-E 300 806 P

DNA 4822F

ADA 086221

ASSESSMENT OF MAGNETOSPHERIC PROCESSES OF IMPORTANCE IN HANE

J. B. Cladis

G. T. Davidson

W. E. Francis

L. L. Newkirk

M. Walt

Lockheed Missiles and Space Co., Inc.

3251 Hanover Street

Palo Alto, California 94304

15 March 1979

Final Report for Period 1 April 1978—15 March 1979

CONTRACT No. DNA 001-78-C-0081

APPROVED FOR PUBLIC RELEASE;
DISTRIBUTION UNLIMITED.

DTIC
ELECTE
S JUL 8 1980 D
B

THIS WORK SPONSORED BY THE DEFENSE NUCLEAR AGENCY
UNDER RDT&E RMSS CODE B322078462 I25AAXYX96013 H2590D.

Prepared for

Director

DEFENSE NUCLEAR AGENCY

Washington, D. C. 20305

80 5 14 001

DDC FILE COPY

Destroy this report when it is no longer
needed. Do not return to sender.

PLEASE NOTIFY THE DEFENSE NUCLEAR AGENCY,
ATTN: STTI, WASHINGTON, D.C. 20305, IF
YOUR ADDRESS IS INCORRECT, IF YOU WISH TO
BE DELETED FROM THE DISTRIBUTION LIST, OR
IF THE ADDRESSEE IS NO LONGER EMPLOYED BY
YOUR ORGANIZATION.



UNCLASSIFIED

SECURITY CLASSIFICATION OF THIS PAGE (When Data Entered)

REPORT DOCUMENTATION PAGE		READ INSTRUCTIONS BEFORE COMPLETING FORM
1. REPORT NUMBER DNA 4822F	2. GOVT ACCESSION NO. AD-A086 221	3. RECIPIENT'S CATALOG NUMBER
4. TITLE (and Subtitle) ASSESSMENT OF MAGNETOSPHERIC PROCESSES OF IMPORTANCE IN HANE.	5. TYPE OF REPORT & PERIOD COVERED Final Report, for Period 1 Apr 78-15 Mar 79,	6. PERFORMING ORG. REPORT NUMBER LMSC/D634976
7. AUTHOR(s) J. B. Cladis G. T. Davidson W. E. Francis	8. CONTRACT OR GRANT NUMBER(s) DNA 001-78-C-0081/New	9. PERFORMING ORGANIZATION NAME AND ADDRESS Lockheed Missiles and Space Co., Inc. 3251 Hanover Street Palo Alto, California 94304
10. CONTROLLING OFFICE NAME AND ADDRESS Director Defense Nuclear Agency Washington, D.C. 20305	11. REPORT DATE 15 March 1979	12. PROGRAM ELEMENT, PROJECT, TASK AREA & WORK UNIT NUMBERS Subtask I25AAXYX960-13
13. MONITORING AGENCY NAME & ADDRESS (if different from Controlling Office) 1284	14. NUMBER OF PAGES 84	15. SECURITY CLASS (of this report) UNCLASSIFIED
16. DISTRIBUTION STATEMENT (of this Report) 18) DNA, SRIE 19) 48-22F, AD-E300-216 Approved for public release; distribution unlimited.		
17. DISTRIBUTION STATEMENT (of the abstract entered in Block 20, if different from Report)		
18. SUPPLEMENTARY NOTES This work sponsored by the Defense Nuclear Agency under RDT&E RMSS Code B322078462 I25AAXYX96013 H2590D.		
19. KEY WORDS (Continue on reverse side if necessary and identify by block number) High-Altitude Nuclear Effects Current-Driven Instability Electrostatic Potentials in Magnetosphere Pitch-Angle Diffusion of Ions EIC Wave Turbulence Anomalous Resistivity		
20. ABSTRACT (Continue on reverse side if necessary and identify by block number) Conditions in the unstable field-aligned current sheet above the auroral oval have been obtained from analyses of the electron and ion measurements on the S3-3 satellite. The measurements were obtained while the satellite was in and near the nominal region of the current sheet, remaining within a few degrees in invariant latitude, over a magnetic local-time interval of about 6 hours. Potential differences along the magnetic field, above and below the satellite, were inferred from the energy and pitch-angle		

DD FORM 1 JAN 73 1473 EDITION OF 1 NOV 65 IS OBSOLETE

UNCLASSIFIED

SECURITY CLASSIFICATION OF THIS PAGE (When Data Entered)

210110

LB

UNCLASSIFIED

SECURITY CLASSIFICATION OF THIS PAGE(When Data Entered)

20. ABSTRACT (Continued)

distributions of the electrons. These potential differences, which exceeded 10 kV at times, were generally higher during the local evening than during the local afternoon, and were quite variable along the satellite trajectory, indicating latitudinal fluctuations of the current sheet with periods of 2-7 minutes. Upward flowing H^+ and O^+ ions were observed whenever the potential differences exceeded about .5 kV, which corresponds to the lowest energy threshold of the detectors. However, the pitch-angle distributions of the ions imply that the ions were accelerated not only along the magnetic field by the potential difference, but also perpendicularly to the field. The transverse acceleration of the ions most probably occurred through interactions with electrostatic ion cyclotron (EIC) waves, which are an expected product of the current-driven instability, and which have been observed in the current-sheet region.

A Monte Carlo program was used to compute energy and pitch-angle distributions of ions, taking into account the effects of the waves, the potential difference along the magnetic field, and the divergence of the magnetic field. Two measurements of the ion distribution were reconstructed by choosing a transverse-heating rate appropriate for measurements of the wave power spectrum, a potential difference below the satellite equal to that inferred from the electron distribution, a source base 2000 km to 4000 km below the satellite, and a source intensity that decreases exponentially at altitudes above the base with a scale height of 600 km to 1000 km. An ion distribution, measured when the potential difference above the satellite was high, was reconstructed with parameters similar to the above, except with a source intensity that increased with altitude above the base. The parameters used to fit the measured distributions are consistent with anomalous-resistivity theory.

UNCLASSIFIED

SECURITY CLASSIFICATION OF THIS PAGE(When Data Entered)

SUMMARY

This report addresses the question of the coupling between the ionosphere and magnetosphere resulting from a high-altitude nuclear explosion. The close analogy of phenomena ensuing from a nuclear burst with natural phenomena in the polar-cap region is pointed out; the recent findings with the S3-3 satellite over aurorae imply that the coupling will be greatly reduced in magnetic tubes containing hot plasma.

Previous analyses of the S3-3 satellite data indicate that the magnetic-field-aligned current sheet above the aurorae generally becomes unstable, generating electrostatic wave turbulence and high potential differences along the magnetic field. Here, we present information on the conditions in the unstable current region inferred from the analysis of data obtained along an unusual trajectory of the satellite wherein the satellite remained in and near the current sheet for an interval of about six hours in magnetic local time. Potential differences along the magnetic field, above and below the satellite (altitude ≈ 7800 km) are inferred from the energy and pitch-angle distributions of the electrons. These potential differences, which exceeded 10 kV at times, were generally higher during the local evening than during the local afternoon. They were also quite variable along the satellite trajectory, indicating latitudinal fluctuations of the current sheet with periods of 2-7 minutes.

Upward-flowing H^+ and O^+ ions appeared whenever the potential differences exceeded about .5 kV, which corresponds to the lowest energy threshold of the detectors. However, the pitch-angle distributions of the ions imply that the ions were accelerated not only along the magnetic field by the potential differences, but also perpendicularly to the field. The transverse acceleration of the ions most probably occurred through interactions with electrostatic ion cyclotron (EIC) waves, which are an expected product of the current-driven instability, and which have been observed in the current-sheet region.

A Monte Carlo program was used to compute energy and pitch-angle distributions of ions, taking into account the effects of the waves, the potential difference along the magnetic field, and the divergence of the magnetic field. Two measurements of the ion distribution were reconstructed by choosing a transverse-heating rate appropriate for measurements of the wave power spectrum, a potential difference below the satellite equal to that inferred from the electron distribution, a source base 2000 km to 4000 km below the satellite, and a source intensity that decreases exponentially at altitudes above the base with a scale height of 600 km to 1000 km. An ion distribution, measured when the potential difference above the satellite was high, was reconstructed with parameters similar to the above, except with a source intensity that increased with altitude above the base. The parameters used to fit the measured distributions are consistent with anomalous-resistivity theory.

Recommendations are made for further work that is necessary in order to assess the effects of the current-driven instability on the environmental conditions resulting from a nuclear explosion.

PREFACE

We wish to thank Drs. R. G. Johnson, R. D. Sharp, and E. G. Shelley of the Lockheed Palo Alto Research Laboratory, and Drs. J. F. Fennell and P. F. Mizera of the Aerospace Corporation for making available to us their charged particle data obtained on the S3-3 satellite. We also thank Drs. F. S. Mozer, P. Kintner, and R. L. Lysak of the University of California at Berkeley for consultations on the properties of the electric field, and ambient plasma inferred from their measurements on the S3-3 satellite. Furthermore, we are grateful to Drs. C. A. Blank and P. Crowley of the Defense Nuclear Agency for their guidance and support.

ACCESSION for		
NTIS	White Section	<input checked="" type="checkbox"/>
DOC	Buff Section	<input type="checkbox"/>
UNANNOUNCED		<input type="checkbox"/>
JUSTIFICATION _____		
BY _____		
DISTRIBUTION/AVAILABILITY CODES		
Dist.	AVAIL. and/or	SPECIAL
A		

TABLE OF CONTENTS

SECTION		PAGE
I	INTRODUCTION	9
II	RELEVANCE OF POLAR-CAP PROCESSES TO NUCLEAR-BURST-INDUCED PROCESSES	12
	1. CONVECTION OF MAGNETIC TUBE CONTAINING HOT PLASMA	12
	2. CONVECTION OF POLAR CAP FIELD LINES	12
III	CONDITIONS IN UNSTABLE-CURRENT REGION	16
	1. S3-3 SATELLITE MEASUREMENTS	16
	2. ANALYSIS OF DATA	28
	3. RESULTS	37
IV	ANALYSIS OF ION DISTRIBUTIONS	41
	1. PITCH-ANGLE DIFFUSION IN PRESENCE OF ELECTRIC FIELDS	41
	2. DIFFUSION COEFFICIENTS FOR INTERACTIONS WITH ELECTROSTATIC WAVES	44
	3. SOLVING THE DIFFUSION EQUATION	46
	4. RESULTS OF MONTE CARLO CALCULATION	49
V	CONCLUSIONS	70
VI	RECOMMENDATIONS	72
VII	REFERENCES	75

LIST OF ILLUSTRATIONS

<u>Figure</u>		<u>Page</u>
1	Illustration of electric field across hot-plasma tube and current tending to neutralize the excess charges at the east and west boundaries of the tube.	13
2	Illustration of electric field over polar cap and current tending to neutralize the excess charges at the dawn and dusk boundaries of the antisolar convection region.	14
3	Altitude and invariant latitude of satellite versus satellite spin number, universal time, and magnetic local time.	18
4	Survey plot of Lockheed data obtained with the S3-3 satellite on a tangential pass through a field-aligned current region on 17 January 1977.	19
5	Magnetic-field ratio B_s/B_t as function of satellite altitude.	30
6	Illustration of transformation of flux which is isotropic at B_1 , $\phi = 0$ to B_s , ϕ_s , where $B_1/B_s = .77$ and $\phi_s = .8$ kV.	32
7	Counting-rate ratio $C(\alpha_L)/C(90^\circ)$ versus w_1 .	34
8	The potential ϕ_s (straight lines) and pitch angle α_L (curves) are plotted versus B_1/B_s for various fixed values of w_1 .	35
9	The potential ϕ_s versus B_1/B_s for fixed values of the counting-rate ratio R .	36
10	Potential difference below satellite as function of satellite spin number.	38
11	The potential difference above the satellite as a function of the satellite spin number.	39
12	Energy distribution of ions (number of ions in energy cells divided by energy widths of cells).	50
13	Energy spectra of ions measured by the Lockheed and Aerospace groups on the three consecutive spins of the S3-3 satellite through the inverted-V structure discussed in References 1 and 2.	51

LIST OF ILLUSTRATIONS (Continued)

<u>Figure</u>		<u>Page</u>
14	Histogram of directional flux versus energy.	53
15	Histogram of pitch-angle distribution of ions for conditions listed in caption of Figure 14.	54
16	Histogram of directional flux versus energy.	55
17	Histogram of pitch-angle distribution of ions for conditions listed in caption of Figure 16.	56
18	Histogram of directional flux versus energy.	57
19	Histogram of pitch-angle distribution of ions for conditions listed in caption of Figure 18.	58
20	Histogram of directional flux versus energy.	59
21	Histogram of pitch-angle distribution of ions for conditions listed in caption of Figure 20.	60
22	Histogram of directional flux versus energy.	61
23	Histogram of pitch-angle distribution of ions for conditions listed in caption of Figure 22.	62
24	Histogram of directional flux versus energy.	63
25	Histogram of pitch-angle distribution of ions for conditions listed in caption of Figure 24.	64
26	Histogram of directional flux versus energy.	65
27	Histogram of pitch-angle distribution of ions for conditions listed in caption of Figure 26.	66
28	Histogram of directional flux versus energy.	67
29	Histogram of pitch-angle distribution of ions for conditions listed in caption of Figure 28.	68
30	Directional flux at B_s , ϕ_s versus pitch angle for ions that have been transversely heated at $B=5B_s$, $\phi-\phi_s=1$ kV to a temperature of 0.8 keV.	73

LIST OF TABLES

<u>Table</u>		<u>Page</u>
1	Detector characteristics	17
2	Parameters in model that give computed ion spectra similar to observed spectra 1 and 2.	52

SECTION I

INTRODUCTION

The electrical coupling of the ionosphere and magnetosphere strongly affects several components of the environment resulting from a high-altitude nuclear explosion. The most important of these are 1) the plasma irregularities, which degrade communications and radar systems, 2) the emissions due to energy and debris deposition in the atmosphere, which enhance the backgrounds of optical/IR systems, 3) the distribution of the energetic ionized debris and air in the magnetosphere, which erode satellite surfaces, and 4) the distribution of the trapped relativistic electrons, which degrade satellite components. In all the work that has been done to date on the delineation of these environmental components, the classical values of the conductivity along the magnetic field, based on binary collisions, have been used. Above the F-layer of the ionosphere such conductivities are so low that the magnetic field lines have been regarded to be equipotentials. All this work now needs to be reassessed in view of the S3-3 Satellite data, which unequivocally imply the presence of high electrostatic potential differences along the magnetic field.

The data reveal that these potential differences extend to tens of kilovolts (Refs. 1, 2, 3) and are nearly always present in a narrow magnetic shell, of thickness equal to a few degrees in latitude, connected to the auroral oval (Ref. 4). Specifically, the elevated potentials occur in the region of the upward flowing, magnetic-field-aligned currents described by Iijima and Potemra (Ref. 5). They are generally below the altitude of the S3-3 satellite (~1 earth radius), but occasionally extend to well above the satellite. The potential gradients are predominantly in a direction such that electrons are accelerated downward and ions upward. Indeed, ions (principally H^+ and O^+) in the keV range are often observed moving upward, generally closely aligned with the magnetic field, when these potential differences occur below the satellite (Ref. 4, 6, and 7).

The pitch-angle distributions of the ions, however, are much broader than expected if ions of the thermal population were simply accelerated along the magnetic field. The ions must also have been accelerated in the direction perpendicular to the magnetic field. Acceleration by waves is suggested. Turbulent electrostatic plasma waves, including electrostatic ion-cyclotron (EIC) waves, are nearly always observed in the region where the potentials occur (Refs. 8 and 9). It is therefore likely that the ions acquired their transverse energies by resonating with the EIC waves. In the adjacent regions where the field-aligned current flows downward (Ref. 5), coherent EIC waves are observed. There, the pitch-angle distributions of energetic H^+ , He^+ and O^+ ions are found to be conical, i.e., peaked at pitch-angles between 0 and 90° (Ref. 10). These distributions indicate that the ions are rapidly accelerated, within a short distance along the magnetic field, by the coherent EIC waves.

The satellite measurements described above indicate that a current-driven instability, generating electrostatic waves, may provide the mechanism necessary to support the field-aligned potential differences in the absence of collisions. Three theories of such instabilities have been proposed: The electric double layer (Refs. 11 and 12), the oblique electrostatic shock (Ref. 13), and anomalous resistivity (Ref. 14 and 15). Some features of each theory, at different times, seem to be implied by the data. The Kindel and Kennel theory (Ref. 14), however, appears to explain the majority of the observations. Their theory, for example, predicts the following:

- (i) A field-aligned current will become unstable above the F-layer of the ionosphere in the density range $2\text{--}20\mu\text{A}/\text{m}^2$. (Such densities have been confirmed by measurements.)
- (ii) The instability will produce electrostatic-wave turbulence at drift velocities that are high compared with the electron thermal velocity. (The turbulence observed in the upward-flowing-current region may therefore be due to the high drift velocity of the downward-moving current-carrying electrons).
- (iii) EIC waves will be destabilized over a wide range of electron to ion temperatures (0.2 to 8) at the lowest current densities and critical-drift velocities. (The EIC waves in the absence of turbulence observed in the downward-flowing current region may therefore be due to the low drift velocity of the upward-moving electrons.)
- (iv) In a plasma containing two ionic constituents, the heavier ion cyclotron waves will be more easily destabilized, even if the heavier-ion abundance is as low as about 10%. (Although the low-frequency He^+ and O^+ cyclotron waves are difficult to identify because of the noise, their effects, i.e., the conical distributions of the He^+ and O^+ ions, have been observed.)

In the context of the Kindel and Kennel theory, the potential differences are due to anomalous resistivity. The wave turbulence provides the resistive drag that inhibits the directed motion of the electrons along the magnetic field and thus allows the potentials to build up. However, in order to appreciably retard the electron motion, it is necessary for the electric fields of the waves to be larger than the field aligned electric field arising from the potential (Ref. 16). This requires that the scale of the observed potentials be large: The measured wave fields are less than about $10\text{ mV}/\text{m}$ (Ref. 9) and the potential differences are generally larger than 1 kV , hence, the scale of the potential, and the extent of the wave turbulence, must be of the order of $10^3\text{V}/10^{-3}\text{V}/\text{m} = 10^6\text{m}$, or 1000 km , along the magnetic field. Quite often, however, electric fields as high as about $0.5\text{V}/\text{m}$ are measured (Ref. 8), implying shorter scales of the potentials. Hence, double layers or electrostatic shocks might also occur in the field-aligned current regions.

It is clear that much more information on these natural processes must be obtained before we can hope to predict the nuclear-induced environment. In particular, information is needed on the distribution (location and extent) of the potential along the magnetic field and on the nature and distribution of the wave turbulence.

We have been studying the potential distributions by analyzing the pitch-angle and energy distributions of the electrons and ions obtained with the Lockheed experiment (Ref. 6) on the S3-3 satellite. In our previous DNA report (Ref. 1) we described the "inverted-V" potential structure that was inferred from the observation while the satellite passed almost normally through the current sheet. In this report we present further information, based on the satellite measurements, on the properties of the instability and the conditions under which it occurs.

In Section II we point out the similarity of physical processes associated with the convection of field lines over the polar cap to the processes resulting from the expansion of the hot plasma produced by a nuclear explosion at high altitudes. This analogy clearly reveals that the auroral-zone observations discussed above are directly relevant to the ionosphere-magnetosphere coupling resulting from a nuclear burst. In Section III we present the Lockheed data obtained along an unusual trajectory wherein the satellite remained in and near the current sheet, within a few degrees of invariant latitude, over a local time interval of about 6 hours; and we discuss the conditions in that region inferred from an analysis of the data. In Section IV we discuss the theory of the pitch-angle diffusion of ions due to interactions with EIC waves, in the presence of an electric field along the magnetic field, and describe a Monte Carlo calculation that was used to compute the ion distributions. The properties of the EIC wave turbulence inferred from the comparison of the computed ion distributions with the measured distributions are discussed. The conclusions and recommendations for further work are discussed in Sections V and VI, respectively.

SECTION II

RELEVANCE OF POLAR-CAP PROCESSES TO NUCLEAR-BURST-INDUCED PROCESSES

1. CONVECTION OF MAGNETIC TUBE CONTAINING HOT PLASMA

Following a nuclear explosion at high altitudes, hot plasma expands into a local magnetic-tube of force, as depicted in Figure 1. Initially, this plasma consists of the bomb debris, including fission fragments and relativistic fission beta-decay electrons, and atmospheric constituents which have been energized and ionized near the burst point. Owing to the plasma pressure and the magnetic-field configuration, an outward force acts on the tube and polarizes the plasma in the azimuthal direction. As shown in Figure 1, a net negative charge appears at the eastern surface of the tube, and a net positive charge appears at the western surface. An electric field directed toward the east, therefore, develops in the tube, and the plasma drifts outward with the $\vec{E} \times \vec{B}$ drift velocity. In this manner the debris and the trapped relativistic electrons become distributed to regions of the magnetosphere above the magnetic shell in the vicinity of the burst.

At somewhat later times, the heated plasma resulting from energy deposition in the atmosphere expands into a local magnetic tube and polarizes either in the direction discussed above or in the opposite direction, depending on the magnitude of its kinetic-energy density. In either case, the combination of the resulting plasma $\vec{E} \times \vec{B}$ drift velocity and density gradient cause the plasma to striate. The striated, high-density plasma thereby becomes distributed over large distances in the magnetosphere and interferes severely with radio-wave propagation.

Both the distribution of the debris at early times and the plasma striations at later times, depend sensitively on the coupling of the ionosphere and magnetosphere. The charge separation across the magnetic tube tends to be neutralized by currents in the thermal plasma which, as shown in Figure 1, flow along magnetic field lines at high altitudes and across magnetic field lines in the ionosphere, where the collision frequency is sufficiently high. In the applications mentioned above, the neutralizing current has been accounted for by using the classical value of the conductivity. If a potential difference should develop in the magnetic-field-aligned current regions, due to anomalous resistivity or any other cause, it would greatly alter the distributions of the plasmas.

2. CONVECTION OF POLAR CAP FIELD LINES

The magnetic field lines over the polar cap are convected in the antisolar direction by the pressure of the solar wind. The motion induces a dawn-to-dusk electric field over the polar cap, as depicted in Figure 2. The net positive and negative charges are on the "stationary" field lines over the aurora oval, the positive charge being located on the half of the auroral oval on the dawn

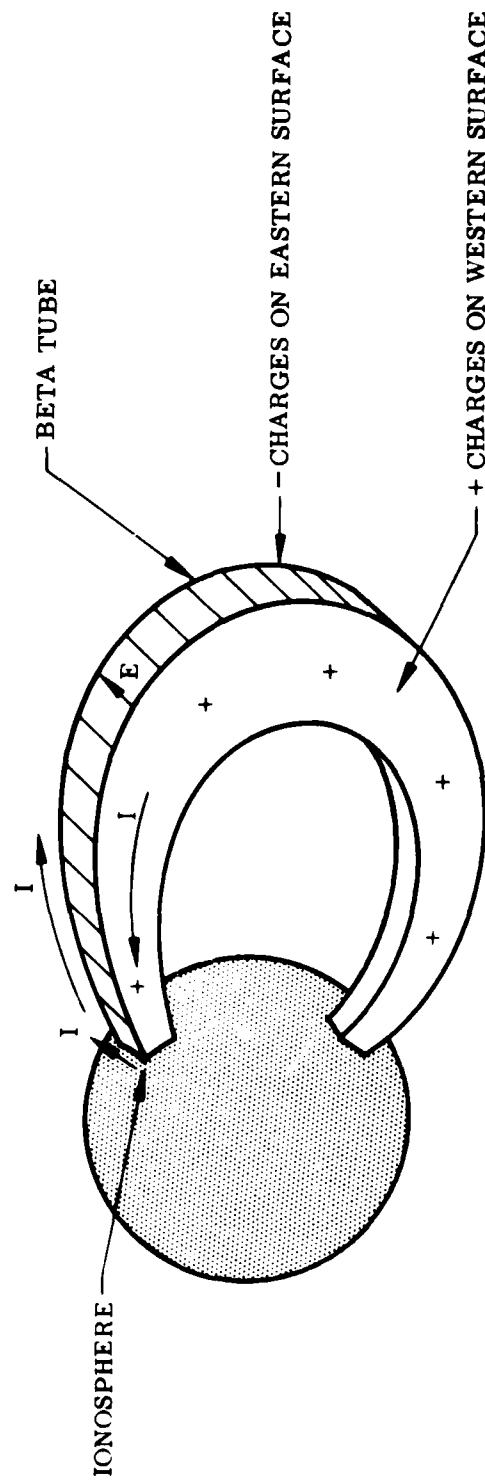


Figure 1. Illustration of electric field across hot-plasma tube and current tending to neutralize the excess charges at the east and west boundaries of the tube.

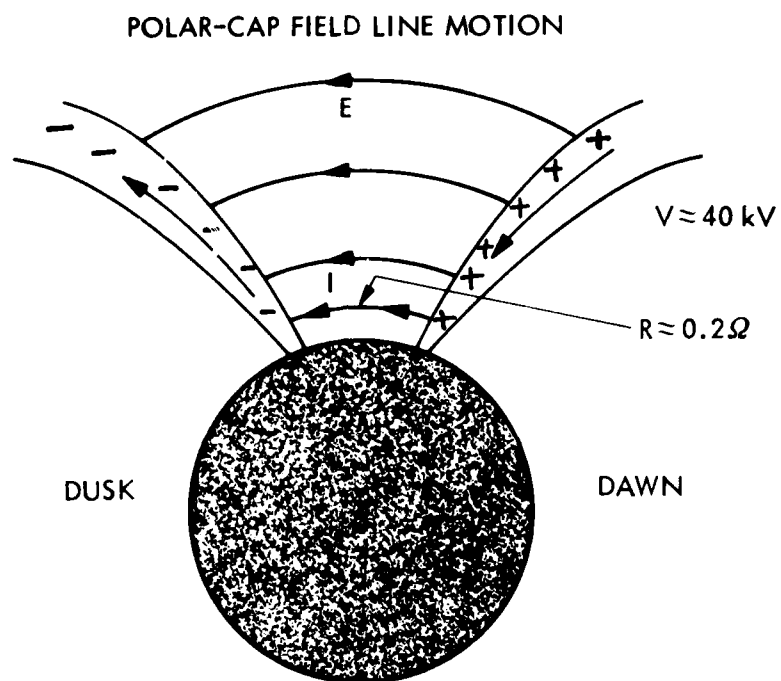


Figure 2. Illustration of electric field over polar cap and current tending to neutralize the excess charges at the dawn and dusk boundaries of the antisolar convection region.

side and the negative charge on the dusk half of the oval. The primary currents that tend to neutralize the charges are also shown in the figure. They flow down the field lines containing the net positive charge on the dawn side, across the polar cap in the ionosphere, and up the field lines containing the net negative charge. These are the region 1 currents identified by Iijima and Potemra (Ref. 5). A less intense region 2 current system is also observed at high values of Kp. These currents flow along field lines adjacent to the region 1 currents but at lower latitudes, and are directed opposite to the region 1 currents.

The potential across the polar cap is generally about 40 kV and the ionospheric resistance over the polar cap is about 0.2 ohms. Hence, the field-aligned region 1 current is about $4 \times 10^4 / 0.2 = 2 \times 10^5$ Amperes. Half the cross sectional area of the current shell at the altitude of the Triad satellite is approximately,

$$A = \pi(R_E + h_s)d \sin \theta \quad (1)$$

where R_E is the earth's radius, h_s is the altitude of the satellite, d is the width of the shell at h_s , and θ is the colatitude of the auroral zone. Taking $h_s = 800$ km, $d = 10$ km, and $\theta = 25^\circ$, we find that $A \approx 9.5 \times 10^4 \text{ km}^2$. The field-aligned current density is therefore $2 \times 10^5 / 9.5 \times 10^4 = 2.1 \mu\text{A/m}^2$. This value is consistent with the current densities measured with the Triad satellite (Ref. 5). It is also within the range of the critical current density given by Kindel and Kennel (Ref. 14) for the onset of the current-driven instability. Moreover, a current density of about $1 \mu\text{A/m}^2$ was measured on the S3-3 satellite when wave turbulence and other products of the instability were observed (Ref. 8). It is, therefore, not surprising that potential differences along magnetic field lines, as well as magnetic-field-aligned currents, are regular features of the auroral oval.

The field aligned currents along the eastern and western boundaries of the magnetic tube containing the early-time plasma, for a Starfish- or USSR1- type burst, is about 10^6 A (Ref. 17). Since the cross section of half the boundary just above the E-layer of the ionosphere is about $3 \times 10^{10} \text{ m}^2$, the field-aligned current density is about $30 \mu\text{A/m}^2$. The current density is the most important parameter that determines whether the current becomes unstable (Ref. 14). Hence, since this value exceeds the critical value it is highly probable that the instability will occur in the hot-plasma tube as it does in the polar cap. Furthermore, since the processes responsible for the field-aligned currents are similar, the information that is now being obtained with the S3-3 satellite on the nature and effects of the instability in the auroral zone should be directly applicable to the plasma tube situation.

SECTION III

CONDITIONS IN UNSTABLE-CURRENT REGION

1. S3-3 SATELLITE MEASUREMENTS

The Lockheed experiment (Ref. 6) on the S3-3 satellite measures the energy and pitch-angle distributions of ions in the energy-per-charge range .50 - .16 keV and electrons in the energy range 70 eV - 24 keV. The measurements are obtained with three ion mass spectrometers and four magnetic electron spectrometers mounted such that their view directions are perpendicular to the spin axis of the satellite. The spin rate of the satellite is ≈ 3.5 RPM about an axis perpendicular to the orbital plane; hence a nearly complete pitch-angle scan is obtained in about 8.7 sec. The ion spectrometers sample the mass-per-charge (M/Q) distribution in the range 1 - 30 once per second. Each ion spectrometer has 4 energy-per-charge settings which are stepped every 16 sec. The energy settings of each ion spectrometer, together with the energy response and geometric factors of the electron spectrometers, are listed in Table 1.

On 17 January 1977, the satellite remained in and about the unstable-current region for a local-time interval of about 6 hours. The trajectory of the satellite is shown in Figure 3. There, the altitude and invariant latitude are plotted against satellite spin number and universal time in seconds (listed on abscissa at bottom of graph) and magnetic local time (listed at top of graph). The satellite spin number is a useful parameter in the discussion of the data. Note that the satellite's altitude and invariant latitude change very little as the satellite moves from 21.5 h to 15.7 h MLT, during a time interval of about 0.6 h. All the magnetic indices were low for several days prior to this satellite pass. At the time of the measurements the three-hourly Kp index was 2.

The data obtained on this pass are shown in Figure 4. At the bottom of the chart are shown the universal time (SYST), longitude, latitude, altitude in km, invariant latitude (ILA), and magnetic local time in h. The four lowest panels show the logarithm of the counts per half-second of the electron spectrometers. The panel labeled PITCH shows the pitch angle of the measured particles. Here, the pitch angle of 0° denotes particles moving directly down the field lines. The next four panels show the logarithm of the sum of the counts per second of the 3 mass spectrometers for ions of M/Q = 1, 2, 4, and 16 respectively. A code designating the energy steps of the mass spectrometers is in the top panel. The numbers on the pitch angle trace denote the spin number of the satellite. We will refer to the ions which have pitch-angle distributions peaked at $\alpha=180^\circ$, as field-aligned ions, although they are not strictly field aligned as discussed in the introduction.

Table 1. Detector characteristics.

<u>Detector</u>	<u>Particle</u>	<u>Energy, keV</u>	<u>GDE, cm² sr keV</u>			
CMEA	Electrons	0.07 - 0.24	1.2 x 10 ⁻⁶			
CMEB	Electrons	0.35 - 1.1	6.5 x 10 ⁻⁶			
CMEC	Electrons	1.6 - 5.0	1.9 x 10 ⁻⁵			
CMED	Electrons	7.3 - 24	6.5 x 10 ⁻⁵			
Energy per unit charge (keV)						
		Step 1	2	3	4	
CXA 1	Ions	0.50	0.68	0.94	1.28	
CXA 2	Ions	1.76	2.4	3.3	4.5	
CXA 3	Ions	6.2	8.5	11.6	16.0	

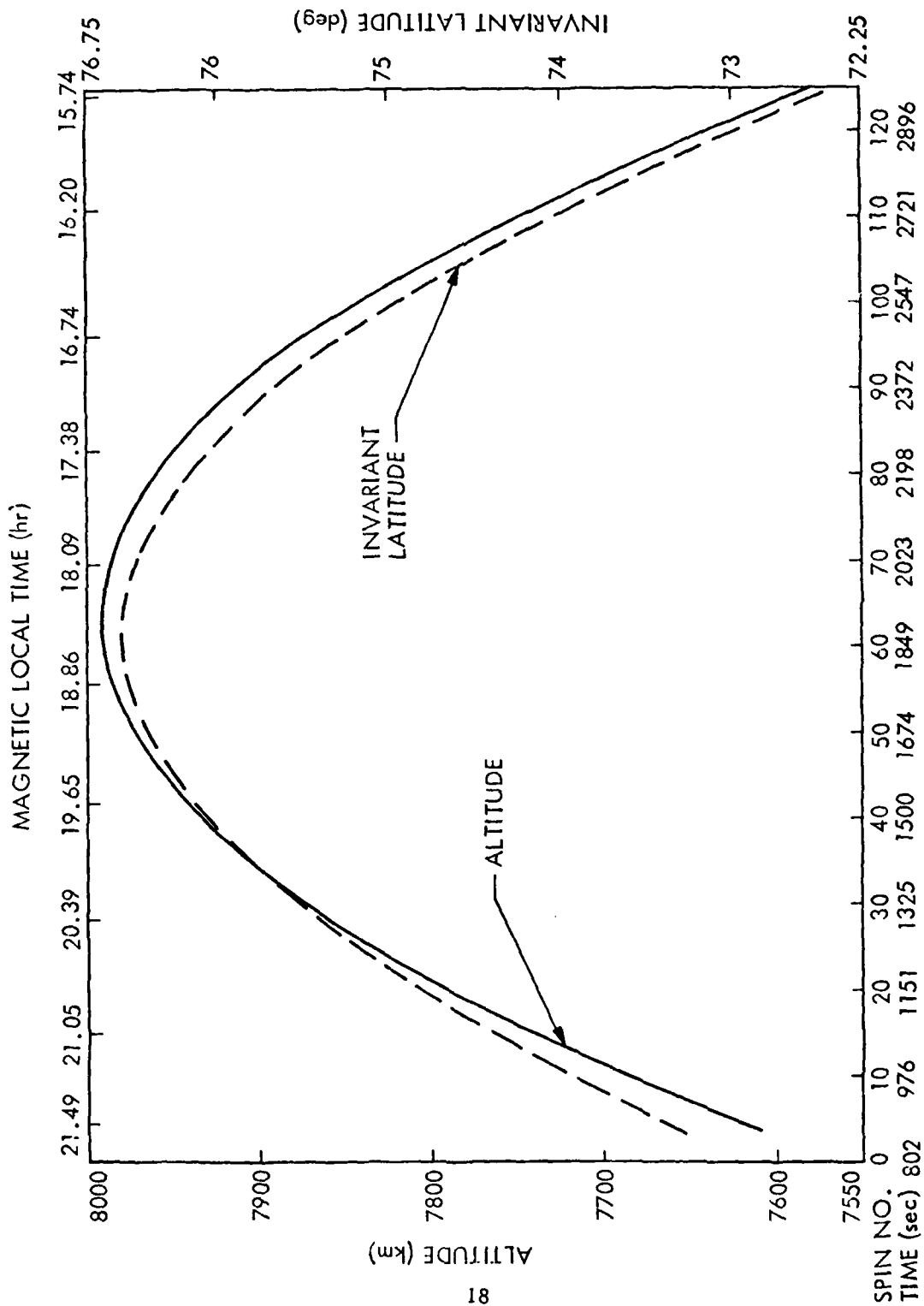


Figure 3. Altitude and invariant latitude of satellite versus satellite spin number, universal time, and magnetic local time.

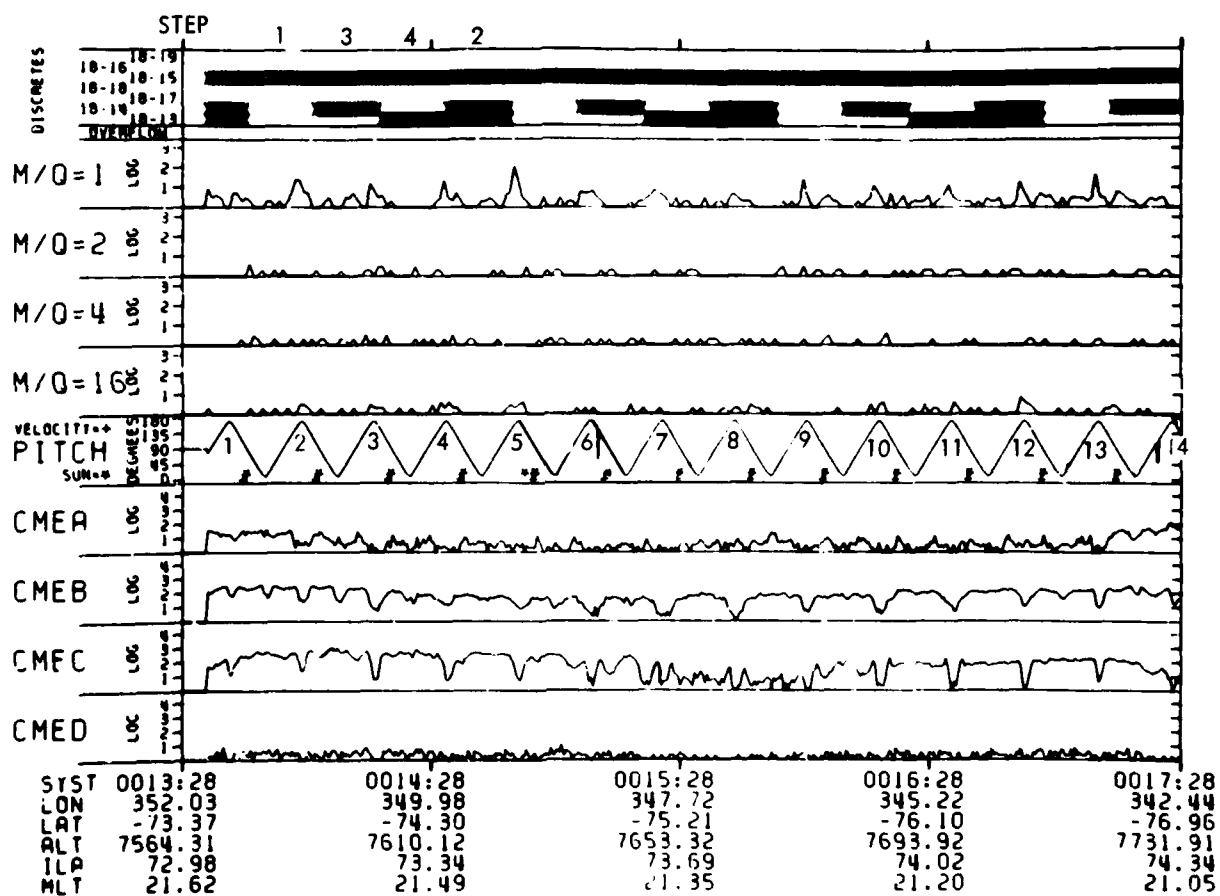
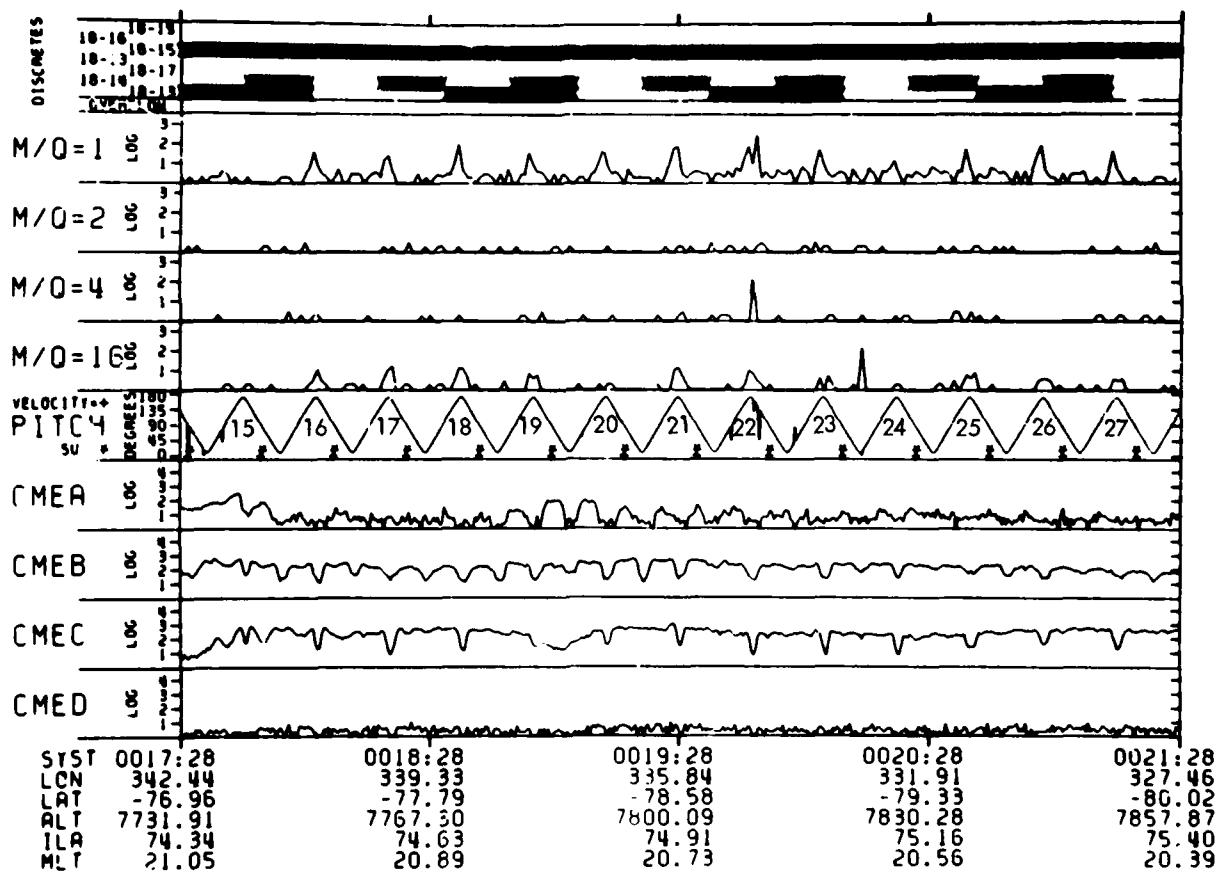
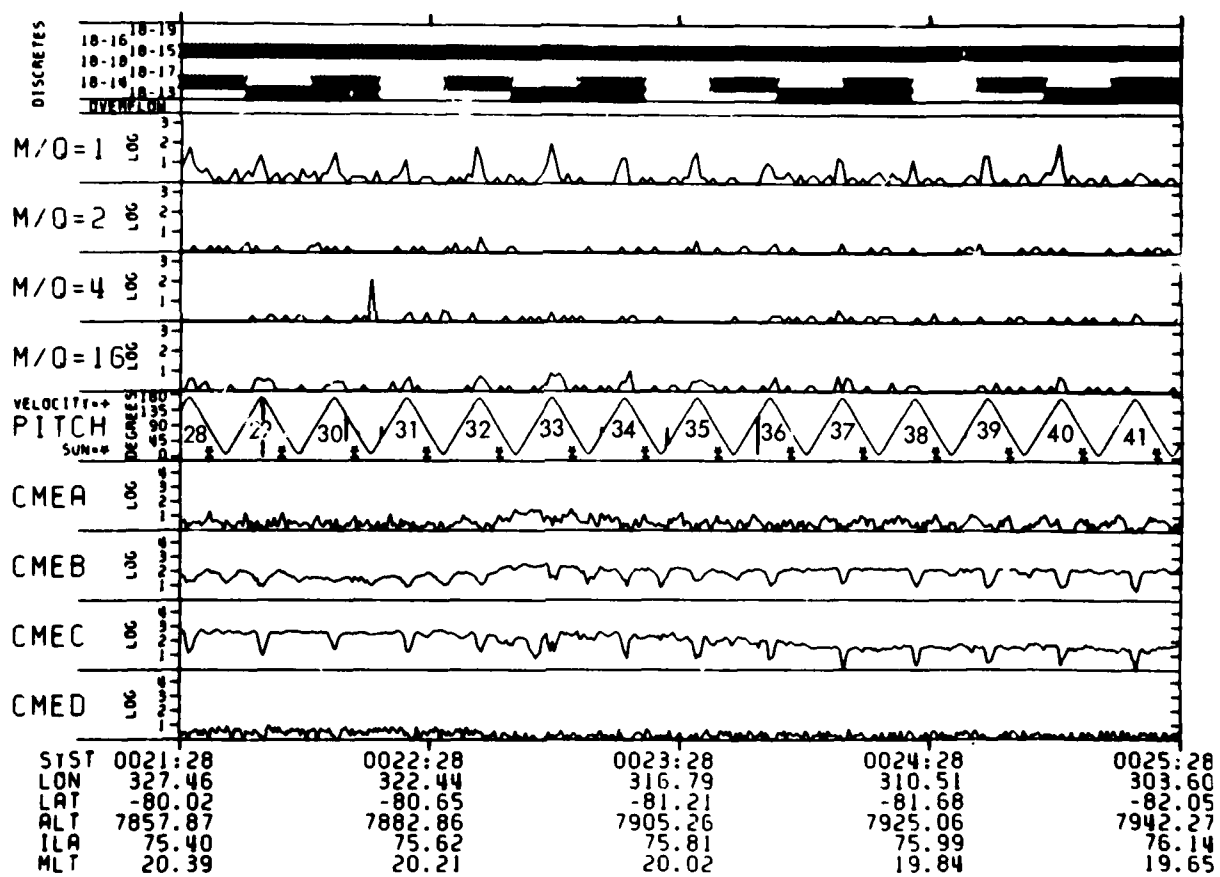
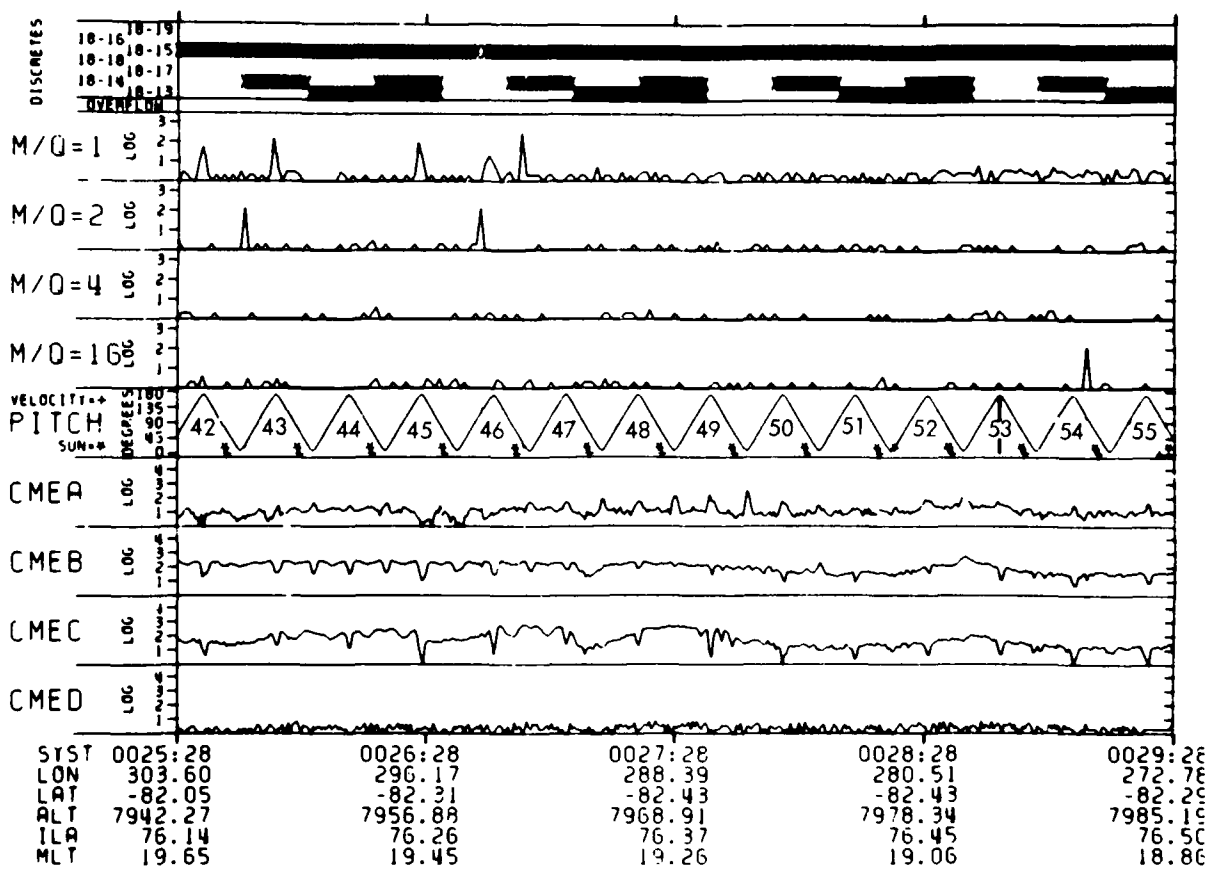
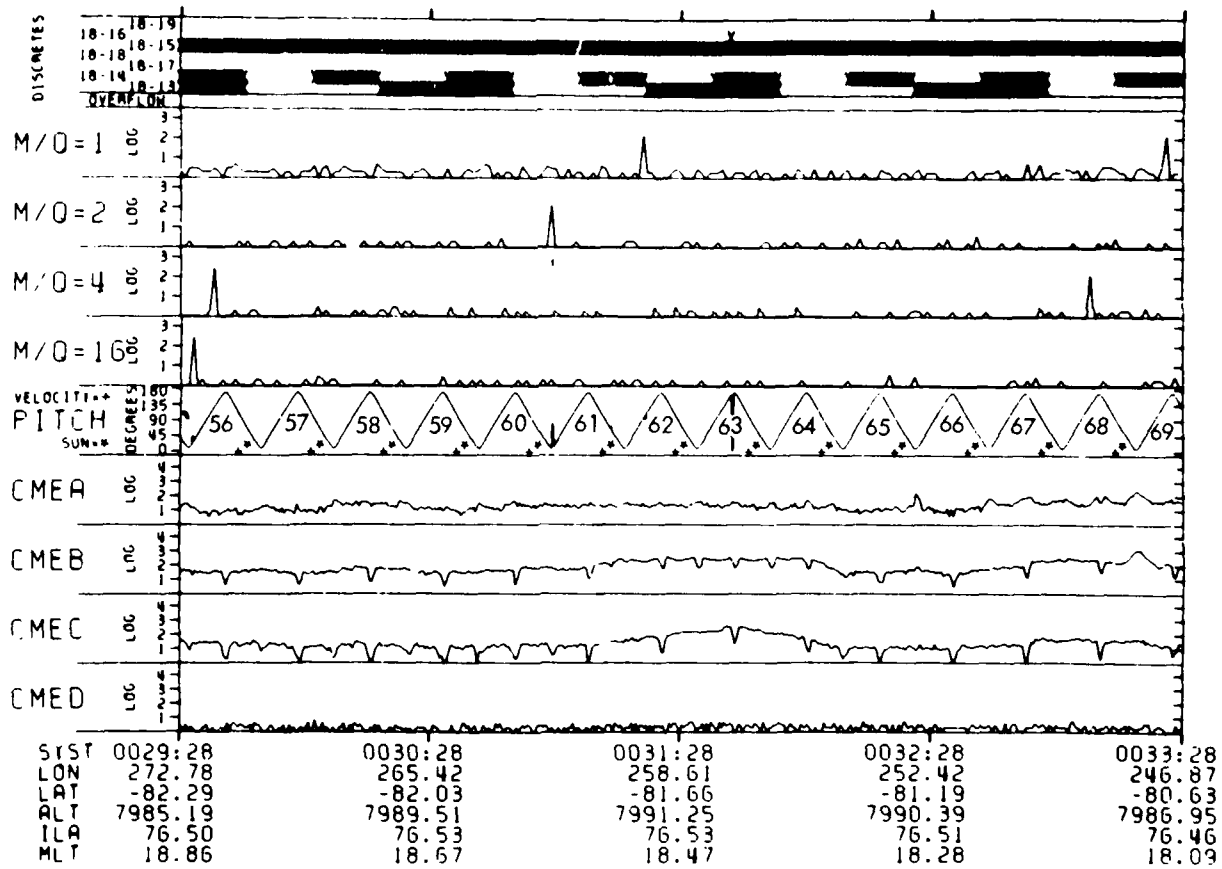


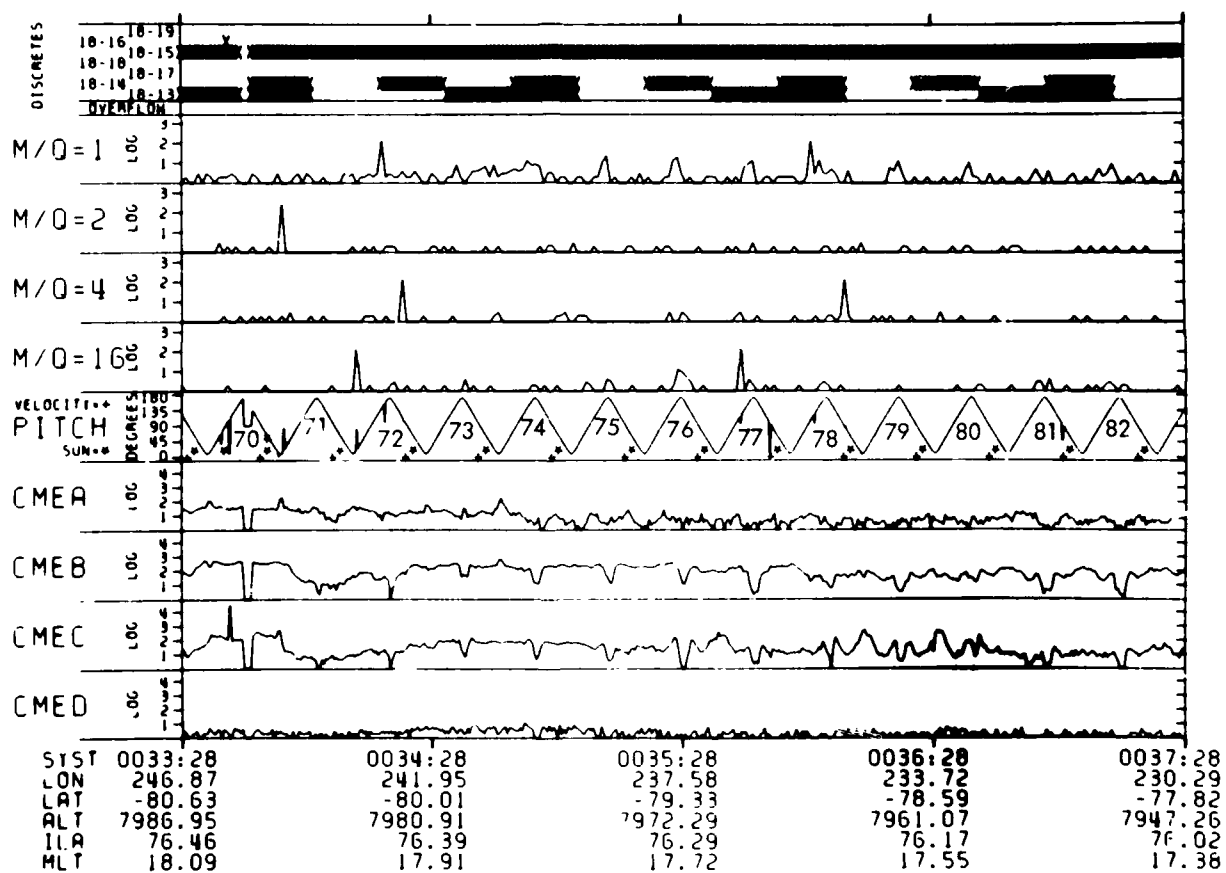
Figure 4. Survey plot of Lockheed data obtained with the S3-3 satellite on a tangential pass through a field-aligned current region on 17 January 1977.

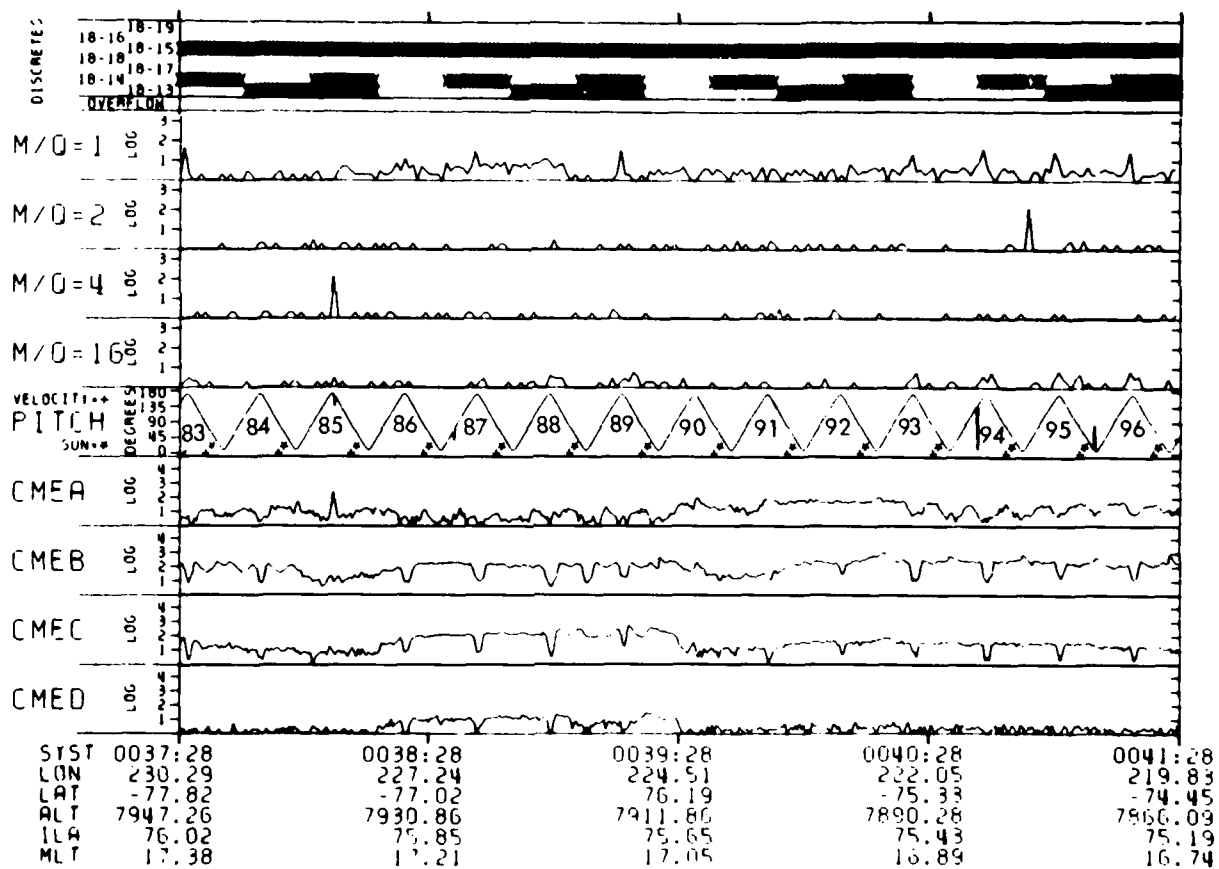


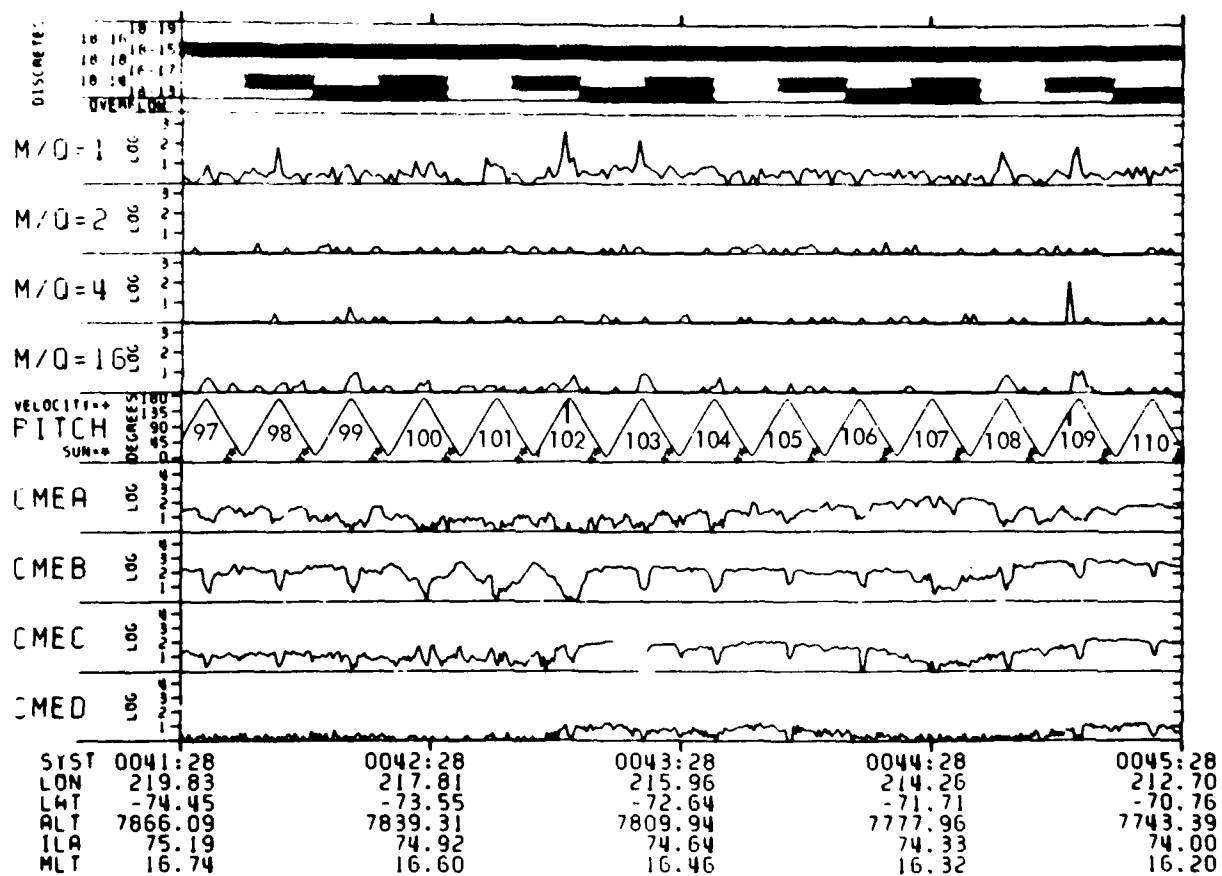


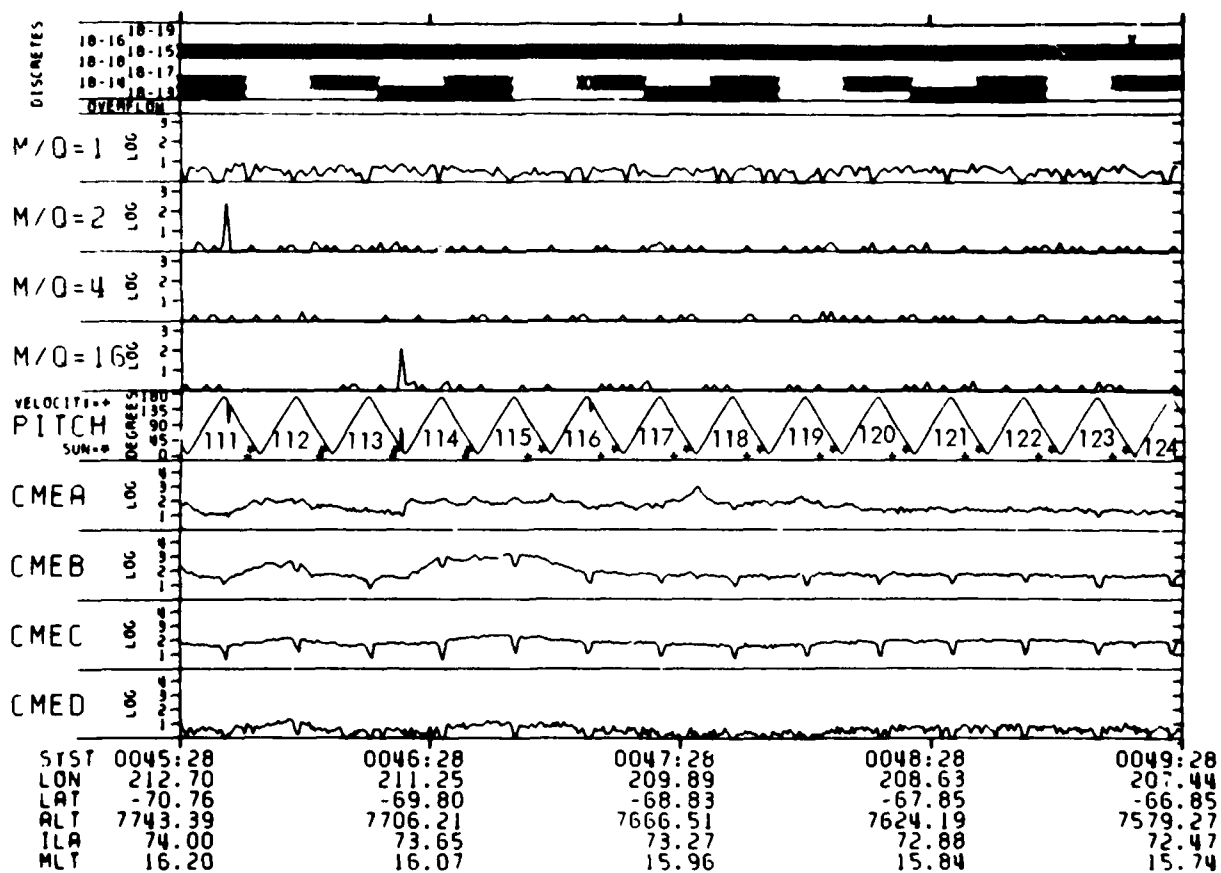












While examining the data, note the following types of features:

- (i) Field-aligned and conical pitch-angle distributions of $H^+(M/Q=1)$, $O^+(M/Q=16)$, and occasionally $He^+(M/Q=4)$ are present. For example, on spins 2, 3, and 4, the counting rates of H^+ and O^+ ions near $\alpha=180^\circ$ are appreciably above the noise level.
- (ii) The troughs in the CME counting rates centered at $\alpha=180^\circ$ are wider and deeper when the field-aligned ions appear. This widening and deepening of the loss cones of the electron distributions is due to an electrostatic potential difference along the magnetic field, below the satellite, that accelerates electrons downward and ions upward (Refs. 1 and 2). This effect is more pronounced for the lower energy electrons. Note, for example, that the electron loss cones are wider and deeper on spin 2 than they are on spin 1.
- (iii) The counting rates of the lower-energy detectors are sometimes symmetrical about $\alpha=90^\circ$, while the counting rates of the higher energy electrons are high near $\alpha=0^\circ$ and have local minima at $\alpha=90^\circ$. Such distributions indicate the presence of electrostatic potential differences above the satellite that accelerate electrons downward (Refs. 1 and 2). The symmetrical distributions are due to electrons that are locally trapped by the magnetic field below the satellite and the electric field above. Note, for example, that on spins 1, 2, and 3, the counting rates of the CMEB detector are symmetrical about 90° while the CMEC counting rates have maxima near 0° and local minima at 90° .
- (iv) The CMEC counting rate becomes modulated when electron "spikes"—high fluxes of electrons closely aligned with the magnetic field—appear. Such field-aligned electrons are usually observed moving simultaneously upward and downward along the magnetic field, with comparable fluxes in both directions (Ref. 18 and 19). On spins 7, 8, and 9, the spikes are directed only upward, as indicated by the CMEA and CMEB counting rates. The largest spikes (both up and down) appear on spins 47-54.

2. ANALYSIS OF DATA

In references 1 and 2 several methods were used to determine the potential differences above and below the satellite in order to evaluate the effects of some of the uncertain parameters, such as the shape of the potential along the magnetic field, the electron spectrum in the electric-field-free region, and interaction of the electrons with the wave turbulence. Now that this groundwork has been done, the most direct methods can be used to estimate the potential differences. Accordingly, in this analysis, the potential differences below the satellite were determined from the loss cone widths.

It will be recalled that at two points, (B_s, ϕ_s) and (B, ϕ) , along the dynamical trajectory of an electron, the energy, w , and pitch angle, α , of the electron are related by the equations expressing the conservation of the magnetic moment of the electron and the total energy, viz.,

$$\frac{w_s}{B_s} \sin^2 \alpha_s = \frac{w}{B} \sin^2 \alpha \quad (2)$$

$$\text{and} \quad w = w_s + e(\phi - \phi_s) \quad (3)$$

Here, B is the magnetic field intensity, ϕ is the electrostatic potential, and e is the absolute value of the electron charge. The subscript, s , denotes the values of the parameters at the location of the satellite. Hence, if B_t designates the limiting field intensity at the "top" of the atmosphere where the electron mirrors before suffering collisional effects, and where $\phi = \phi_m$, the edge of the loss cone, $\alpha_s = \alpha_c$, is given by the equation

$$\alpha_c = \sin^{-1} \left[\frac{B_s}{B_t} \left(1 + \frac{e(\phi_m - \phi_s)}{w_s} \right) \right]^{1/2} \quad (4)$$

The potential ϕ , toward lower altitudes, is assumed to increase monotonically from 0 to its maximum value, ϕ_m , and then to remain constant.

This equation was used to determine $\phi_m - \phi_s$. Generally, the CMEB detector, which has a high counting rate and is sensitive to a relatively narrow range of electron energies, was used to determine α_c . For this detector the energy 0.9 keV was used for w_s . However, the value of α_c obtained from the CMEC counting rate was often used to verify results. For this detector, the energy 1.8 keV was used for w_s in Eq. (4). The 48-term Jensen and Cain magnetic field model for 1972 (Ref. 20) was used to determine the values of B_s and B_t on the field lines traversed by the satellite trajectory. B_t was evaluated at the altitude of 200 km. The ratio B_s/B_t along the satellite trajectory, as a function of the satellite altitude, is shown in Figure 5.

The potential ϕ_s at the satellite and the value of B_1 above the satellite where $\phi = 0$, were estimated from the CMEC counting rate by assuming the primary electrons at B_1 to be isotropic in the downward hemisphere and to have a Maxwellian distribution with a temperature, w_e , equal to 1 keV. Such a distribution is consistent with many samples of the data obtained at times when the potential was zero. The directional flux of these electrons at the satellite, B_s , from Liouville's theorem, is

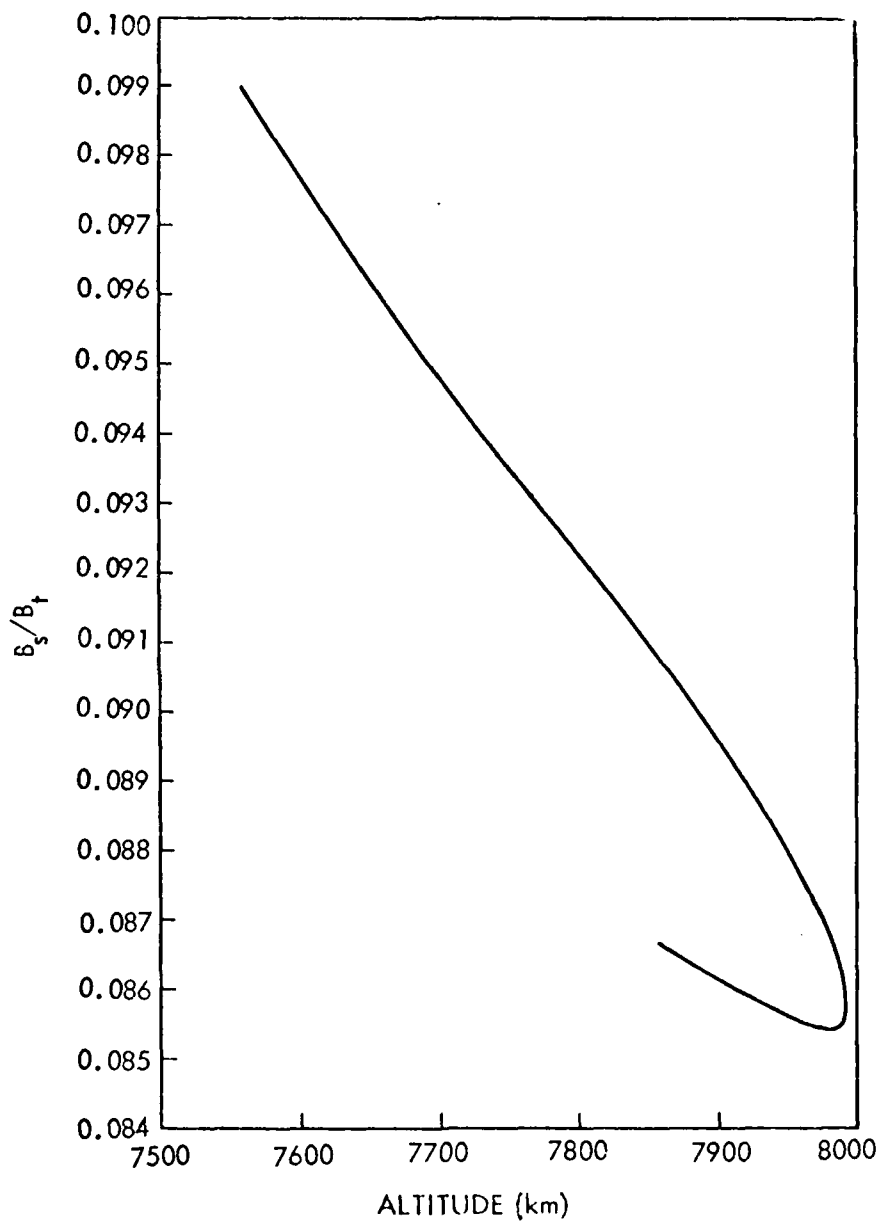


Figure 5. Magnetic-field ratio B_s/B_t as function of satellite altitude.

$$j(w_s, \alpha_s, B_s) = \frac{n_o w_s}{(2\pi^3 m w_e)^{1/2}} \exp \left[-(w_s - e\phi_s)/w_e \right] \quad (5)$$

where, from the conservation of the magnetic moment,

$$\alpha_s = \sin^{-1} \left[\left(1 - \frac{e\phi_s}{w_s} \right) \frac{B_s}{B_1} \sin^2 \alpha_1 \right]^{1/2} \quad (6)$$

for $w_s \geq e\phi_s$. Here, α_1 is the pitch angle of the electrons at B_1 . The counting rate of the CMEC detector due to this flux is given by the integral,

$$C(\alpha_s) = G \int_{w_1}^{5 \text{ keV}} j(w_s, \alpha_s, B_s) dw_s \quad (7)$$

$G = 5.4 \times 10^{-6} \text{ cm}^2 \text{ sr}$ is the geometric factor of the detector, and w_1 is the larger of $w_L = 1.6 \text{ keV}$ (the low-energy limit of the detector bandpass) or

$$w_1 = \frac{e\phi_s}{1 - \frac{B_1}{B_s} \sin^2 \alpha_s} \quad (8)$$

which follows from (6) for $\alpha_1 = 90^\circ$. Note that the flux given by (5) is constant over the pass band of the detector in the pitch-angle range $0 \leq \alpha_s \leq \alpha_L$, where α_L follows from (8) for $w_1 = w_L$. Hence, the counting rate of the detector should be constant in that pitch angle interval. The situation is illustrated in Figure 6 which depicts the response of the detector as a function of pitch angle, on the contours of constant flux obtained by transforming the isotropic flux from $B_1, \phi = 0$ to B_s, ϕ_s . The relationship between ϕ_s and B_1 at the limit of the constant counting-rate interval, given by the equation

$$e\phi_s = w_L \left(1 - \frac{B_1}{B_s} \sin^2 \alpha_L \right) \quad (9)$$

is valid for an isotropic flux at B_1 , regardless of the energy distribution.

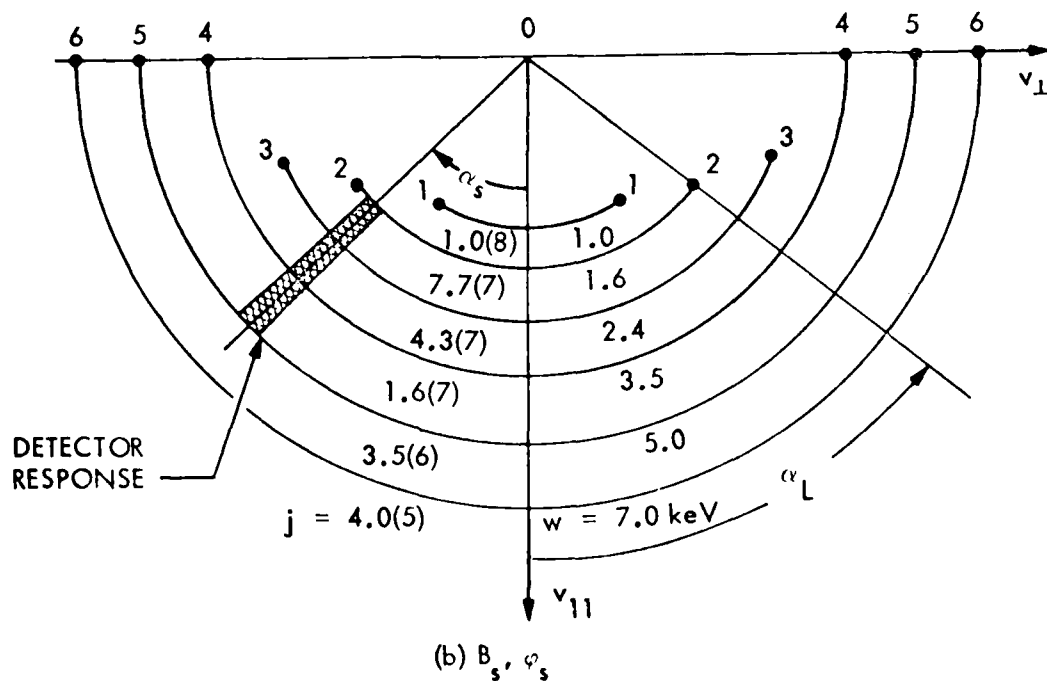
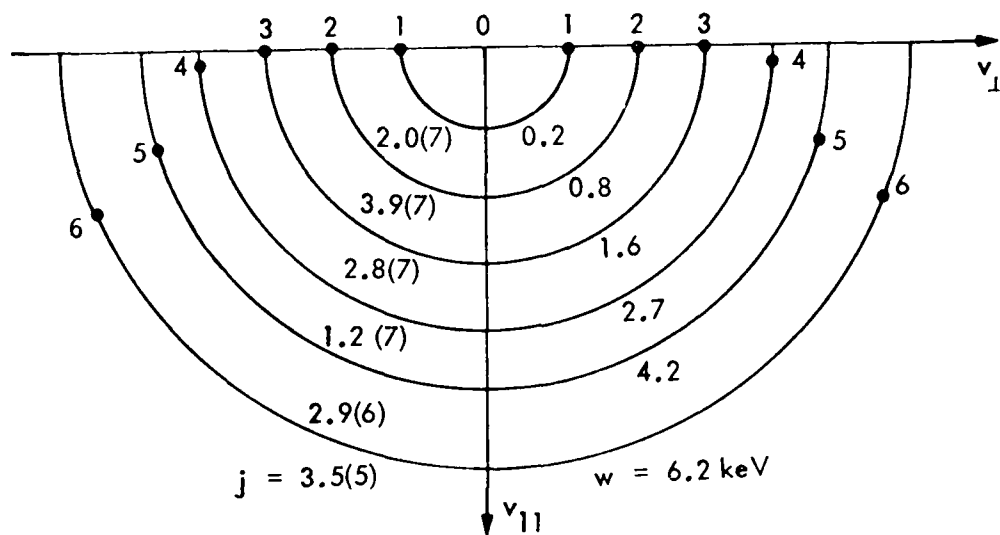


Figure 6. Illustration of transformation of flux which is isotropic at $B_1, \phi = 0$ to B_s, ϕ_s , where $B_1/B_s = .77$ and $\phi_s = .8$ kV. The flux contours between the numbered dots in (a) correspond to the contours between the correspondingly numbered dots in (b). Note that the counting rate of the detector, which responds to energies 1.6 to 5.0 keV, is constant between $\alpha = 0$ to $\alpha = \alpha_L$.

By putting (5) into (7) and integrating for $\alpha_s = \alpha_L$ and $\alpha_s = 90^\circ$, the ratio $C(\alpha_L)/C(90^\circ)$ is found to be,

$$\frac{C(\alpha_L)}{C(90^\circ)} = \frac{(1 + 1.6) \exp(-1.6) - (1 + 5.0) \exp(-5.0)}{(1 + w_1) \exp(-w_1) - (1 + 5.0) \exp(-5.0)} \quad (10)$$

where w_1 is given by Eq. (8) for $\alpha_s = 90^\circ$, i.e.,

$$w_1 = \frac{e\phi_s}{1 - B_1/B_s} \quad (11)$$

The ratio $C(\alpha_L)/C(90^\circ)$ is plotted against w_1 in Figure 7. The straight lines in Figure 8 give the potential ϕ_s as a function of B_1/B_s for fixed values of w_1 . By eliminating ϕ_s from Eqs. (9) and (11), we obtain

$$\sin^2 \alpha_L = \frac{B_s}{B_1} \left[1 - \frac{w_1}{w_L} \left(1 - \frac{B_1}{B_s} \right) \right] \quad (12)$$

The curves in Figure 8 show the values of α_L as a function of B_1/B_s for fixed values of w_1 . Hence, ϕ_s and B_1/B_s for values of $e\phi_s \leq w_L = 1.6$ keV, are determined from the measured values of α_L and $C(\alpha_L)/C(90^\circ)$ as follows: the value of w_1 corresponding to the counting-rate ratios is obtained from the graph of Figure 7; B_1/B_s corresponding to α_L and w_1 is obtained from Figure 8; the ϕ_s corresponding to the same values of B_1/B_s and w_1 is read off the graph in Figure 8.

For $e\phi_s > w_L$ the peak of the CMEC counting rate is at $\alpha=0$, and we do not have sufficient information from this detector alone to determine ϕ_s and B_1/B_s separately. However, we can determine the lower and upper limits of these values. The counting rate ratio, $C(0^\circ)/C(90^\circ)$, of the CMEC detector now becomes

$$\frac{C(0^\circ)}{C(90^\circ)} = \frac{(1 + e\phi_s) \exp(-e\phi_s) - (1 + 5.0) \exp(-5.0)}{(1 + w_1) \exp(-w_1) - (1 + 5.0) \exp(-5.0)} \quad (12)$$

After substituting Eq. (11) for w_1 , this equation was solved numerically for ϕ_s for various values of $R = C(0^\circ)/C(90^\circ)$ and B_1/B_s . The results are shown in Figure 9, where ϕ_s is plotted against B_1/B_s for fixed values of R . This

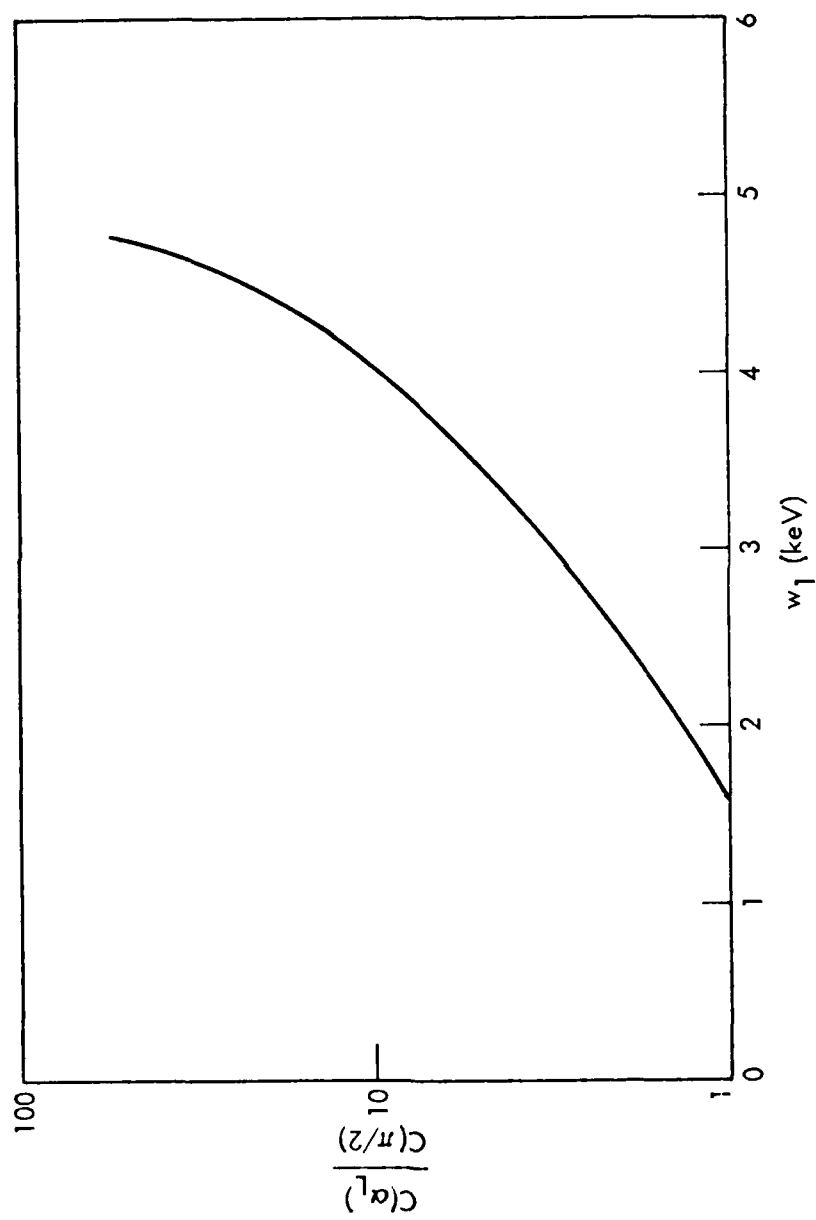


Figure 7. Counting-rate ratio $C(\alpha_L)/C(90^\circ)$ versus w_1 .

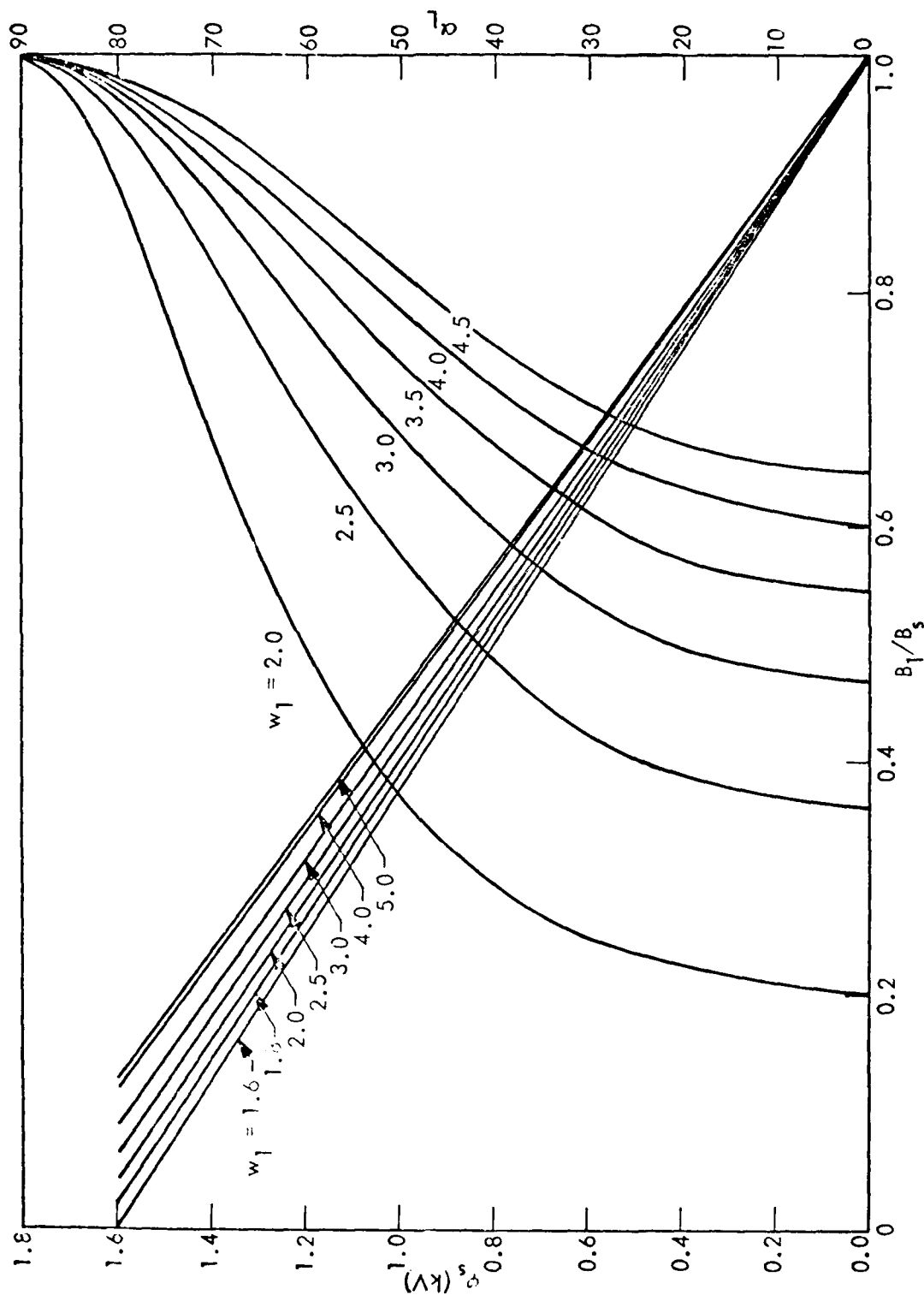


Figure 8. The potential ϕ_s (straight lines) and pitch angle α_L (curves) are plotted versus B_1/B_s for various fixed values of w_1 .

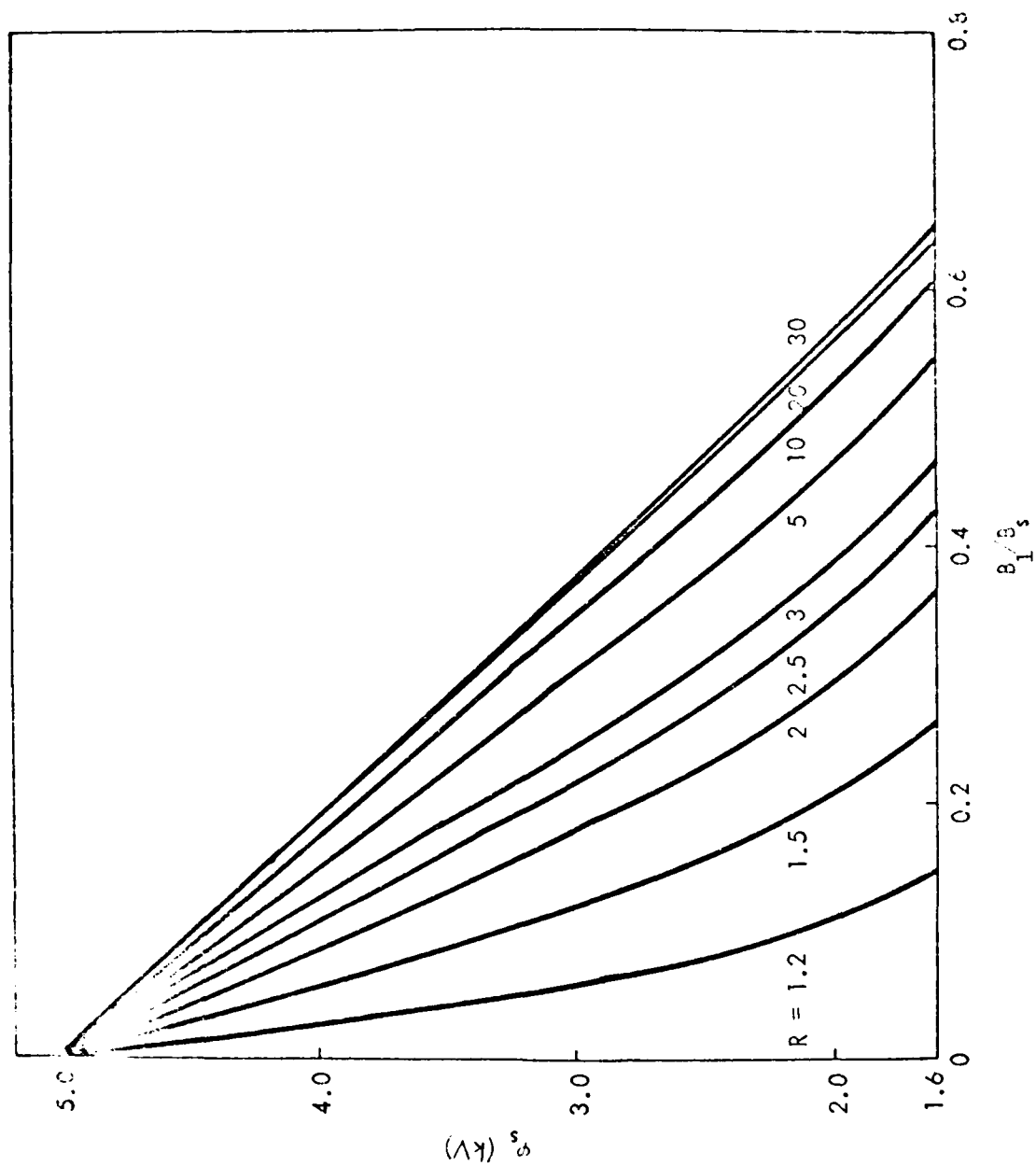


Figure 9. The potential ϕ_s versus B_1/B_s for fixed values of the counting-rate ratio R .

figure shows that for $R \geq 1$, ϕ_s is between 1.6 - 5.0 kV, and B_1/B_s is between 0 and the limiting value $(B_1/B_s)_L$ given by the intercept of the appropriate R curve at the abscissa. If $\phi_s \geq 5$ kV the minimum energy of the primary electrons would exceed the sensitivity band of the detector and its response to these electrons would be zero. Its counting rate would then be symmetrical about $\alpha=90^\circ$ since it would respond only to the lower energy electrons resulting from interactions in the atmosphere and local trapping. In this case the potential above the satellite can be estimated by applying the methods described above to the counting rates of the CMED detector if those rates are sufficiently above the noise.

3. RESULTS

In Figure 10 the potential difference $\phi_m - \phi_s$ is plotted against the satellite spin number. The scale at the top of the figure gives the invariant latitude and magnetic local time. Near the top of the figure the shading indicates the ranges over which the field-aligned ions (FAI) are observed, and the asterisks denote the more isolated occurrences of the conical ion distributions (CID). The potential differences are quite variable and at times very high, exceeding 8 kV on one spin period. Note also that the field-aligned ions are observed whenever $e(\phi_m - \phi_s)$ approximately exceeds the energy threshold of the ion spectrometers.

The regions in which the high electron fluxes (spikes), both near $\alpha=0$ and $\alpha=180^\circ$, are observed are also shown in the figure. Note that these spikes generally occur when $\phi_m - \phi_s$ is very small. The source of the spikes has not yet been determined, but we believe they may be due to toroidal, MHD turbulence, which accelerates electrons in both directions along the magnetic field.

The potential difference above the satellite is shown in Figure 11 as a function of the satellite spin number. These values of ϕ_s vary in approximately the same manner as those in Figure 12. An important difference, however, is that the potential ϕ_s is always high just preceding the occurrences of the electron spikes. The magnetic field ratios B_1/B_s were found to be less than 0.78, with most of the separately-determined values being between about 0.55 and 0.70.

The variations of the potential differences shown in Figures 10 and 11 are too rapid to be ascribed to the spatial (altitude and invariant latitude) or magnetic local-time variations of the satellite. As described in References 1 and 2 the potential differences were found to have an inverted-V structure, a few degrees wide in invariant latitude. Furthermore, since this current sheet is associated with the discrete aurorae, rapid variations are not expected within the current sheet in the longitudinal direction. The rapid variations are therefore more likely due to oscillatory motions of the magnetic shell containing the field-aligned currents. Observations of oscillations, principally with periods of 2 to 7 minutes, of the magnetic field at high latitudes and in the motion of the magnetopause suggest that the high latitude field lines fluctuate with such periods. The variations

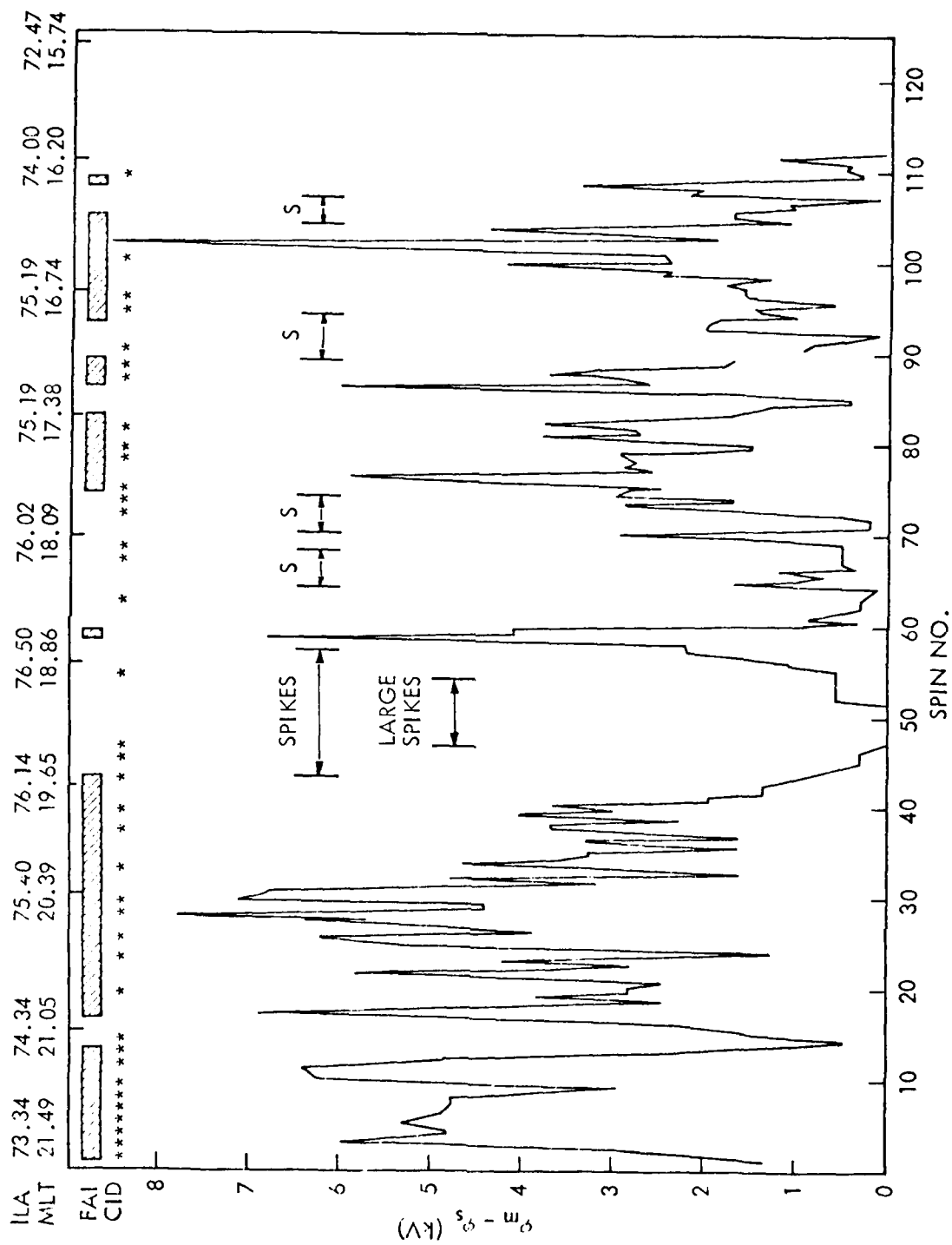


Figure 10. Potential difference below satellite as function of satellite spin number. The invariant latitude and magnetic local time are shown at the top of the graph. Observations of the field-aligned ions (FAI) and conical ion distributions (CID) are indicated near the top of the figure. The locations of the electron spikes are also shown in the figure.

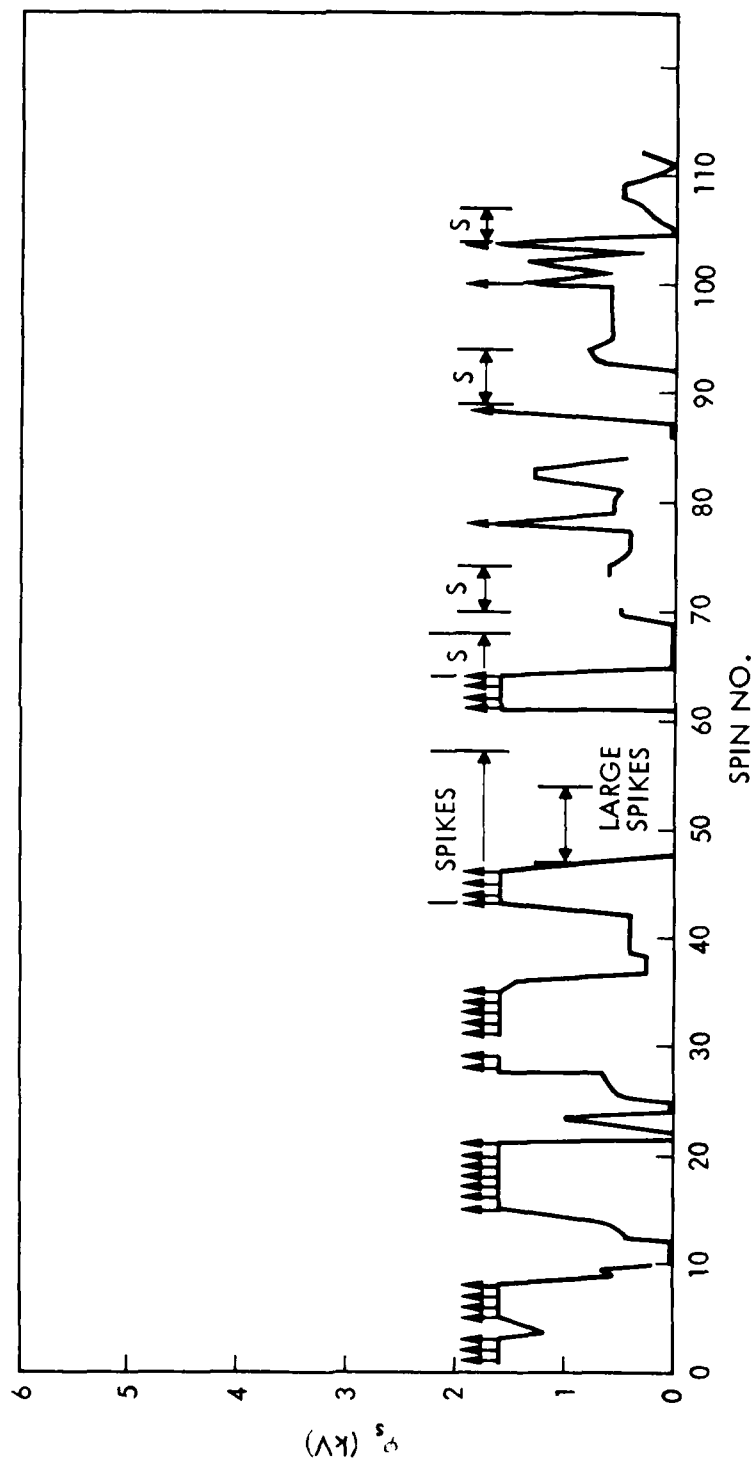


Figure 11. The potential difference above the satellite as a function of the satellite spin number. The arrows indicate that the ϕ_s is between 1.6 and 5.0 keV.

of the potentials in Figures 10 and 11 appear to be consistent with fluctuations of this type.

The effect of the variation of the invariant latitude of the satellite is indicated by the general lowering of the activity at invariant latitudes higher than about 76.2° . The data described in References 1 and 2 display an electron spike at the high latitude boundary of the potential structure. The regions of the spikes shown in Figures 10 and 11, especially the locations of the large spikes appear to denote the high latitude region of the potential structure.

Our interpretation of the results is, therefore, as follows. On spin zero the satellite entered the region in which the narrow potential structure, due to the current-driven instability, was fluctuating in the latitudinal direction. On spin numbers 43-74 the satellite had generally cleared the region, on the high-latitude side, except for the surge of the current sheet that occurred in the vicinity of spin number 58. The satellite then again traversed that region as it moved toward lower latitudes and earlier magnetic local times. The potentials were generally higher during the local evening than during the local afternoon.

SECTION IV

ANALYSIS OF ION DISTRIBUTIONS

1. PITCH-ANGLE DIFFUSION IN PRESENCE OF ELECTRIC FIELDS

Pitch-angle diffusion is customarily treated with a Fokker-Planck diffusion equation for the phase space distribution function, f . Since the principal observables are kinetic energy, w , and pitch-angle, α , f is usually regarded as a function of w and α . However, the proper physical variables are the constants of motion, in this case the adiabatic invariants. To see how this affects the form of the Fokker-Planck equation, consider pitch-angle diffusion in a divergent magnetic field with energy conservation (i.e. trapped electrons in a VLF-ELF wave field; see Kennel and Petschek, Ref. 21). The local interactions are described by the homogeneous field equation,

$$\frac{Df}{Dt} = \frac{1}{\sin \alpha} \frac{\partial}{\partial \alpha} \left[D_{\alpha\alpha} \sin \alpha \frac{\partial f}{\partial \alpha} \right] \quad (13)$$

where Df/Dt is the total derivative,

$$\frac{Df}{Dt} = \frac{\partial f}{\partial t} + \vec{V} \cdot \nabla f \quad (14)$$

Equation (13) cannot represent the variation of the distribution along the magnetic field direction because α is not an adiabatic invariant variable. The pitch-angle at the equator, α_0 , is an adiabatic invariant variable, so the non-local analog of Equation (13) is,

$$\frac{\partial f(\alpha_0)}{\partial t} = \frac{1}{\tau_b \sin 2\alpha_0} \frac{\partial}{\partial \alpha_0} \left[\bar{D}_{\alpha_0 \alpha_0} \tau_b \sin 2\alpha_0 \frac{\partial f(\alpha_0)}{\partial \alpha_0} \right] \quad (15)$$

where τ_b is the bounce period, and $\bar{D}_{\alpha_0 \alpha_0}$ a bounce averaged diffusion coefficient.

In the presence of two non-stochastic effects, a divergent magnetic field and a parallel electric field, we must find new constants of the motion. Conservation of the first adiabatic invariant (magnetic moment) gives a constant C_1 :

$$C_1 B = w_{\perp}^2 = w^2 \sin^2 \alpha \quad (16)$$

where w_{\perp} and w_{\parallel} represent the (non-relativistic) components of w . Motion along the field direction must preserve the total energy, kinetic plus potential. If ϕ is the total potential energy (charge e times electric potential ϕ) we have the definition of another constant C_2 :

$$C_2 - C_1 B - \psi = w_{\parallel} = w(1 - \sin^2 \alpha) \quad (17)$$

the zero point for ψ is arbitrary, so we can choose the equator to be the point where $\psi = 0$. This allows us to construct, from the above equations, two new constants of motion,

$$U = 1 - \frac{B_0}{B} \frac{w_{\perp}}{w_{\perp} + w_{\parallel} + \psi} \quad (18)$$

$$K = w + \psi \quad (19)$$

where B_0 is the magnetic field at the equator (or $\psi = 0$ point). Clearly U is related to α_0 , for it becomes equal to $\cos^2 \alpha_0$ at the equator; i.e. the second term on the right hand side of (18) becomes w_{\perp}/w , which is equal to $\sin^2 \alpha_0$.

The derivative operator of Equation 13 is

$$\frac{\partial}{\partial \alpha} = \frac{\partial K}{\partial \alpha} \left(\frac{\partial}{\partial K} \right)_U + \frac{\partial U}{\partial \alpha} \left(\frac{\partial}{\partial U} \right)_K \quad (20)$$

Substituting this in the diffusion equation gives

$$\frac{Df}{Dt} = 4 \frac{K-\psi}{K} \frac{B_0}{B} \left| 1 - (1-U) \frac{K}{K-\psi} \frac{B}{B_0} \right|^{\frac{1}{2}} \frac{\partial}{\partial U} \left\{ D_{\alpha\alpha} \left| 1 - (1-U) \frac{K}{K-\psi} \frac{B}{B_0} \right|^{\frac{1}{2}} (1-U) \frac{\partial f}{\partial U} \right\} \quad (21)$$

where f must be a function of $w - K$ and U . Note, however that (21) is still a local diffusion equation.

To obtain the bounce-averaged equation integrate over the particle's trajectory. The element of length is $ds/\cos \alpha$, where ds is the increment along the magnetic field; the integral is

$$\oint \frac{DF}{dt} \frac{ds}{\cos \alpha} = 4 \oint ds \frac{B_0}{B} \frac{K-\psi}{K} \frac{\partial}{\partial U} \left\{ D_{\alpha\alpha} \left| 1 - (1-U) \frac{B}{B_0} \frac{K}{K-\psi} \right|^{\frac{1}{2}} (1-U) \frac{\partial f}{\partial U} \right\} \quad (22)$$

$$= \frac{1}{T} \frac{\partial}{\partial U} \left| \bar{D}_{UU} T \frac{\partial f}{\partial U} \right| \quad (23)$$

$$\bar{D}_{UU} = \frac{1}{2T} \int_{s_1}^{s_2} D_{\alpha\alpha} 4 \left(\frac{B_0}{B} \frac{K-\psi}{K} \right)^2 \sin^2 \alpha \cos^2 \alpha \frac{ds}{\cos \alpha} \quad (24)$$

where s_1 and s_2 are the locations of the conjugate mirror points, and T is the quarter-bounce integral,

$$T = \frac{1}{R_0} \int_{s_1}^{s_2} \frac{ds}{\cos \alpha} \quad (25)$$

R_0 is the distance from the center of the earth to the equatorial crossing of the magnetic field line.

The development of Equation (22) is the same as for Equation (15), as can be seen immediately by letting $\psi \sim 0$ and $U \sim \cos^2 \alpha_0$. The left side of the equation is not so simple, however, because the electric field can raise or lower the mirror point. If the mirror points are both above the atmosphere, the effects of absorption can be neglected and the $\vec{V} \cdot \nabla f$ term is near zero. If either mirror point dips into the atmosphere, the absorption contributes a term of order

$$\frac{1}{T} \vec{V} \cdot \int \nabla f \frac{ds}{\cos \alpha} \approx \frac{1}{T} V \int \frac{\partial f}{\partial s} ds \approx \frac{f}{\tau_b} \quad (26)$$

The diffusion equation above is appropriate to interactions with electromagnetic (cyclotron-mode) waves that approximately preserve the particle energy. Other waves, such as transverse electrostatic waves, primarily alter the perpendicular component of momentum. The local equation is then,

$$\frac{Df}{Dt} = \frac{\partial}{\partial w_{\perp}} \left(D_{w_{\perp} w_{\perp}} \frac{\partial f}{\partial w_{\perp}} \right) \quad (27)$$

In this case there is no simple decomposition into an adiabatic invariant equation with a single degree of freedom (as in (15) or (22)). This can be seen most readily by finding dU/dK and noting that it is not a single-valued function of U and K . The rightside must comprise several terms, including cross terms with two different derivatives. It is highly unlikely that analytic solutions exist; even numerical solutions are difficult in an inhomogeneous magnetic field.

A useful set of variables is K and

$$M = w_{\perp} \frac{B_0}{B} \quad (28)$$

This is simply the first adiabatic invariant, in energy units. The differential operator is

$$\frac{\partial}{\partial w_{\perp}} = \frac{B_0}{B} \left(\frac{\partial}{\partial M} \right)_K + \left(\frac{\partial}{\partial K} \right)_M \quad (29)$$

The diffusion equation becomes

$$\begin{aligned} \frac{Df}{Dt} = & \left(\frac{B_0}{B} \frac{\partial}{\partial M} + \frac{\partial}{\partial K} \right) \left[D_{\perp\perp} \left(\frac{B_0}{B} \frac{\partial}{\partial M} + \frac{\partial}{\partial K} \right) f \right] = \left(\frac{B_0}{B} \frac{\partial D_{\perp\perp}}{\partial M} + \frac{\partial D_{\perp\perp}}{\partial K} \right) \left(\frac{B_0}{B} \frac{\partial f}{\partial M} + \frac{\partial f}{\partial K} \right) \\ & + D_{\perp\perp} \left(\frac{B_0^2}{B^2} \frac{\partial^2 f}{\partial M^2} + 2 \frac{B_0}{B} \frac{\partial^2 f}{\partial M \partial K} + \frac{\partial^2 f}{\partial K^2} \right) \end{aligned} \quad (30)$$

The cross terms cannot, of course, be eliminated, so the equation can have all combinations of first and second derivatives on the right.

2. DIFFUSION COEFFICIENTS FOR INTERACTIONS WITH ELECTROSTATIC WAVES

The Fokker-Planck equation for interactions that alter the perpendicular and parallel parts of a particle's energy is (Chandrasekhar, Ref. 23),

$$\begin{aligned} \frac{Df}{Dt} = & - \frac{\partial}{\partial w_{\perp}} f \langle \Delta w_{\perp} \rangle - \frac{\partial}{\partial w_{\parallel}} f \langle \Delta w_{\parallel} \rangle + \frac{1}{2} \frac{\partial^2}{\partial w_{\perp}^2} f \langle (\Delta w_{\perp})^2 \rangle + \frac{\partial^2}{\partial w_{\perp} \partial w_{\parallel}} f \langle \Delta w_{\perp} \Delta w_{\parallel} \rangle \\ & + \frac{1}{2} \frac{\partial^2}{\partial w_{\parallel}^2} f \langle (\Delta w_{\parallel})^2 \rangle \end{aligned} \quad (31)$$

The notation $\langle \Delta X \rangle$ for the Fokker-Planck coefficients denotes a time average of the changes in X, per unit time. If the waves affect only one component, Δw , the w terms disappear. An equilibrium solution of the remaining equation is $\partial f / \partial t = 0$, $f = \text{constant}$. This gives a relation between the Fokker-Planck coefficients,

$$\frac{Df}{Dt} = 0 = - \frac{\partial \langle \Delta w_{\perp} \rangle}{\partial w_{\perp}} + \frac{1}{2} \frac{\partial^2 \langle (\Delta w_{\perp})^2 \rangle}{\partial w_{\perp}^2} \quad (32)$$

A solution of (32) is

$$D_{\perp\perp} = \frac{1}{2} \langle (\Delta w_{\perp})^2 \rangle \quad (33)$$

$$\frac{\partial D_{\perp\perp}}{\partial w_{\perp}} = \langle \Delta w_{\perp} \rangle \quad (34)$$

The Fokker-Planck equation can then be written as a diffusion equation

$$\frac{Df}{Dt} = \frac{\partial}{\partial w_{\perp}} \left(D_{\perp\perp} \frac{\partial f}{\partial w_{\perp}} \right) \quad (35)$$

Interactions of charged particles with transverse electrostatic waves may be assumed to affect only w_{\perp} . A particle of charge e in resonance with a transverse wave field, of amplitude E_w experiences a change in energy.

$$\begin{aligned}\Delta w_{\perp} &\approx \frac{1}{2} m v_{\perp} \Delta v_{\perp} \\ &\approx \frac{1}{2} m \sqrt{\frac{2w_{\perp}}{m}} \left(\frac{eE_w}{m} \right) \delta t \\ &= \sqrt{\frac{w_{\perp}}{2m}} (eE_w) \delta t\end{aligned}\quad (36)$$

If the wave and particle are out of resonance by an amount $\delta\omega$, they will remain in phase for a time of order

$$\delta t \approx \frac{\pi}{2\delta\omega} \quad (37)$$

Generally, except in a highly inhomogeneous field, the interaction time is set by relation (37). The diffusion coefficient follows upon taking a time average of $(\Delta w_{\perp})^2$, thus,

$$D_{\perp\perp} \approx \frac{1}{2} \left\langle \frac{w_{\perp}}{2m} (eE_w \delta t)^2 \right\rangle / \delta t \approx \frac{\pi e^2}{8} \frac{w_{\perp}}{m} \frac{\langle E_w^2 \rangle}{\delta\omega} \quad (38)$$

The last term on the right has the form of a power spectrum. The average wave power in a band of width $\delta\nu = \delta\omega/2$ is the power spectral density,

$$P_{\nu}^E \approx \frac{\langle E_w^2 \rangle}{2\delta\nu} \quad (39)$$

The diffusion coefficient therefore becomes,

$$D_{\perp\perp} \approx \frac{w_{\perp} e^2}{8m} P_{\nu}^E \quad (40)$$

The power spectral density of the broad-band electrostatic turbulence, in the region of the peak intensity (10 - 50 Hz), measured by Gurnett and Frank (Ref. 9) is about $5 \times 10^{-6} \text{ (V/m)}^2/\text{Hz}$. Substituting this value in (40) gives, for protons,

$$D_{\perp\perp} \approx 0.06 w \text{ (keV)}^2/\text{sec} \quad (41)$$

Here, the energy w_{\perp} is in keV. A more detailed analysis by Sturrock (Ref. 24) led to a similar form, with $D_{\perp\perp}$ proportional to w_{\perp} .

3. SOLVING THE DIFFUSION EQUATION

The local diffusion equation, (35), has the form,

$$\frac{\partial f}{\partial t} = \Gamma \frac{\partial}{\partial w_{\perp}} \left(w_{\perp} \frac{\partial f}{\partial w_{\perp}} \right) \quad (42)$$

The initial condition is that the distribution is a delta function at $w_{\perp} = 0$. The boundary condition at $w_{\perp} = 0$ is $w_{\perp} \partial f / \partial w_{\perp} = 0$. A solution that satisfies these conditions is

$$f \sim \frac{1}{\Gamma t} \exp(-w_{\perp} / \Gamma t) \quad (43)$$

This solution is useful for verifying the computational results at late time, but, unfortunately, the adiabatic invariant diffusion equation has no such simple solutions.

An alternative that avoids the difficulty of solving the diffusion equation is to return to the fundamental processes and trace the probable trajectories of individual particles. In our case a Monte Carlo technique is well suited to individual trajectories if the concept of mean deflection is invoked. We postulate that the deflection, δw_{\perp} , obeys a probability distribution (normalized to 1):

$$P(\delta w_{\perp}) = \frac{1}{\sqrt{2\pi} \sigma} \exp[-(\delta w_{\perp})^2 / 2\sigma^2] \quad (44)$$

This distribution is not based on physical principles, but rather has the expected form and a well-defined mean, σ^2 ; there are few processes in nature that strictly obey a normal (Gaussian) distribution. The critical restrictions on the use of the probability distribution, (44), are that the mean deflection be small compared with the scale, $f/(df/dw_{\perp})$, of the distribution and small compared with w_{\perp} . These conditions can be satisfied by choosing the time interval to be sufficiently small.

The Fokker-Planck coefficients are related to P . The diffusion coefficient is

$$D_{\perp\perp} = \frac{1}{2} \left\langle \frac{(\delta w_{\perp})^2}{\Delta t} \right\rangle \equiv \frac{1}{2\Delta t} \int_{-\infty}^{\infty} P(\delta w_{\perp}) (\delta w_{\perp})^2 d\delta w_{\perp} = \frac{\sigma^2}{2\Delta t} = w_{\perp} \Gamma \quad (45)$$

The probability distribution is now

$$P(\delta w_{\perp}) = \frac{1}{(4w_{\perp}\Gamma\Delta t)^{1/2}} \exp[-(\delta w_{\perp}) / (4w_{\perp}\Gamma\Delta t)] \quad (46)$$

A random variable, Q , uniformly distributed between 0 and 1, was determined from the cumulative probability distribution,

$$Q(\delta w_{\perp}) = \int_{-\infty}^{\delta w_{\perp}} P(x) dx \quad (47)$$

At the end of each predetermined time step, Δt , Q was set equal to a random number and (47) was solved for δw_{\perp} . Negative as well as positive values of δw_{\perp} were allowed. Negative values of w_{\perp} of course are not physically possible. Two methods were used to deal with this computational possibility. In one, the ions were assumed to be "absorbed" at $w_{\perp} < 0$, i.e. the case history was eliminated if w_{\perp} became negative. In the other, reflection about $w_{\perp} = 0$ was assumed; the sign of w_{\perp} was reversed if it became negative. The ion distributions computed on the basis of these widely different assumptions were essentially the same, undoubtedly because the diffusion coefficient favored the higher values of w_{\perp} .

The effect of the divergence of the magnetic field on the ion trajectories was taken into account by assuming that, between resonances, the adiabatic motions of the ions held. The following equations were used to compute the ion trajectories:

$$s_n = s_{n-1} + \Delta s_n \quad (48)$$

$$\Delta s_n = v_{\parallel n-1} \Delta t_n \quad (49)$$

$$\Delta \psi_n = e E_{\parallel} \Delta s_n \quad (50)$$

$$w_{\parallel n} = w_{\parallel n-1} + w_{\perp n-1} \left(1 - \frac{B_n}{B_{n-1}} \right) + \Delta \psi_n \quad (51)$$

$$w_{\perp n} = w_{\perp n-1} - w_{\perp n-1} \left(1 - \frac{B_n}{B_{n-1}} \right) + \delta w_{\perp n} \quad (52)$$

The program began by computing the trajectories of ions, with specified initial values of w_{\parallel} and w_{\perp} , from an altitude H_{so} , at the base of the source distribution, toward higher altitudes along the magnetic field. At certain "read-out" altitudes, H_{Ri} , above H_{so} , the characteristics of the ions were tabulated: the ions were accumulated in energy cells of widths $(\Delta w)_i$ and in pitch-angle cells of solid-angle widths $(\Delta \Omega)_i$. Also, the ions in each of the energy cells were further subdivided into pitch-angle cells of solid-angle widths $(\Delta \Omega)_k$. After the trajectories of N_0 ions, starting from H_{so} were computed and tabulated in this manner, the trajectories of $N_0 \exp[-\Delta H_s/H_{scale}]$ ions, starting from the altitude $H_{so} + \Delta H_s$, were computed, continuing the tabulation described above. Here, ΔH_s is the increment in the source altitude,

and H_{scale} is the scale height of the source. The computation continued, with ion trajectories starting at ever higher altitudes, until the source altitude exceeded the maximum readout altitude.

The incremental directional flux at a readout altitude due to the ions $\Delta N_{ik}(s_n)$ that originated at the altitude s_n within the volume element $A_n \Delta H_s$ is

$$\Delta j(w_i, \alpha_k; s_n) = \frac{\Delta N_{ik}(s_n)}{\Delta w_i \Delta \Omega_k A \cos \alpha_k \Delta t} \quad (53)$$

where A is the cross sectional area of the magnetic tube at the readout altitude. But, from the continuity equation,

$$\frac{\Delta N_{ik}}{A_n \Delta H_s} v_{o||} A_n = \frac{\Delta N_{ik}}{\Delta t} \quad (54)$$

where $v_{o||}$ is the initial parallel velocity component of the ions. By putting (54) into (53) and summing over the source altitudes s_n , the flux is given by the equation,

$$j(w_i, \alpha_k) = \frac{v_{o||} \sum_n \Delta N_{ik}(s_n)}{\Delta w_i \Delta \Omega_k A \cos \alpha_k \Delta H_s} \quad (55)$$

If ΔH_s would have been variable along the tube, the summation in (55) would have been over the ratio $\Delta N_{ik}(s_n)/\Delta H_{sn}$.

The following information was printed at each readout altitude:

- (i) the number of ions in the energy cells, N_i , and in the solid-angle cells, N_k ,
- (ii) the number of ions, N_i , in the energy cells divided by the widths Δw_i (this ratio is proportional to the energy distribution of the flux, i.e., to the summation of (55) over the k variables)

- (iii) the number of ions N_{ik} with energies in the i th cell and pitch-angles in the k th cell divided by $\Delta w_i \Delta \Omega_k \cos \bar{\alpha}_k$, where $\bar{\alpha}_k$ is the mean value of α in the k th cell (this ratio is proportional to j as given by Eq. 55), and,
- (iv) the number of ions N_k in the pitch-angle cells, for all energies, divided by $\Delta \Omega_k \cos \bar{\alpha}_k$ (this ratio is proportional to the pitch-angle distribution of the ions, i.e., to the summation of (55) over the i th variables.

4. RESULTS OF MONTE CARLO CALCULATION

The Monte Carlo program was first run with $E = 0$ and $\nabla B = 0$ to determine whether the numerical solution of the diffusion equation (42) would compare favorably with the analytical solution (43). The following parameters were used: heating rate, $\Gamma = .0283$ keV/sec; diffusion time, $t = 27.95$ sec; $\Delta t = .2795$ sec (100 collisions); initial energy, $w_{\perp 0} = .5$ keV; and number of case histories, $N = 500$. The resulting energy distribution, f , of the ions is shown in Figure 12. The straight line drawn in this figure has the slope $\Gamma t = .79$ keV, which is the form of the analytical solution. Note that the computed values (the open circles) follow the analytical solution quite well. Actually, the computed values are still somewhat elevated in the vicinity of .5 keV, the initial value of w_{\perp} . Hence, a shorter value of Δt (more collisions within the time t) would be desirable.

Note from (41) and (45) that the heating rate, Γ , used in this run is comparable to the value .06 keV/sec implied by the measurements.

A series of runs was then conducted, with $E_{\parallel} > 0$ and ∇B appropriate for the earth's field, to determine the effects of the model parameters on the energy and pitch-angle distributions of the ions. Combinations of the parameters were sought that would give distributions that are representative of the measured distributions. In references 1 and 2, three measurements of the energy distributions of the ion flux made during the S3-3 satellite traversal of the inverted-V potential structure are described. These energy spectra are reproduced in Figure 13. The spectra in the panels from left to right will be referred to by the numbers 1, 2, and 3, respectively. At the times of the measurements of the spectra 1, 2, and 3, the potential differences below the satellite, inferred from the electron distributions, were about .8, 2, and 2.5 keV, respectively. Using these potentials and typical observed wave-power

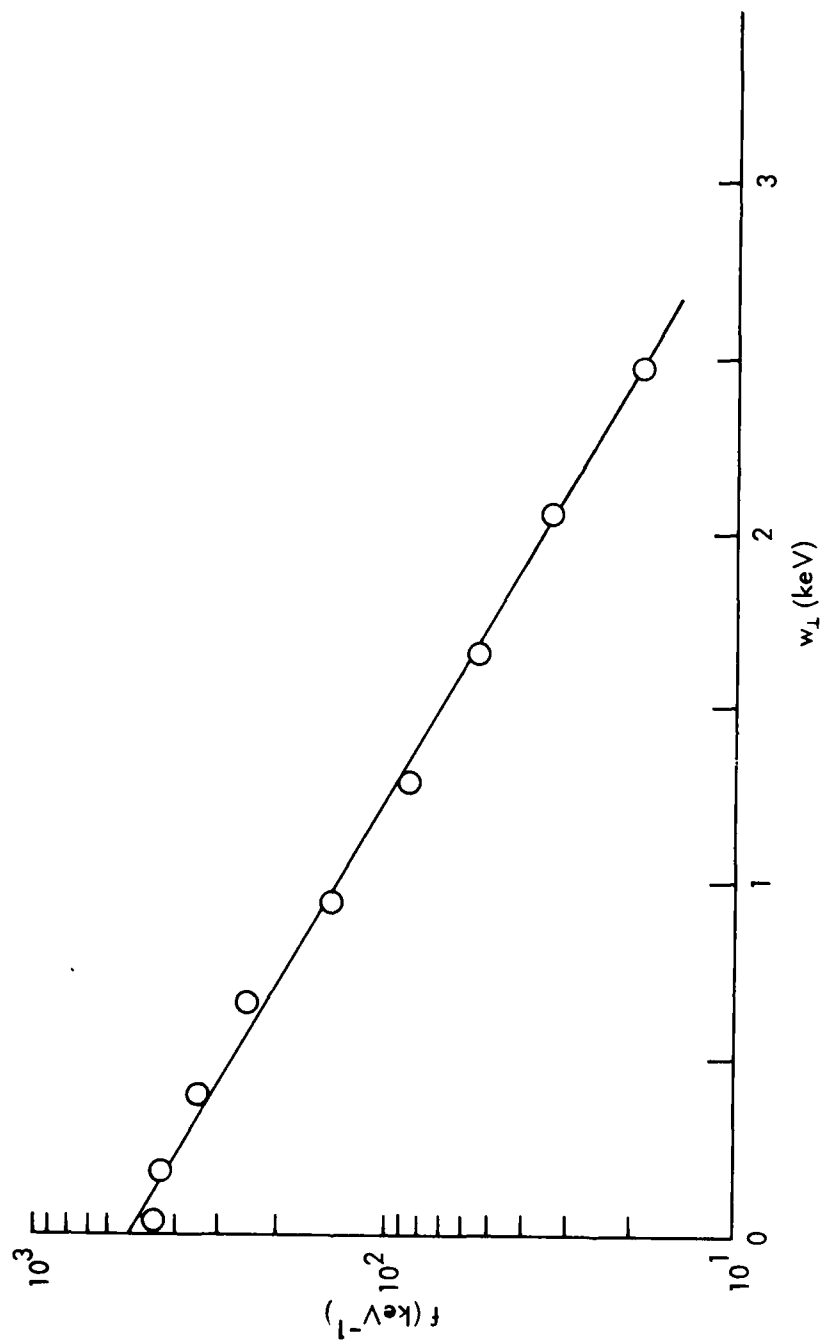


Figure 12. Energy distribution of ions (number of ions in energy cells divided by energy widths of cells). $E_M = 0$, $\gamma_B = 0$, $\Gamma = .0283$ keV/sec, $\Delta t = .2795$ sec, $w_{10} = .5$ keV, $N = 500$. The straight line is the analytical solution of the diffusion equation. The open circles are the computed points.

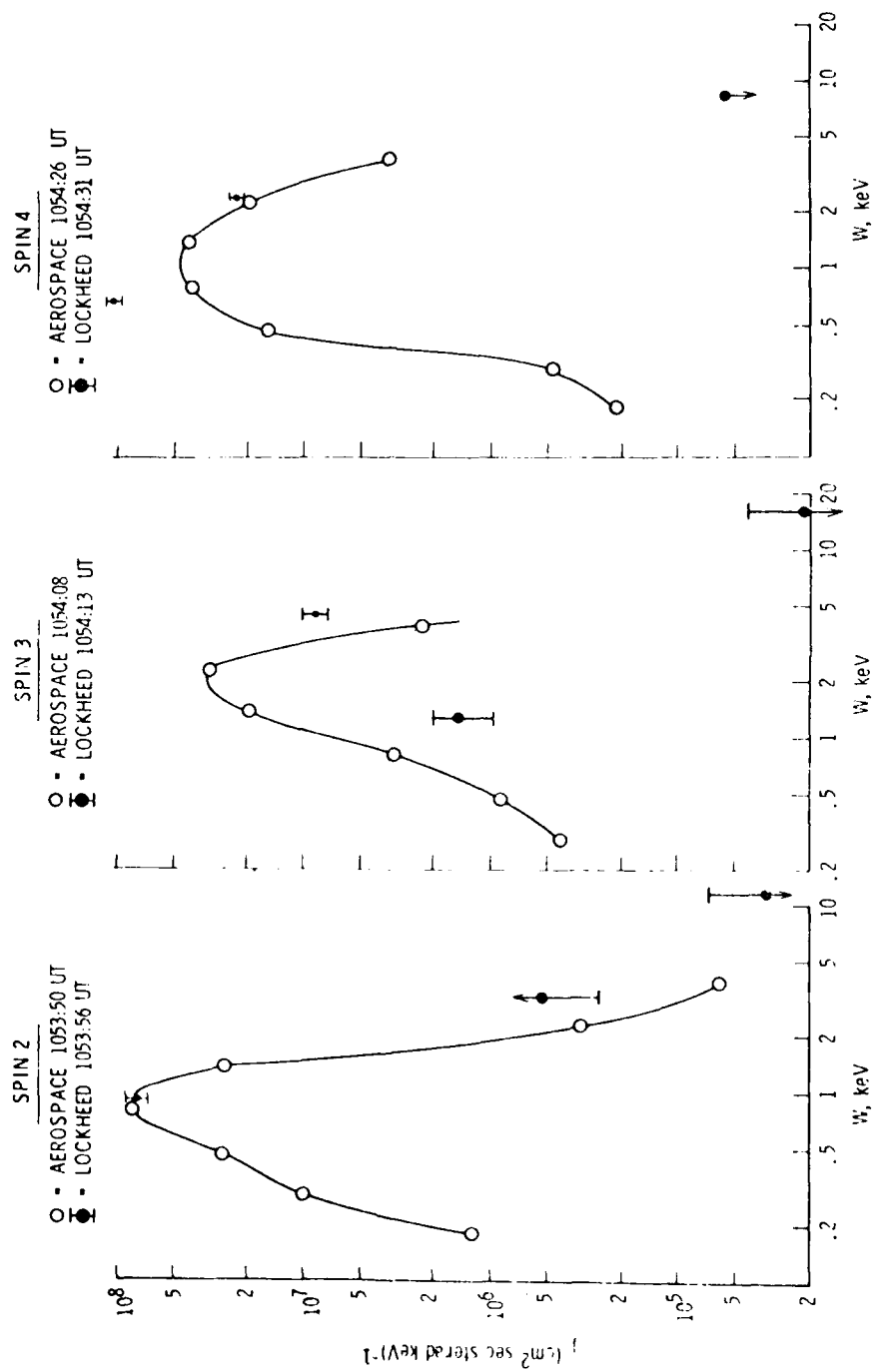


Figure 13. Energy spectra of ions measured by the Lockheed and Aerospace groups on the three consecutive spins of the S3-3 satellite through the inverted-V structure discussed in References 1 and 2.

spectra as constraints on the model parameters, the combinations of the parameters that resulted in spectra similar to spectra 1 and 2 are listed in Table 2.

Table 2. Parameters in model that give computed ion spectra similar to observed spectra 1 and 2.

Spectrum Number	H_{so} (km)	H_{scale} (km)	H_R (km)	$E_{ }$ (mV/m)	Γ (keV/sec)	Δt (sec)
1	4000	600	8000	0.2	.0306	.04083
2	4000	600	8000	0.5	.1061	.06455

The corresponding pitch-angle distributions were consistent with the measurements, but these measurements were not sufficiently precise to provide an adequate test of the computational results.

Some of the computed ion distributions are shown in Figures 14-29. All these distributions were computed using the following parameters: $H_{so} = 4000$ km, $\Delta H_s = 400$ km, $H_{scale} = 600$ km, $w_{||0} = .01$ keV, and $w_{\perp 0} = .3$ keV. The number of case histories from the base altitude, N_o , was 2000. The values of $E_{||}$, Γ , Δt , H_R , and $\Delta\phi = E_{||}(H_R = H_{so})$ are given in the figure captions. The histograms shown in Figures 14 and 15 are the energy spectrum of the flux (print-out item (ii) described above) and the corresponding pitch-angle distribution of the ions (print-out item (iv)) at $H_R = 6000$ km, for $E_{||} = .2$ mV/m, $\Delta\phi = .4$ keV, $\Gamma = .0433$ keV/sec, and $\Delta t = .02887$ sec. The ordinates are related to the counts in the cells as described in items (ii) and (iv) above. Note that both distributions are quite broad, owing to the high energy that the ions acquire from the transverse heating mechanism relative to the energy that the ions acquire by falling through the potential drop along the magnetic field. The output information described in item (iii) above reveals that the pitch-angle distributions of the ions are strongly energy dependent; toward increasing ion energies, the pitch-angle distributions become narrower and peaked at larger pitch angles. Hence, conical pitch angle distributions may be observed not only when the ions are rapidly accelerated within a short distance along the magnetic field by coherent EIC waves, but also when the ions are accelerated more slowly by the waves over a long distance if the energy threshold of the detector is sufficiently high; in this case, about 1.3 keV.

The distributions at the higher altitude, $H_R = 8000$ km computed with the parameters listed for spectrum number 1 in Table 2, are shown in Figure 16 and 17. The measured spectrum is also drawn in Figure 16. Note that the computed distribution is in fair agreement with the measured value. The number density of the ions in Spectrum 1 is about $0.2/\text{cm}^3$ (Ref. 1). Application of the continuity equation reveals that if all these ions originated 4000 km below the satellite with initial energies of .01 keV, the number density of the ions at the source would be about $5/\text{cm}^3$.

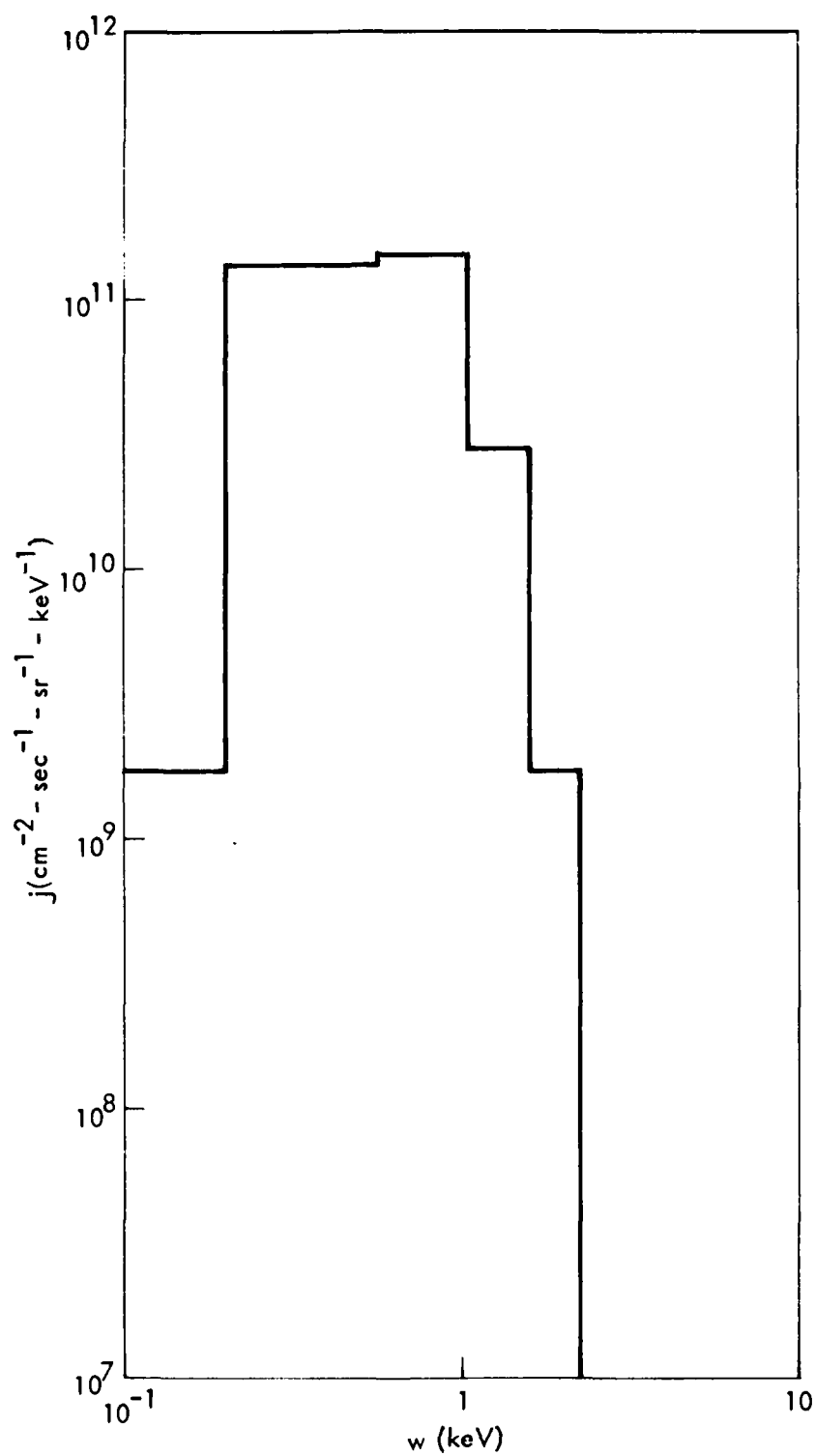


Figure 14. Histogram of directional flux versus energy
 $E_H = .2$ mV/m, $r = .02330$ keV/sec, $\Delta t = .02887$ sec,
 $H_R = 6000$ km, and $\Delta\phi = .4$ kV.

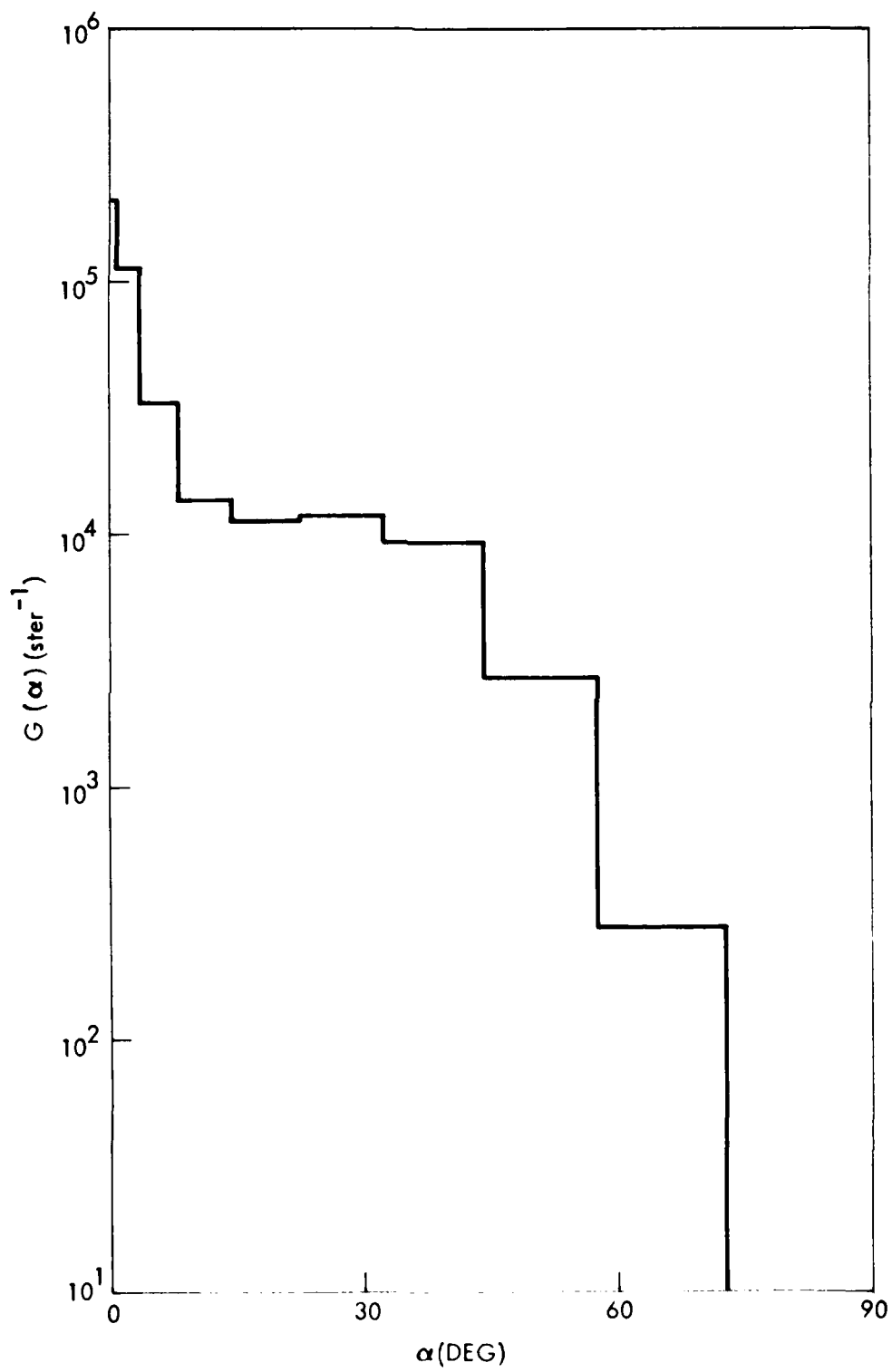


Figure 15. Histogram of pitch-angle distribution of ions for conditions listed in caption of Figure 14.

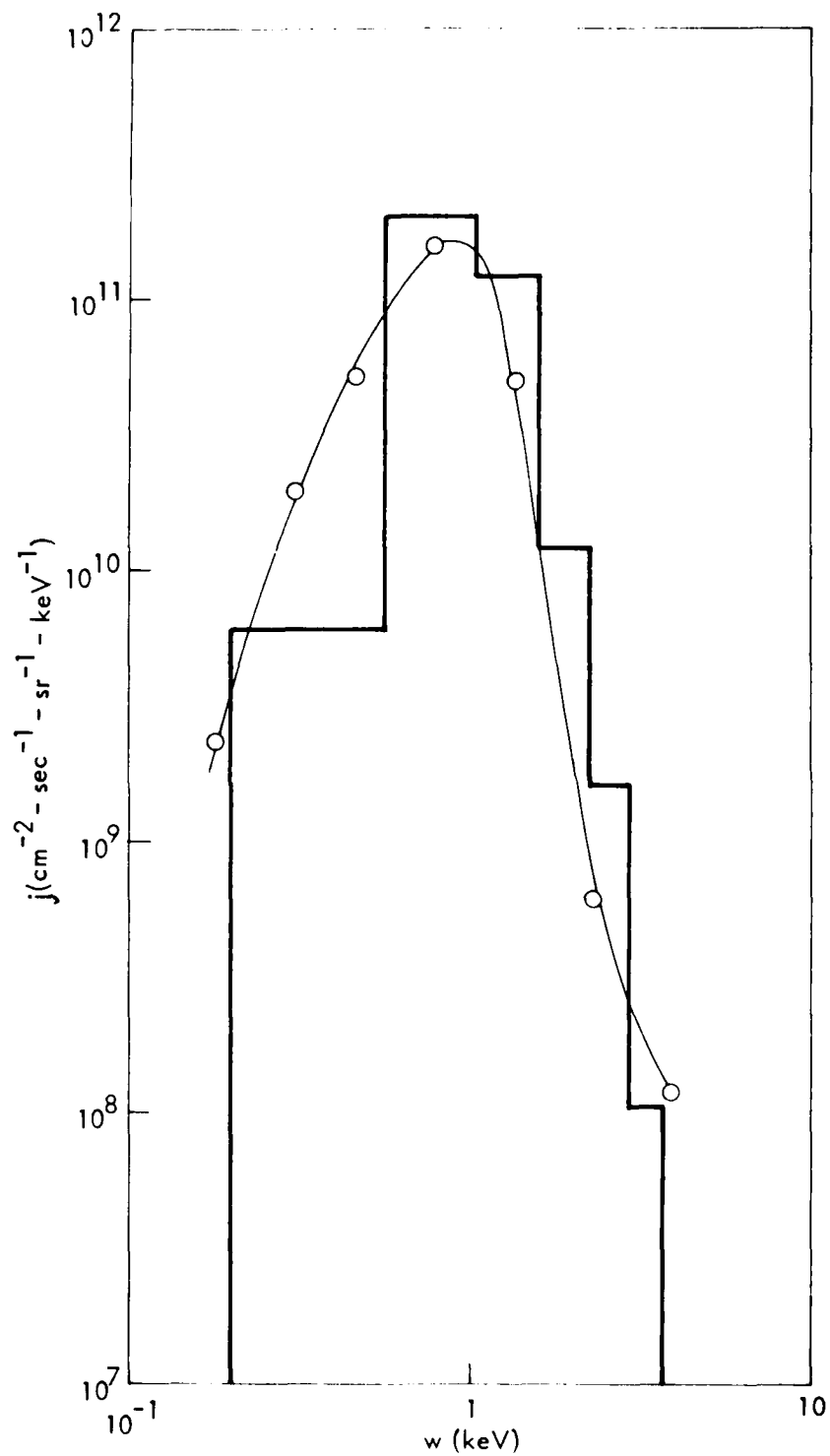


Figure 16. Histogram of directional flux versus energy. $E_H = .2$ mV/m, $\Gamma = .03061$ keV/sec, $\Delta t = .04083$ sec $H_R = 8000$ km, and $\Delta E = .8$ keV. The curve is the measured flux (spectrum number 1) fitted to the histogram.

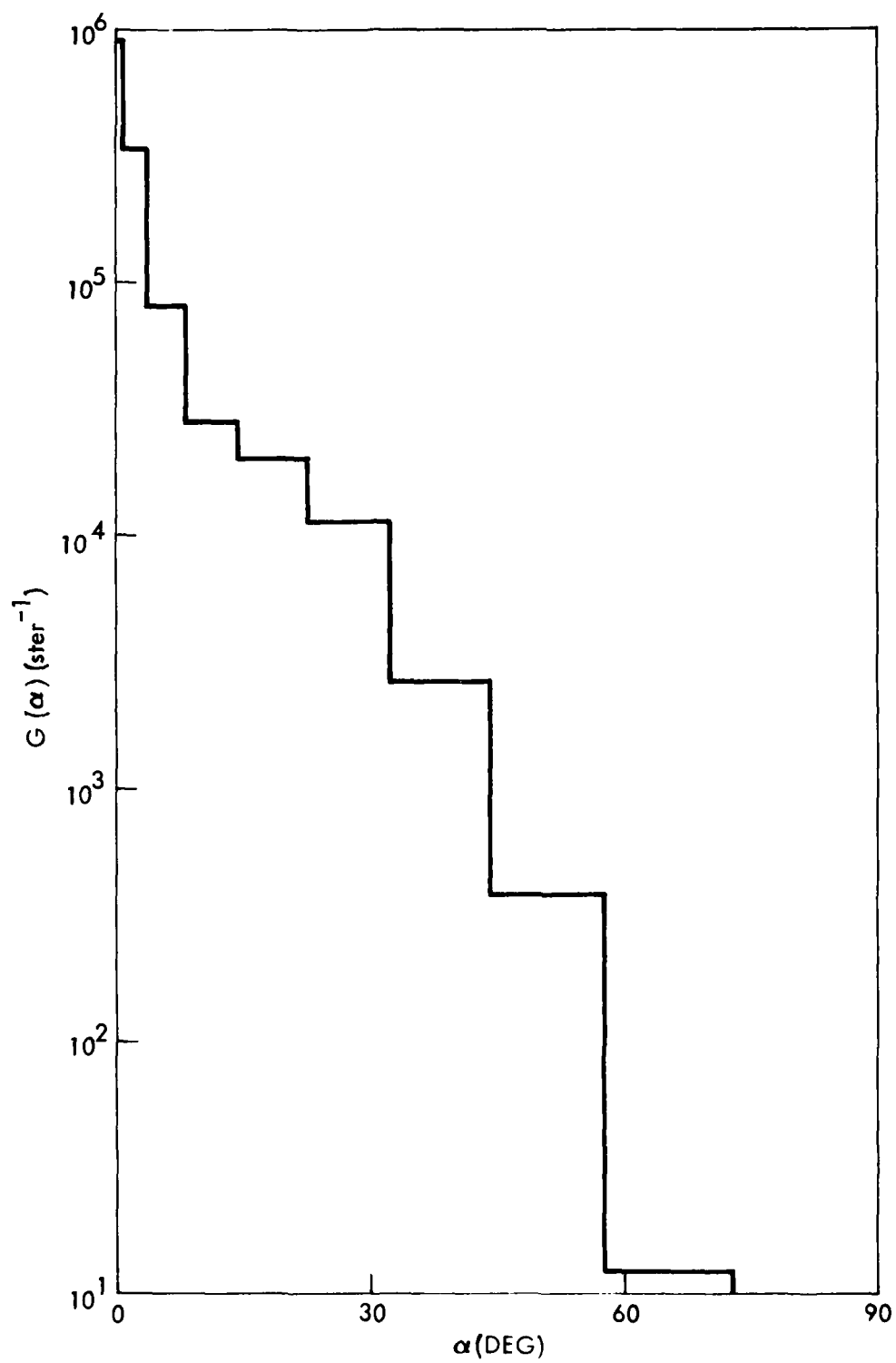


Figure 17. Histogram of pitch-angle distribution of ions for conditions listed in caption of Figure 16.

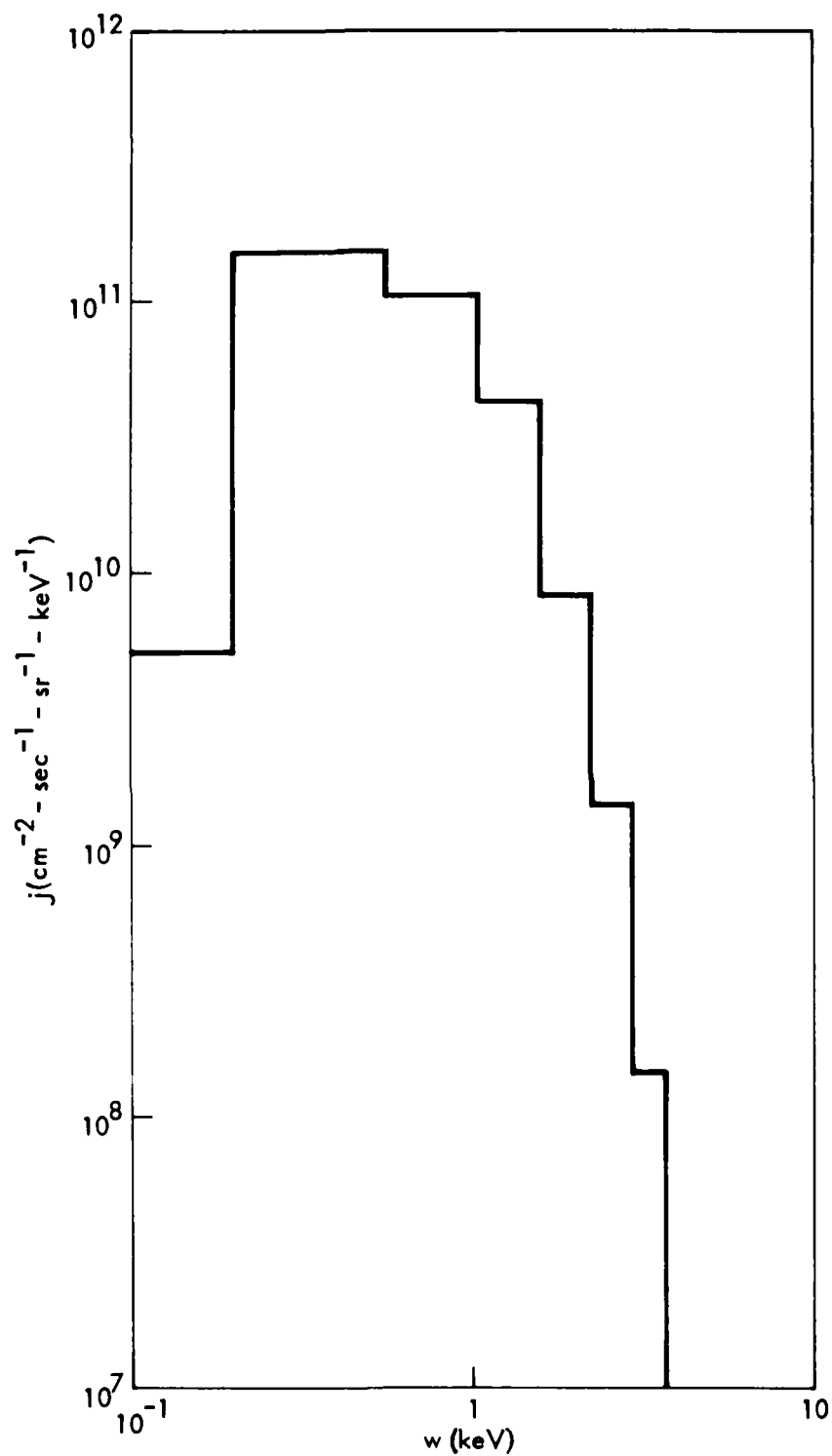


Figure 18. Histogram of directional flux versus energy.
 $E_{\parallel} = .2$ mV/m, $\Gamma = .08660$ keV/sec, $\Delta t = .02887$ sec,
 $H_R = 600.0$ km, and $\Delta\phi = .4$ kV.

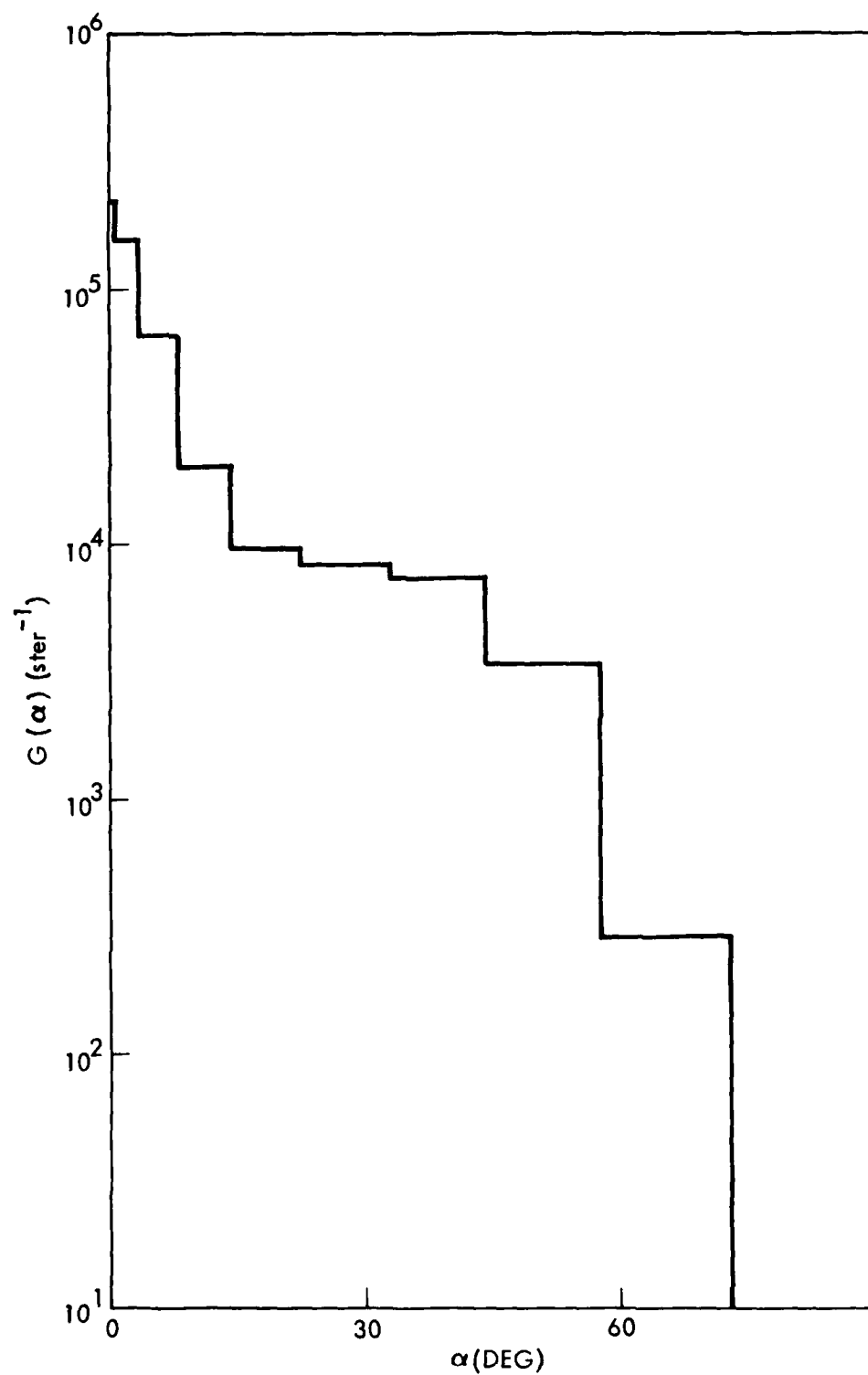


Figure 19. Histogram of pitch-angle distribution of ions for conditions listed in caption of Figure 18.

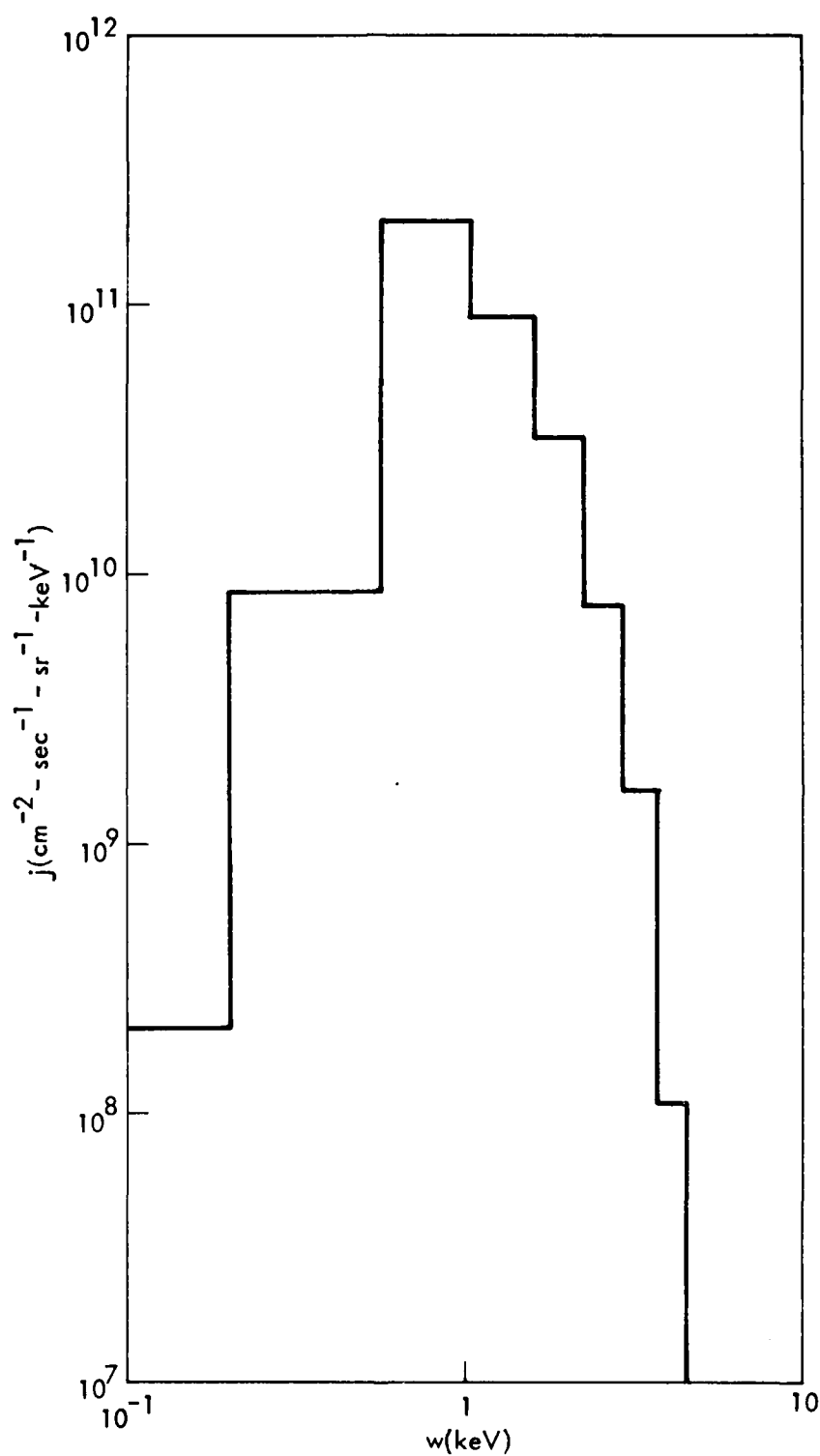


Figure 20. Histogram of directional flux versus energy.
 $E_H = .2$ mV/m, $\Gamma = .06122$ keV/sec, $\Delta t = .04083$ sec,
 $H_R = 8000$ km, and $\Delta\phi = .6$ kV.

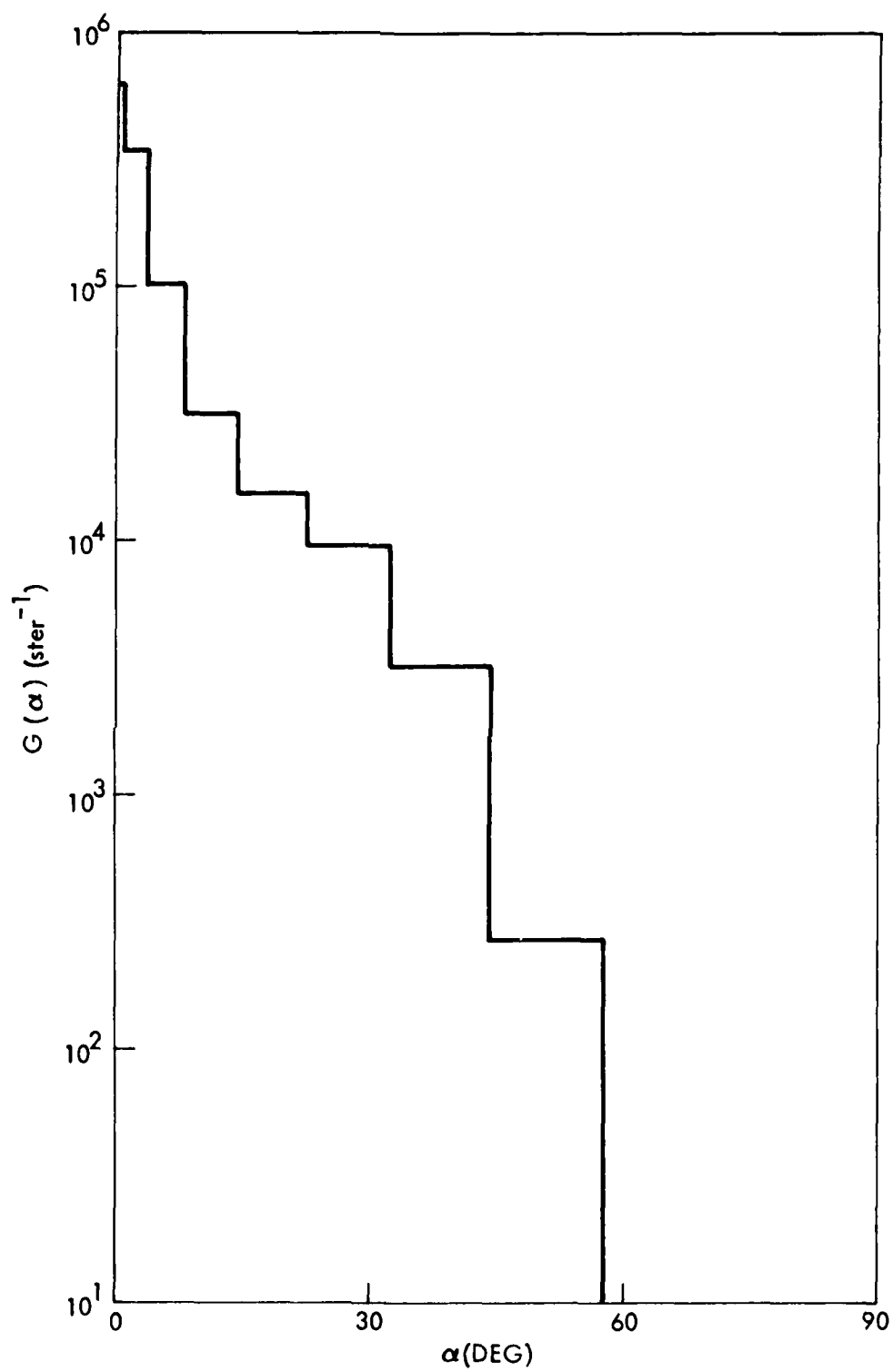


Figure 21. Histogram of pitch-angle distribution of ions for conditions listed in caption of Figure 20.

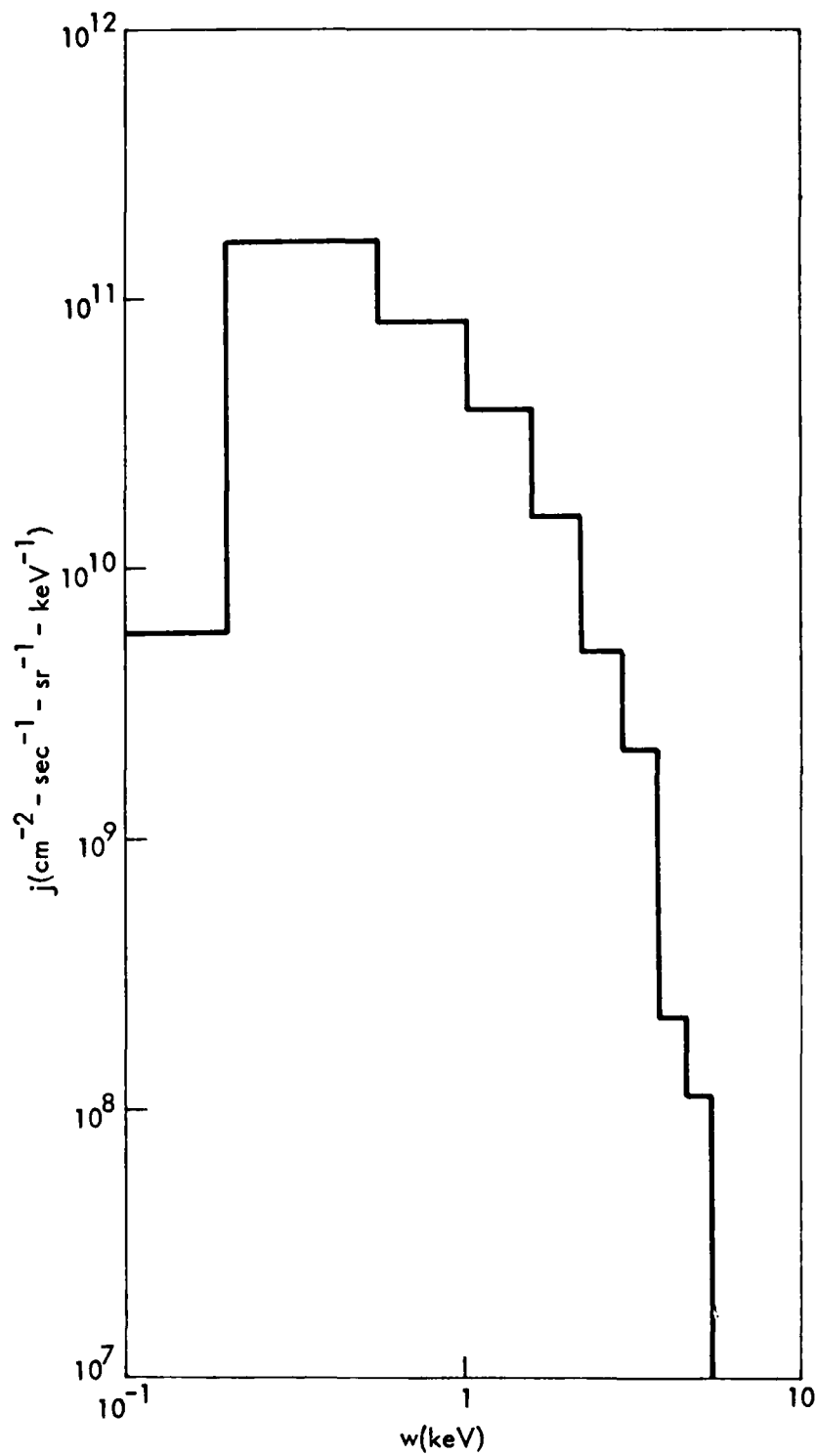


Figure 22. Histogram of directional flux versus energy.
 $E_H = .2 \text{ mV/m}$, $\Gamma = .1732 \text{ keV/sec}$, $\Delta t = .02887 \text{ sec}$,
 $H_R = 6000 \text{ km}$, and $\Delta\phi = .4 \text{ kV}$

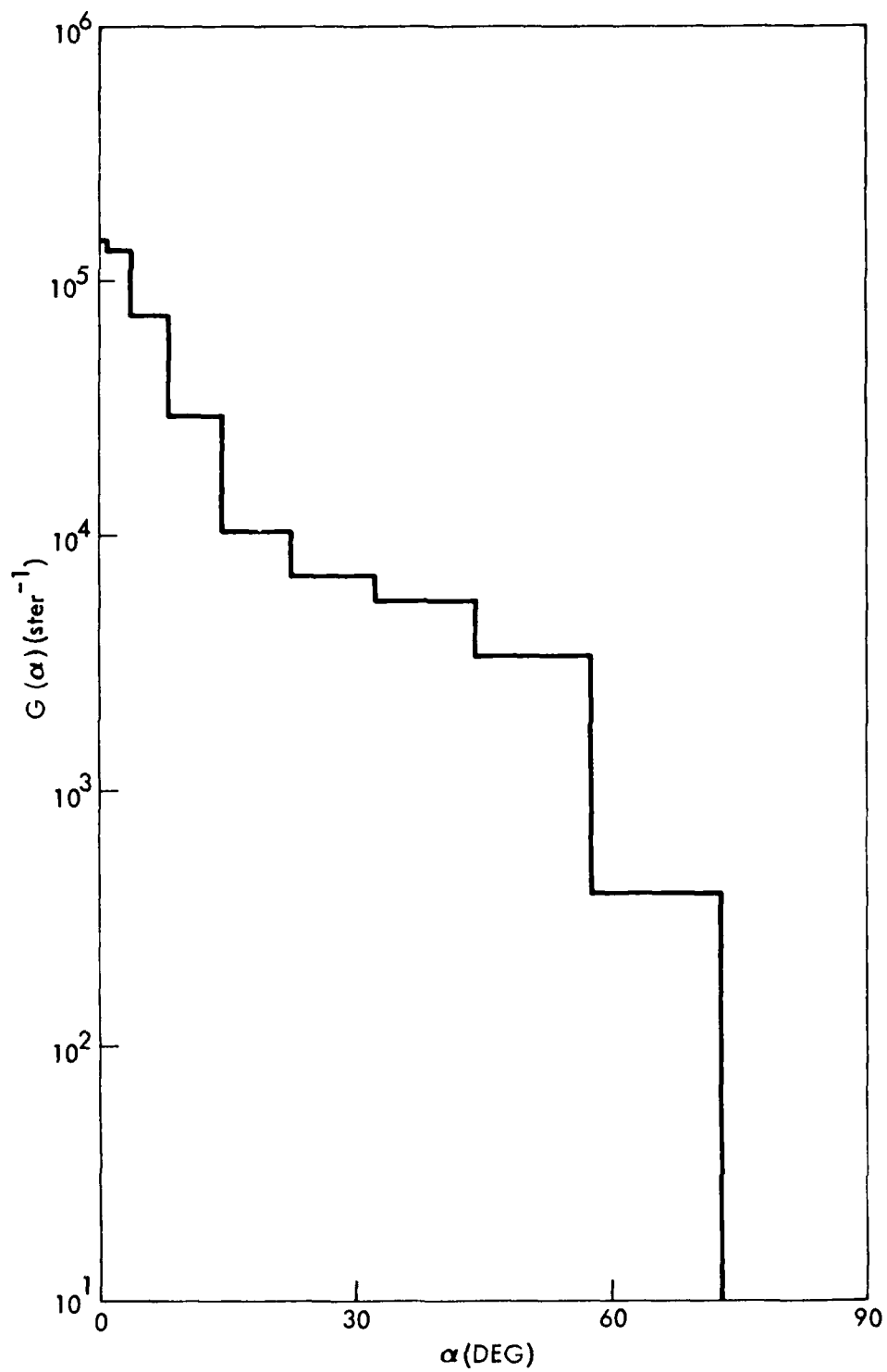


Figure 23. Histogram of pitch-angle distribution of ions for conditions listed in caption of Figure 22.

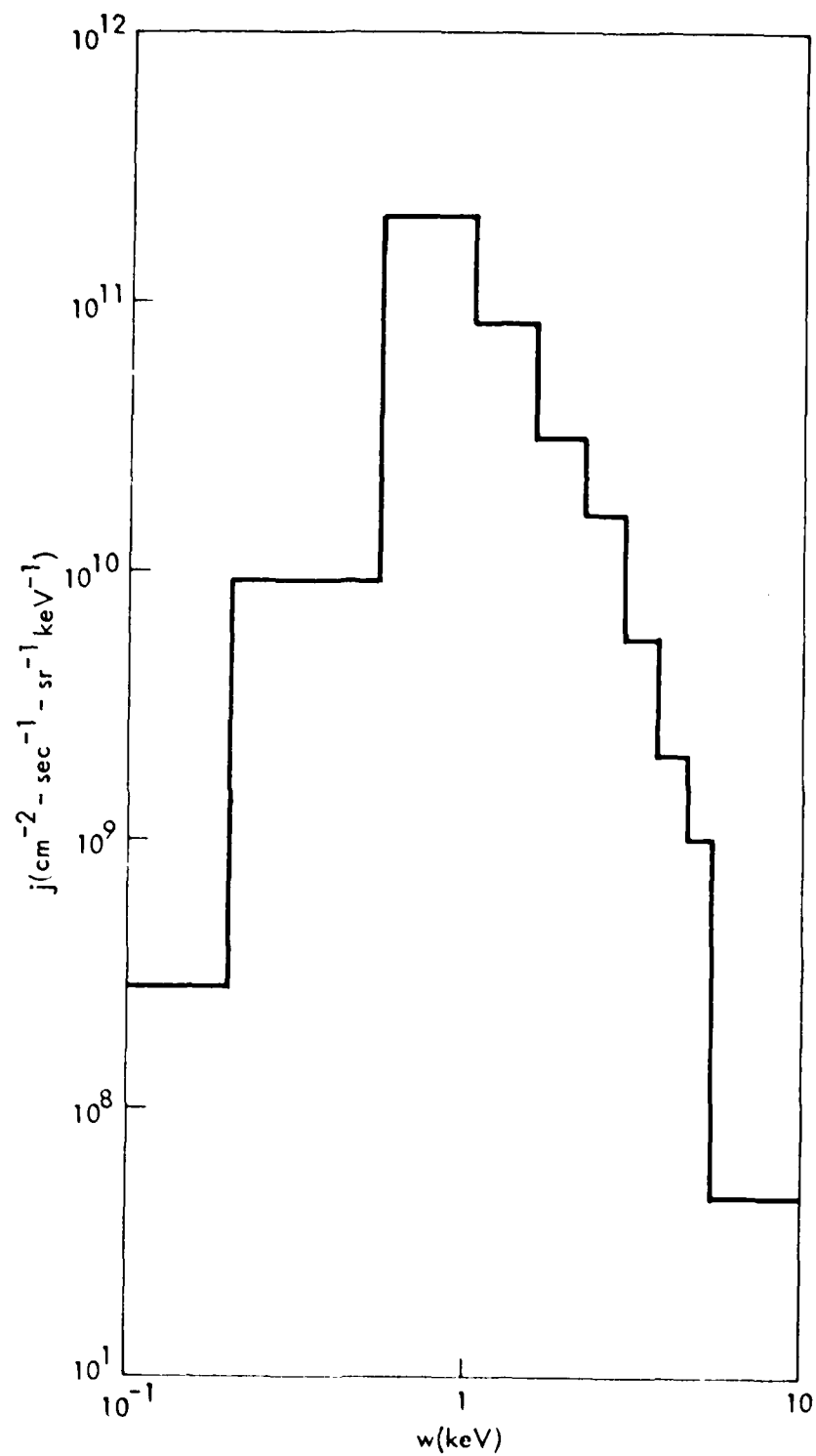


Figure 24. Histogram of directional flux versus energy.
 $E_H = .2$ mV/m, $\Gamma = .1225$ keV/sec, $\Delta t = .04083$ sec,
 $R_R = 3000$ km, and $\Delta\epsilon = .8$ keV.

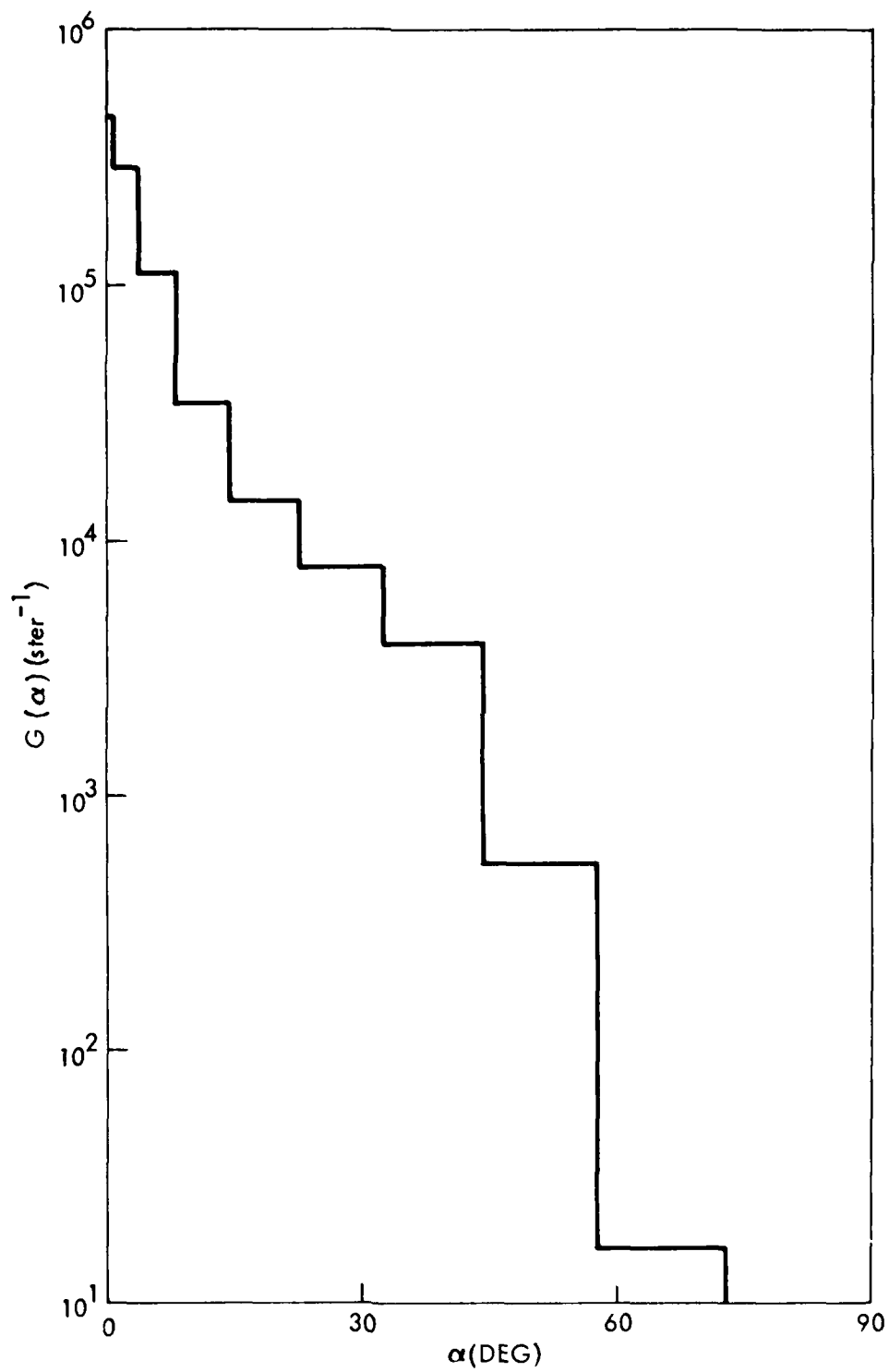


Figure 25. Histogram of pitch-angle distribution of ions for conditions listed in caption of Figure 24.

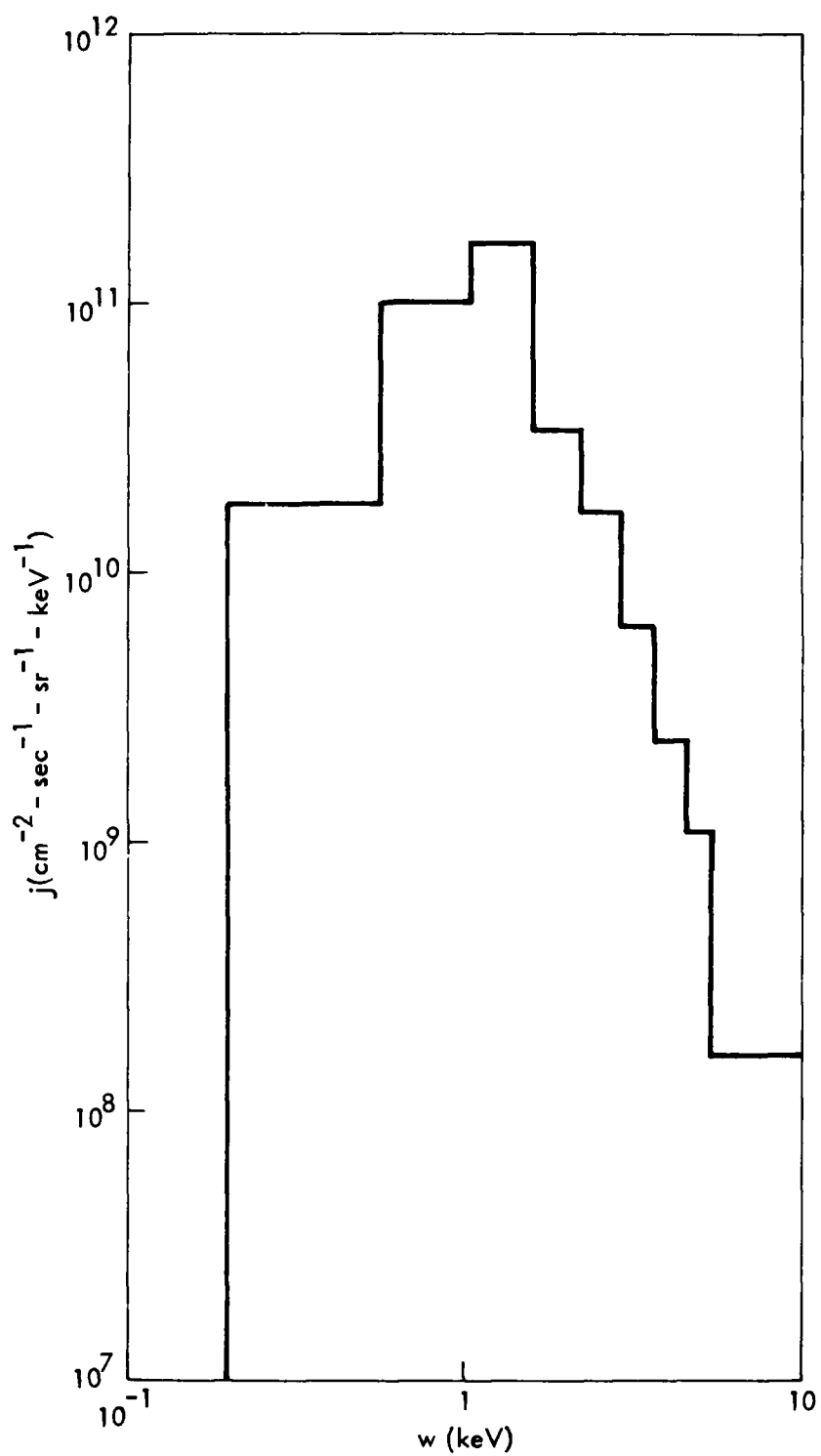


Figure 26. Histogram of directional flux versus energy.
 $E_{\parallel} = .5$ mV/m, $\Gamma = .1500$ keV/sec, $\Delta t = .04564$ sec,
 $H_R = 6000$ km, and $\Delta\phi = 1$ kV.

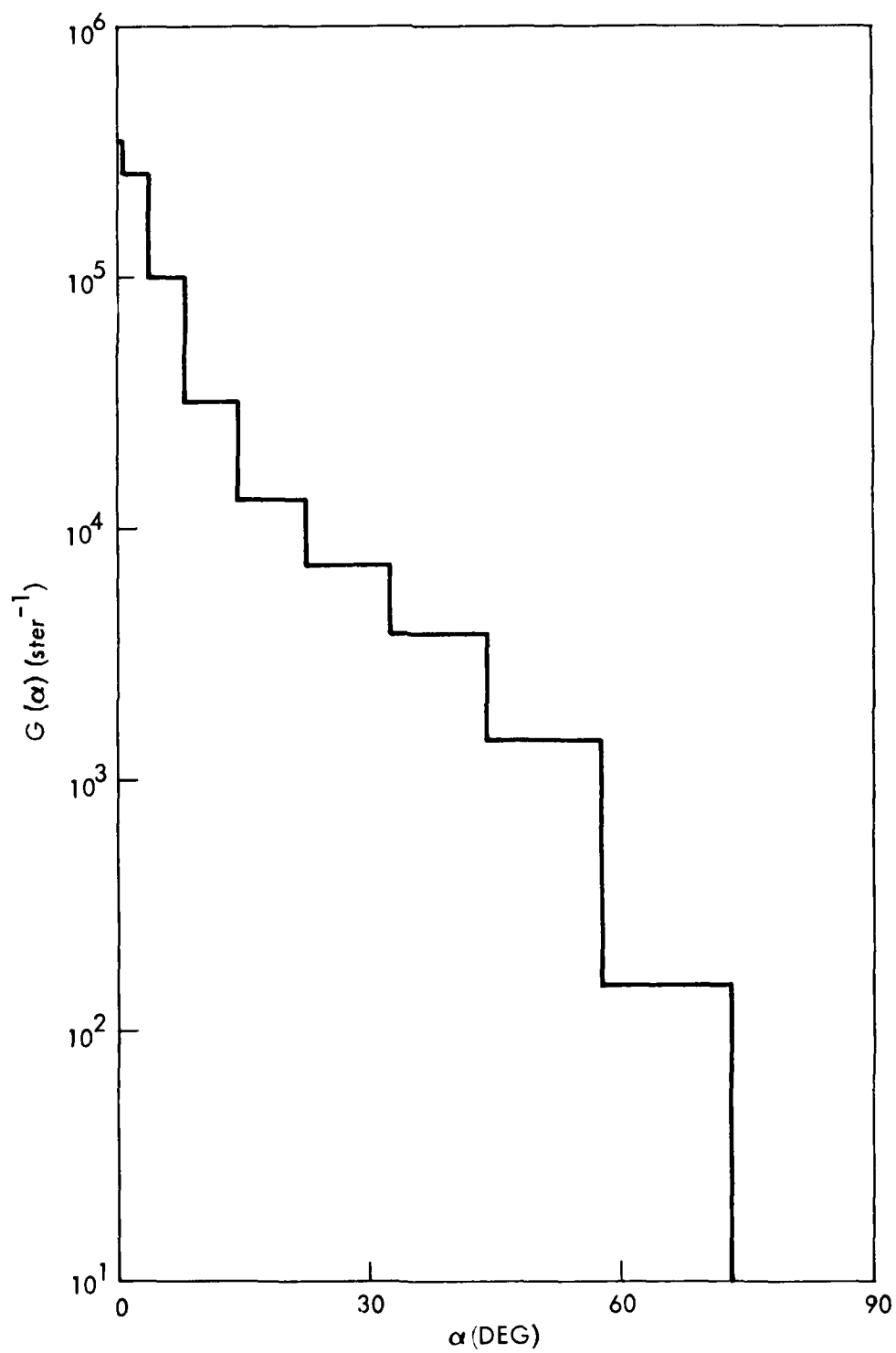


Figure 27. Histogram of pitch-angle distribution of ions for conditions listed in caption of Figure 26.

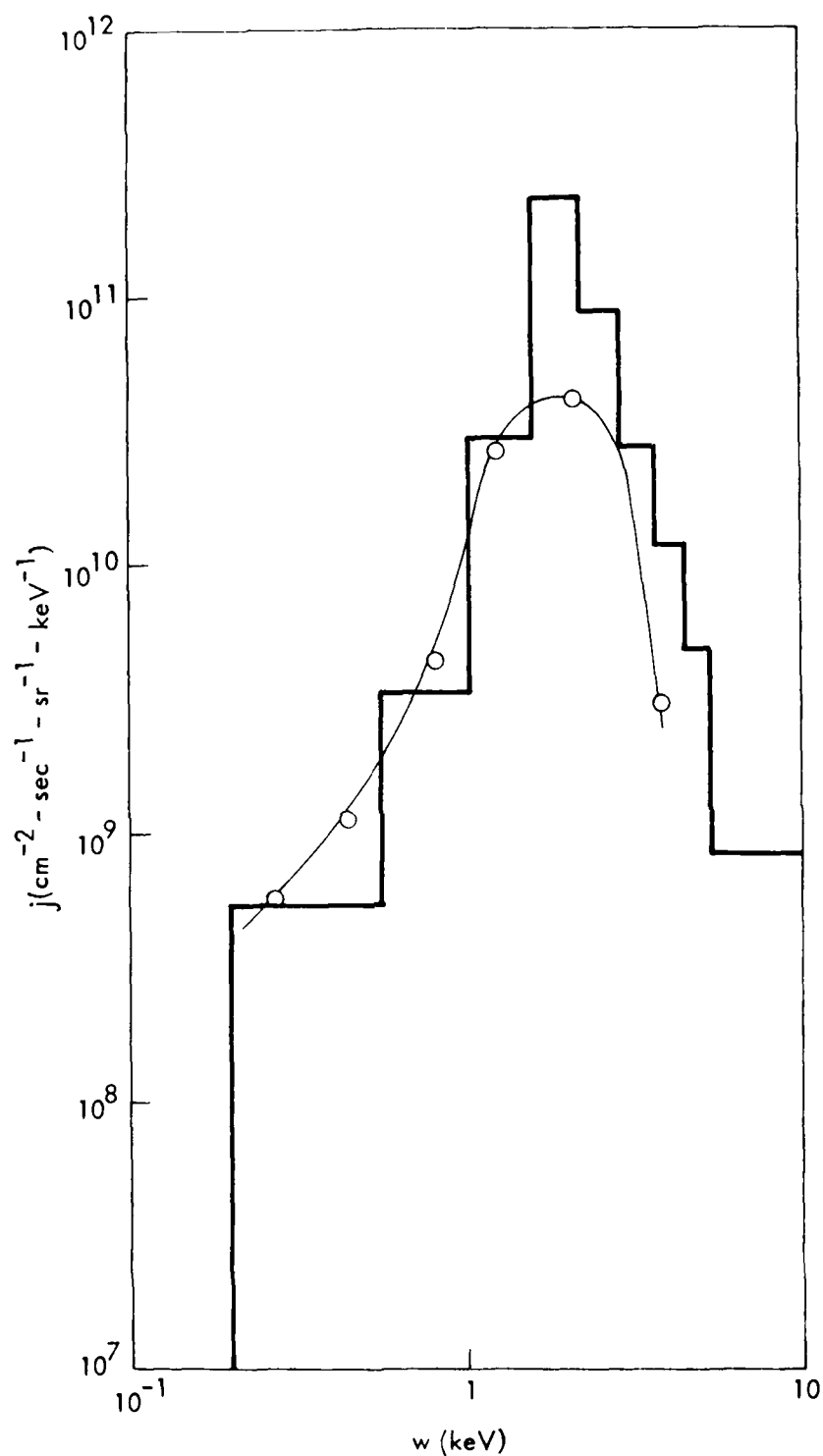


Figure 28. Histogram of directional flux versus energy. $E = .5$ nV/m, $\Gamma = .1061$ keV/sec, $\Delta t = .06455$ sec, $H_R = 3000$ km, and $\Delta\phi = 2$ kV. The curve is the measured flux (spectrum number 2) fitted to the histogram.

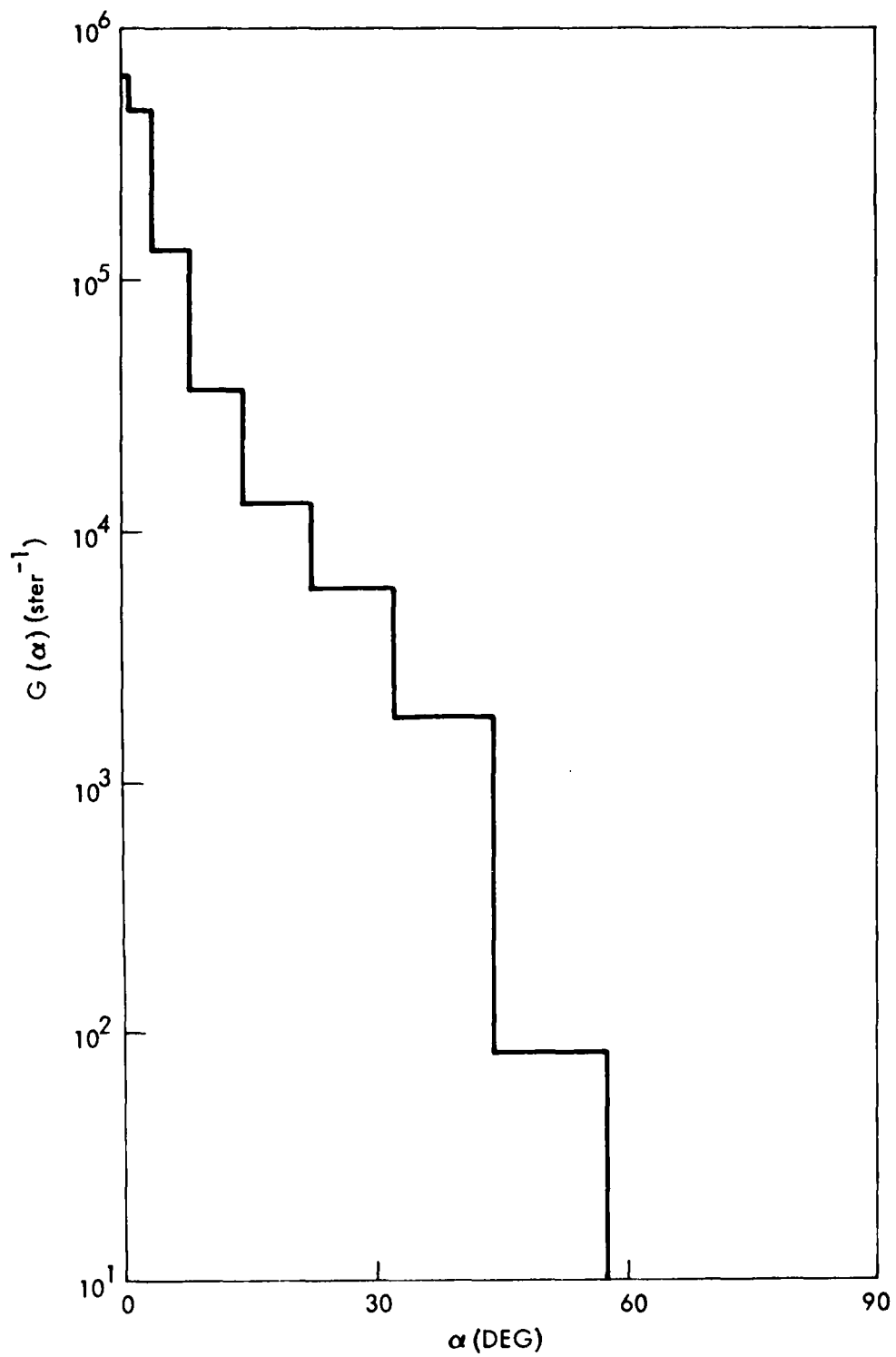


Figure 29. Histogram of pitch-angle distribution of ions for conditions listed in caption of Figure 28.

A comparison of the distributions in Figures 14 and 16 indicate that Spectrum 1 could also have been matched if the base of the source had been chosen to be 2000 km (i.e., $H_R - H_{SO}$) below the satellite and E had been increased to 0.4 mV/m.

The succeeding figures, 18-25, principally illustrate the effect of an increasing heating rate on the distributions at the two altitudes, 6000 km and 8000, above the source base, 4000 km. The effect of an increased electric field is illustrated in Figures 26-29. Spectrum 2 is compared with the ion distribution in Figure 28. Here, again, the agreement is seen to be fairly good. It could have been improved by decreasing $E_{||}$ somewhat and increasing Γ . Spectrum 2 could also have been fit by choosing parameters similar to those listed in the caption of Figure 26 (a source base 2000 km below the satellite) but doubling the electric field, to 1 mV/m.

The distribution in Figure 26 matches very well the measured spectrum, 3. However, in the computation of that distribution, $\Delta\phi$ was 0.8 kV. The potential difference below the satellite at the time of the Spectrum 3 measurement was about 2.5 kV. In the context of the model discussed above, a peak in the spectrum below the energy $e\Delta\phi$ can only be explained if the source intensity increases at altitudes above the potential ϕ_m . The potential difference above the satellite was very small when spectra 1 and 2 were measured; it then increased sharply on the following satellite spin, when spectrum 3 was measured, implying an intensification of the wave field above the satellite. If the wave field also increased below the satellite, but above the point where $\phi = \phi_m$, an increase in the ion source intensity above the base could be explained.

SECTION V

CONCLUSIONS

The data obtained on 17 January 1977, while the S3-3 satellite was along a long trajectory, from 21.3h MLT to 16.0h MLT, through the nominal region of the upward magnetic-field-aligned current sheet, yielded important new information on the properties of the potential structure. The results described in Section III.3 indicate that high potential differences, to values exceeding 10 kV, along the magnetic field were present over the entire local-time interval of the satellite pass through the region. The results also indicate that energetic H^+ and O^+ ions with pitch-angle distributions generally peaked along the magnetic field, but sometimes peaked at angles inclined to the field (conics), were present whenever the potential differences occurred.

Ghielmetti et al. (Ref. 4), by examining the data on the upward-flowing ions obtained with the S3-3 satellite on traversals of the current-sheet region at different local times but within short local-time intervals, found that the probability of observing upward-flowing ions over the auroral oval is high (>60% above an altitude of 4000 km). The probability of such observations is the highest during the local evening. At other local times, the probability is highly correlated with magnetic activity.

The results of this statistical study, therefore, together with the observations in the current sheet region over the wide local-time interval, indicate that the current sheet on the dusk half of the auroral oval is nearly always unstable over a wide range of longitude. This finding is consistent with the model of the antisolar convection of the polar-cap field lines over the polar cap discussed in Section II and with the instability criteria provided by Kindel and Kennel (Ref. 14). Potential difference along the magnetic field evidently appear on the dawn side of the auroral oval at high values of K_p when the region 2 current system develops.

The latitudinal fluctuations of the potential region inferred from the data (see, e.g. Figure 10) are not surprising in view of the behavior of the discrete aurorae and the expected resonant oscillations of high-latitude field lines. An important consequence of this finding, however, is that latitudinal motions of the current sheet induce electric fields along the magnetic field. The nature and effects of such electromagnetic fields have not yet been assessed.

Another fascinating feature of the data are the spikes—the high fluxes of electrons that are highly collimated in both directions along the magnetic field. The source of these spikes has not yet been investigated.

The analysis of the ion distributions indicate that the ions are simultaneously heated transversely by interacting with the EIC wave turbulence and

accelerated longitudinally by the electric field along the magnetic field. The simulation of this acceleration process in a Monte Carlo program, using a transverse heating rate appropriate for typical values of wave power spectra and potential differences below the satellite, was successful in reproducing the usual characteristics of the ions in the potential region. The results indicate that energy spectra with peaks at energies equal to or less than the potential energy below the satellite can be reconstructed by assuming the ion source to be extended along the magnetic field, with its base located at several thousand kilometers below the satellite and its intensity diminishing exponentially toward higher altitudes with a scale height less than about 1000 km. If the peaks of the energy spectra are at energies less than the potential energy below the satellite, the source intensity must increase with altitude. In all the simulation runs, the electric field was taken to be equal to the potential difference below the satellite divided by the distance between the source base and the satellite.

The pitch-angle distributions of the ions resulting from this acceleration process are both peaked at $\alpha = 180^\circ$ and conically-shaped, depending on the energy band of the ions. At low energies, the distributions are peaked along the field; toward increasing ion energies, the distributions become peaked at increasing inclination angles.

The distribution of the source intensity used in the simulation program may reflect solely the intensity of the wave field, since a source number density less than about 5 ions/cm^3 is needed to account for the observed ion fluxes. Hence, the distribution of the wave turbulence, as well as the scale of the potential distribution, are found to be consistent with the anomalous-resistivity theory.

SECTION VI

RECOMMENDATIONS

The close relationship between the phenomena occurring in the polar-cap regions and in magnetic tubes containing hot plasma resulting from a nuclear explosion has been established. The instability criteria predicted by Kindel and Kennell (Ref. 14), and verified in the auroral current sheet, indicate that the currents at the boundaries of tubes containing hot plasma due to megaton-type explosions will become unstable and thereby impair the coupling of the ionosphere and magnetosphere. In order to predict the ensuing effects, more detailed information on the natural phenomenon should be obtained.

Several recommendations stem from this work. Recently, the S3-3 satellite has made several passes through the region of the current sheet, in the southern hemisphere, similar to the one on 17 January 1977. Since the analysis of the 17 January data has yielded so much information on the properties and dynamics of that region, analysis of further data of this type is recommended. Attempts should be made to correlate such observations with simultaneous measurements in or near the current sheet of the wave turbulence and ion measurements on the GEOS and ISEE satellites.

The high fluxes of counterstreaming electrons (the electron spikes) continue to pose a perplexing and fascinating problem. Further data on this phenomenon should be analyzed, and an intensive theoretical investigation should be undertaken. Such a study may very likely uncover a dynamical plasma process which may have an important impact on some of the defense problems discussed in Section I.

The electric field induced by the motion of the current sheet above the auroral oval, as well as the effects of this electric field, should also be investigated.

Information on the location and extent of the region where the ions are accelerated perpendicularly to the field can be inferred fairly directly from the energy and conical pitch-angle distributions of the ions. Wide pitch-angle distributions at high ion energies indicate a large extent of the heating region. The Monte Carlo program could be used for the analysis of such cases. Maxwellian energy distributions and narrow pitch-angle distributions with peaks at angles that increase with increasing energy indicate a short extent of the heating region. Such cases could be investigated analytically through an application of Liouville's theorem. Figure 30 depicts the form of the flux, as a function of pitch angle, expected for ions that have been heated transversely to a temperature $T_t = 0.8$ keV below the satellite, where the magnetic field intensity was 5 times the field intensity at the satellite and where the potential was 1 kV higher. The arrows denote the pitch-angles of the ions which have the energies shown at the arrows. The ion temperature and number

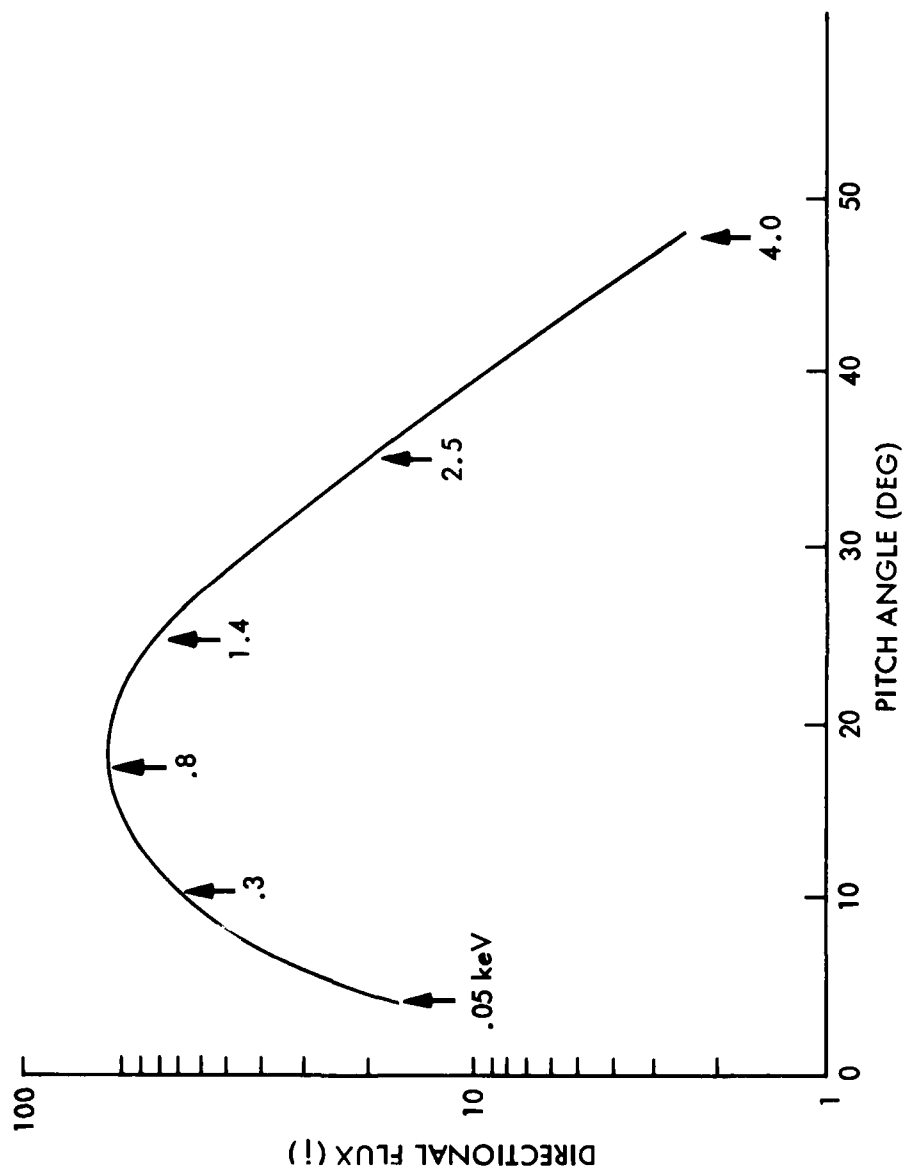


Figure 30. Directional flux at B_s , ϕ_s versus pitch angle for ions that have been transversely heated at $B = 5B_s$, $\phi - \phi_s = 1$ kV to a temperature of 0.8 keV. The points noted on the curve are the pitch angles of the ions which have the energies shown at the arrows.

density, and the location and potential of the source point, can be inferred from such distributions. Finally, narrow energy distributions, in addition to narrow pitch-angle distributions, imply acceleration by coherent EIC waves. Such distributions can also be analyzed by using Liouville's theorem. These analyses require highly resolved measurements of both the energy and pitch-angle distributions of the ions, in addition to the electron measurements which are required for the determination of the potential difference. Appropriate measurements are available from the combined experiments of Lockheed and Aerospace on the S3-3 satellite.

In addition to the investigations of the natural phenomena recommended above, the possible effects of anomalous resistivity in magnetic tubes containing hot plasma produced by nuclear bursts should be estimated. For these investigations, the potential difference along the magnetic field should be assumed to be a sizable fraction of the potential difference across the tube, say 1/4th, as in the case of the polar-cap region.

The effects of an electric field along the magnetic field and transverse EIC-wave heating on the distributions of the debris in the magnetosphere should also be estimated. If, owing to the transverse heating, an appreciable fraction of the debris will become trapped by the magnetic field, the intensity of the trapped electrons will be appreciably enhanced. Moreover, the build-up of trapped debris in the radiation belt in the event of a nuclear exchange would present a further hazard to satellite systems.

SECTION VII

REFERENCES

The following references contain further guidance:

1. Cladis, J.B., G.T. Davidson, W.E. Francis, L.L. Newkirk, and M. Walt, "Assessment of processes related to plasma irregularities," Final Report, DNA 4473F, Defense Nuclear Agency, Washington, D.C. 20305, 1978.
2. Cladis, J.B., and R.D. Sharp, "Scale of electric field along magnetic field in an inverted-V event," J. Geophys. Res., 84, 6564, 1979.
3. Mizera, P.R., and J.F. Fennell, "Signatures of electric fields from high and low altitude particles distributions," Geophys. Res. Lett. 4, 311, 1977.
4. Ghielmetti, A.G., R.G. Johnson, R.D. Sharp, and E.G. Shelley, "The latitudinal, diurnal, and altitudinal distributions of upward flowing energetic ions of ionospheric origin," Geophys. Res. Lett., 5, 59, 1978.
5. Iijima, T., and T.A. Potemra, "The amplitude distribution of field-aligned currents at northern high latitudes observed by triad," J. Geophys. Res., 81, 2165, 1976.
6. Shelley, E.G., R.D. Sharp, and R.G. Johnson, "Satellite observations of an ionospheric acceleration mechanism," Geophys. Res. Lett., 3, 654, 1976.
7. Sharp, R.D., R.G. Johnson, and E.G. Shelley, "Energetic particle measurements from within ionospheric structures responsible for auroral acceleration processes," submitted to J. Geophys. Res., 1978.
8. Mozer, F.S., C.W. Carlson, M.K. Hudson, R.B. Torbert, B. Parady, J. Yatteau, and M.C. Kelley, "Observations of paired electrostatic shocks in the polar magnetosphere," Phys. Rev. Lett., 38, 292, 1977.
9. Gurnett, D.A. and L.A. Frank, "A region of intense plasma wave turbulence on auroral field lines," J. Geophys. Res., 82, 1031, 1977.
10. Sharp, R.D., R.G. Johnson, and E.G. Shelley, "Observation of an ionospheric acceleration mechanism producing (keV) ions primarily normal to the geomagnetic field direction," J. Geophys. Res., 82, 3324, 1977.
11. Block, L.P., "Double layers," in Physics of the Hot Plasma in the Magnetosphere, B. Hultqvist and L. Stenflo, ed., p. 229, Plenum Press, New York 1975.
12. Block, L.P., and C.-G. Fälthammar, "Mechanisms that may support magnetic-field-aligned electric fields in the magnetosphere," Ann. Geophys., 32, 161, 1976.

13. Swift, D. W., "On the formation of auroral arcs and acceleration of auroral electrons," J. Geophys. Res., 80, 2096, 1975.
14. Kindel, J. M., and C. F. Kennel, "Topside current instabilities," J. Geophys. Res., 76, 3055, 1971.
15. Papadopoulos, K., "A review of anomalous resistivity for the ionosphere," Rev. Geophys. Space Phys., 15, 113, 1977.
16. Fälthammar, C.-G., "Problems related to macroscopic electric fields in the magnetosphere," (Paper 7R0704), Rev. Geophys. Space Phys., 15, 457, 1977.
17. Cladis, J. B., G. T. Davidson, W. E. Francis, L. L. Newkirk, and M. Walt, "Improvement of SPECTER II code: injection and evolution of an artificial radiation belt," LMSC/D34017, Final Report, November 15, 1978
18. Sharp, R. D., E. G. Shelley, R. G. Johnson, and A. G. Ghielmetti, "Counter streaming electron beams at altitudes of $\sim 1 R_E$ over the auroral zone," Submitted to J. Geophys. Res., 1979.
19. McIlwain, C., "Auroral electron beams near the magnetic equator," in Physics of Hot Plasmas in the Magnetosphere, ed. by B. Hultquist and L. Stenflo, Plenum Pub. Co., N. Y., 1976.
20. Cain, J. C., Hendricks, S. J., Langel, R. A., and W. V. Hudson, "A proposed model for the international geomagnetic reference field-1965," J. Geomag. and Geoelectr., 19, 335, 1967.
21. Kennel, C. F., and H. E. Petschek, "Limit on stably trapped particle fluxes," J. Geophys. Res., 71, 1, 1966.
22. Davidson, G., and M. Walt, "Loss cone distributions of radiation belt electrons," J. Geophys. Res., 82, 1, 1977.
23. Chandrasekhar, S., "Stochastic problems in physics and astronomy," Rev. Mod. Phys., 15, 1, 1943.
24. Sturrock, P. A., "Stochastic acceleration," Phys. Rev. 141, 186, 1966.

DISTRIBUTION LIST

DEPARTMENT OF DEFENSE

Assistant to the Secretary of Defense
Atomic Energy

ATTN: Executive Assistant

Command & Control Technical Center

ATTN: C-650, W. Heidig

Defense Advanced Rsch. Proj. Agency

ATTN: TIO

Defense Communications Agency

ATTN: Code 810, J. Barna

Defense Communications Engineer Center

ATTN: Code 700, J. Lebo

ATTN: Code R103, D. Worthington

ATTN: Code R720, J. Worthington

ATTN: Code R103, J. Raffensberger

Defense Intelligence Agency

ATTN: DB-4D

ATTN: DT-1C

Defense Nuclear Agency

ATTN: RAEV

2 cy ATTN: RAAE

4 cy ATTN: TITL

Defense Technical Information Center

12 cy ATTN: DD

Field Command

Defense Nuclear Agency

ATTN: FCPR

Field Command

Defense Nuclear Agency

Livermore Division

ATTN: FCPR

Interservice Nuclear Weapons School

ATTN: TTV

Joint Chiefs of Staff

ATTN: J-3, Environmental Services Div.

ATTN: J-5, Nuclear Division

ATTN: C3S Evaluation Office

Joint Strat. Tgt. Planning Staff

ATTN: Document Control

National Security Agency

ATTN: TDL

Undersecretary of Defense for Rsch. & Engrg

ATTN: Strategic & Space Systems (OS)

DEPARTMENT OF THE ARMY

Atmospheric Sciences Laboratory

U.S. Army Electronics R&D Command

ATTN: DELAS-EQ-MO, R. Olsen

ATTN: DELAS-EQ-ME, K. Ballard

ATTN: DELAS-AS-M, R. Rubio

ATTN: DELAS-EQ, F. Niles

ATTN: DELAS-BE-A, J. Butterfield

DEPARTMENT OF THE ARMY (Continued)

BMD Advanced Technology Center

Department of the Army

ATTN: ATC-O, W. Davies

ATTN: ATC-T, M. Capps

BMD Systems Command, Department of the Army

ATTN: BMDSC-H, N. Hurst

Chief of Engineers

Department of the Army

ATTN: DAEN-RDM, F. De Percin

Deputy Chief of Staff for Rsch., Dev., & Acq.

Department of the Army

ATTN: DAMA-WSZ-C

ATTN: DAMA-CSZ-C

Electronics Tech. & Devices Lab.

U.S. Army Electronics R&D Command

ATTN: DELET-ER, H. Bomke

ATTN: DRSEL-RD-P

ATTN: DELEW-D

ATTN: DELET-R, S. Kronenberg

Harry Diamond Laboratories

Department of the Army

ATTN: DELHD-N-P, F. Wimenitz

U.S. Army Ballistic Research Labs

ATTN: DRDAR-TSB-S

ATTN: DRDAR-BLB, J. Mester

ATTN: DRDAR-BLP, J. Heimerl

U.S. Army Missile Command

ATTN: DRDMI-XS

ATTN: DRSMI-ABL

U.S. Army Nuclear & Chemical Agency

ATTN: Library

U.S. Army Research Office

ATTN: R. Mace

ATTN: DRXRO-JC, H. Robl

U.S. Army Satellite Comm. Agency

ATTN: Technical Library

U.S. Army Materiel, Dev., & Readiness Command

ATTN: DRXCD-TL

ATTN: DRCLDC, J. Bender

White Sands Missile Range

Department of the Army

ATTN: AMSEL-NL-SD, W. Webb

ATTN: STEWS-TE-AN, M. Squires

DEPARTMENT OF THE NAVY

Naval Electronic Systems Command

ATTN: PME 117-20

ATTN: Code 501A

ATTN: ELEX 03

Naval Intelligence Support Center

ATTN: Document Control

ATTN: Code 40A, E. Blase

DEPARTMENT OF THE NAVY (Continued)

Naval Ocean Systems Center
ATTN: Code 532, J. Richter
ATTN: Code 532, R. Pappert
ATTN: Code 5321, I. Rothmuller
ATTN: Code 5324, W. Moler

Naval Postgraduate School
ATTN: Code 61 DY, J. Dyer
ATTN: Code 0142 Library
ATTN: Code 61 MN, E. Milne

Naval Research Laboratory
ATTN: Code 6750, D. Strobel
ATTN: Code 7175, J. Johnson
ATTN: Code 6623, R. Statler
ATTN: Code 7128, J. Kurfess
ATTN: Code 6750, K. Hain
ATTN: Code 7175H, D. Horan
ATTN: Code 6709, W. Ali
ATTN: Code 6700, T. Coffey
ATTN: Code 7044, E. Raymond
ATTN: Code 6780, J. Fedder
ATTN: Code 7120, R. Kinzer
ATTN: Code 2627
ATTN: Code 1434, E. Brancato
ATTN: Code 6461, F. Campbell
ATTN: Code 7550, J. Davis
ATTN: Code 6780, S. Ossakow
ATTN: Code 6701, J. Brown
ATTN: Code 7120, G. Share

Naval Surface Weapons Center
ATTN: Code F31

Navy Astronautics Group
6 cy ATTN: W. Gleason

Office of Naval Research
ATTN: Code 465, G. Joiner

Office of the Chief of Naval Operations
ATTN: OP 604C3, R. Piacesi
ATTN: OP 981

DEPARTMENT OF THE AIR FORCE

Aerospace Defense Command
Department of the Air Force
ATTN: DOFS
ATTN: DOF

Air Force Systems Command
ATTN: DLX7
ATTN: DLS

Air Force Technical Applications Center
ATTN: STINFO Office/TF

Air Force Weapons Laboratory
Air Force Systems Command
ATTN: DYC
ATTN: CA
ATTN: SUL

Assistant Chief of Staff, Intelligence
Department of the Air Force
ATTN: IN

DEPARTMENT OF THE AIR FORCE (Continued)

Air Force Geophysics Laboratory
ATTN: LKB, A. Faire
ATTN: LK, C. Stergis
ATTN: OPR, F. DelGreco
ATTN: LKB, T. Keneshea
ATTN: PHG, J. McClay
ATTN: OPR-1, J. Ulwick
ATTN: LKB, K. Champion
ATTN: LKO, R. Van Tassel
ATTN: LKB, W. Swider, Jr.
ATTN: LKD, R. Narcisi
ATTN: PHG, F. Innes
ATTN: OPR, F. Billingsly
ATTN: LKO, R. Huffman
ATTN: OP, J. Garing
ATTN: OPR, A. Stair
ATTN: OPR, R. Murphy
ATTN: OPR, H. Gardiner
ATTN: OPR, J. Kennealy
ATTN: OPR, R. O'Neill
ATTN: OPR, T. Connolly
ATTN: SULL, E. Cunha

Deputy Chief of Staff
Research, Development, & Acq.
Department of the Air Force
ATTN: AFRDQSM
ATTN: AFRDS
ATTN: AFRD
ATTN: AFSCSD

Electronic Systems Division
Department of the Air Force
ATTN: XRPH, W. Morton

Foreign Technology Division
Air Force Systems Command
ATTN: WE
ATTN: NIIS, Library

Electronic Systems Division
Department of the Air Force
ATTN: ESTT

Headquarters Space Division
Air Force Systems Command
ATTN: AWW

Headquarters Space Division
Air Force Systems Command
ATTN: SZJ

Rome Air Development Center
Air Force Systems Command
ATTN: TSLD
ATTN: OCSA, J. Simons
ATTN: OCS, V. Coyne

Strategic Air Command
Department of the Air Force
ATTN: ADW, J. Greene, Jr.
ATTN: XPFS, B. Stephan
ATTN: NRT

USAFETAC/CB
ATTN: CBTL, Stop 825

DEPARTMENT OF ENERGY CONTRACTORS

Lawrence Livermore Laboratory
 ATTN: L-517, J. Tinney
 ATTN: Technical Information Dept. Library

Los Alamos Scientific Laboratory

ATTN: D. Steinhaus
 ATTN: E. Bryant
 ATTN: E. Jones, Jr.
 ATTN: MS 563, O. Judd
 ATTN: MS 668, J. Malik
 ATTN: D. Renner
 ATTN: M. Johnson
 ATTN: M. Tierney
 • ATTN: R. Jeffries
 ATTN: S. Rockwood
 ATTN: MS 212, W. Barfield
 ATTN: W. Maier
 ATTN: D. Kerr
 ATTN: MS 560, W. Hughes
 ATTN: MS 664, J. Zinn

Sandia Laboratories

ATTN: 3141
 ATTN: C. Mehl
 ATTN: M. Kramm

Sandia Laboratories

Livermore Laboratory
 ATTN: T. Cook

OTHER GOVERNMENT AGENCIES

Department of Commerce
 National Bureau of Standards
 ATTN: A. Phelps

Department of Commerce
 National Bureau of Standards

ATTN: Security Officer for D. Lide
 ATTN: Security Officer for L. Gervantman
 ATTN: Security Officer for K. Keesler
 ATTN: Security Officer for P. Garvin
 ATTN: Security Officer for B. Stienen
 ATTN: Security Officer for Office of Director
 ATTN: Security Officer for M. Krauss
 ATTN: Security Officer for M. Scheer
 ATTN: Security Officer for G. Sinnott
 ATTN: Security Officer for J. Cooper

Department of Commerce
 National Oceanic & Atmospheric Admin.

ATTN: L. Machta
 ATTN: J. Angell

Department of Commerce
 National Oceanic & Atmospheric Admin.

ATTN: J. Townsend, Jr.
 ATTN: R. Lavoie
 ATTN: Assistant Administrator, RD
 ATTN: W. McGovern
 ATTN: G. Peterson

NASA

ATTN: N. Stone
 ATTN: W. Roberts
 ATTN: R. Hudson
 ATTN: R. Chappell
 ATTN: C. Balcher
 ATTN: W. Dran

OTHER GOVERNMENT AGENCIES (Continued)

Department of Commerce
 National Oceanic & Atmospheric Admin.

ATTN: E. Ferguson
 ATTN: R. Docker
 ATTN: R. Knecht
 ATTN: D. Williams
 ATTN: H. Sauer
 ATTN: W. Spjeldvik
 ATTN: A. Snaily

Institute for Telecommunications Sciences
 National Telecommunications & Info

ATTN: W. Utlaut

NASA

ATTN: S. Bauer
 ATTN: Code 6801, A. Tempkin
 ATTN: Technical Library
 ATTN: G. Mead
 ATTN: G. Levin
 ATTN: Code 900, J. Siry
 ATTN: Code 625, J. Heppner
 ATTN: J. Vette
 ATTN: R. Benson
 ATTN: Code 625, M. Sugiura
 ATTN: Code 620, H. Taylor
 ATTN: A. Aikin

NASA

ATTN: J. Findlay
 ATTN: G. Sharp
 ATTN: W. Taylor
 ATTN: R. Schiffer
 ATTN: P. Kurzhals
 ATTN: E. Schmerling
 ATTN: A. Schardt
 ATTN: P. Eaton
 ATTN: J. Naugle
 ATTN: D. William
 ATTN: D. Denent
 ATTN: SI-5, D. Cauffman

NASA

ATTN: O. Garriot
 ATTN: Classified Lib., Code BMe

NASA

ATTN: N-245-3, R. Whitten
 ATTN: C. Sonett
 ATTN: P. Dyal

National Scientific & Technical Info. Facility

ATTN: Acq Branch
 ATTN: SAR DLA-385

National Science Foundation

ATTN: R. Manka
 ATTN: R. Sinclair
 ATTN: E. Blake
 ATTN: W. Cramer
 ATTN: F. White
 ATTN: W. Adams
 ATTN: M. Wilson

DEPARTMENT OF DEFENSE CONTRACTORS

Aerodyne Research, Inc.
 ATTN: M. Canac

DEPARTMENT OF DEFENSE CONTRACTORS (Continued)

Aerospace Corp.

ATTN: V. Josephson
ATTN: J. Blake
ATTN: L. Aukerman
ATTN: J. Reinheimer
ATTN: H. Mayer
ATTN: F. Keller
ATTN: V. Wall
ATTN: S. Bower
ATTN: F. Morse
ATTN: J. Sorrels
ATTN: J. Stevens
ATTN: G. Paulikas
ATTN: N. Cohen
ATTN: T. Taylor

Berkeley Research Associates, Inc.

ATTN: J. Workman

COMSAT Labs.

ATTN: Document Control

ESL, Inc.

ATTN: J. Marshall

General Dynamics Corp.

ATTN: Research Library

General Electric Co.

ATTN: T. Baurer
ATTN: Technical Information Center
ATTN: M. Bortner
ATTN: J. Peden
ATTN: P. Zavitsanos
ATTN: F. Alyea

General Electric Company—TEMPO

ATTN: B. Gambill
ATTN: T. Stevens
ATTN: D. Chandler
ATTN: M. Dudash
ATTN: W. Knapp
5 cy ATTN: DASIA

Grumman Aerospace Corp.

ATTN: M. Agostino
ATTN: M. Rossi

Geophysical Institute

ATTN: N. Brown
ATTN: S. Akasofu
ATTN: R. Parthasarathy
ATTN: T. Davis
ATTN: Technical Library
ATTN: J. Wagner
ATTN: A. Belon
ATTN: H. Cole

ATTN: J. McBride

DEPARTMENT OF DEFENSE CONTRACTORS (Continued)

IIT Research Institute

ATTN: Documents Library

Institute for Defense Analyses

ATTN: Classified Library
ATTN: H. Wolfhard
ATTN: J. Bengston

Johns Hopkins University

ATTN: S. Krimigis
ATTN: P. Partridge
ATTN: Document Librarian

Kaman Sciences Corp.

ATTN: F. Shelton
ATTN: Library

Lockheed Missiles & Space Co., Inc.

ATTN: B. McCormac
ATTN: D. Fisher
ATTN: G. Davidson
ATTN: J. Reagan
ATTN: J. Cladis
ATTN: J. Schallau
ATTN: J. Evans
ATTN: L. Newkirk
ATTN: A. Anderson
ATTN: M. Walt
ATTN: R. Breuch
ATTN: R. Sharp
ATTN: R. Caren
ATTN: R. Johnson
ATTN: Technical Information Center
ATTN: R. Landshoff
ATTN: W. Frye
ATTN: W. Francis
ATTN: W. Imhof
ATTN: T. Dassell
ATTN: G. Nakano

Lockheed Missiles & Space Co., Inc.

ATTN: E. Smith
ATTN: J. Hockenberry
ATTN: D. Churchill
ATTN: S. Weiss
ATTN: Q. Riepe
ATTN: J. Cretcher
ATTN: J. Hart, Jr.
ATTN: D. Crowther
ATTN: D. McClinton
ATTN: E. Crowther

Mission Research Corp.

ATTN: D. Sappenfield
ATTN: C. Longmire
ATTN: D. Archer
ATTN: D. Sowle
ATTN: M. Scheibe
ATTN: R. Hendrick

Mitre Corp.

ATTN: R. Greeley
ATTN: P. Grant
ATTN: B. Troutman

Photometrics, Inc.

ATTN: I. Kofsky

1012 AG16)

DEPARTMENT OF DEFENSE CONTRACTORS (Continued)

University of Pittsburgh

ATTN: F. Kaufman

ATTN: M. Biondi

R & D Associates

ATTN: R. Lelevier

ATTN: R. Turco

ATTN: A. Latter

ATTN: W. Graham, Jr.

ATTN: C. MacDonald

ATTN: F. Gilmore

ATTN: H. Fry

ATTN: R. Lindgren

ATTN: W. Karzas

R & D Associates

ATTN: H. Mitchell

Rand Corp.

ATTN: C. Crain

ATTN: P. Tamarkin

ATTN: Library

Science Applications, Inc.

ATTN: D. Hamlin

ATTN: D. Sachs

Smithsonian Astrophysical Observatory

ATTN: A. Dalgarno

Smithsonian Astrophysical Observatory

ATTN: J. Henry

Space Data Corp.

ATTN: E. Allen

Stanford University

ATTN: R. Helliwell

ATTN: D. Carpenter

General Research Corp.

ATTN: J. Ise, Jr.

DEPARTMENT OF DEFENSE CONTRACTORS (Continued)

SRI International

ATTN: J. Peterson

ATTN: R. Leadabrand

ATTN: W. Chesnut

ATTN: M. Baron

ATTN: R. White

ATTN: A. Peterson

ATTN: R. Hake, Jr.

ATTN: B. Gasten

ATTN: E. Kindermann

ATTN: A. Whitson

ATTN: F. Smith

ATTN: G. Black

Teledyne Brown Engineering

ATTN: J. Cato

ATTN: R. Deliberis

ATTN: J. Dobkins

TRW Defense & Space Sys. Group

ATTN: F. Scarf

ATTN: J. Frichtenicht

ATTN: Technical Information Center

ATTN: O. Adams

ATTN: H. Holloway

ATTN: R. Watson

ATTN: R. Plebuch

Utah State University

ATTN: Security Officer

Visidyne, Inc.

ATTN: J. Carpenter

William Marsh Rice University

ATTN: R. Stebbings

ATTN: J. Chamberlain

McDonnell Douglas Corp.

ATTN: W. Olson

ATTN: A. Goedeke

DATE
ILME
-8